M2 internship: Evaluation of the trainee by the supervisor
This evaluation will be taken into account to constitute 30% of the overall grade of the internship.

Name of the student: **SENGAR Hemantika**

topic : Simulation of the Total Absorption Calorimeter response for measuring the 241Pu capture and fission reactions at the CERN n_TOF facility

Internship dates: 02/13/2023 – 08/11/2023
Laboratory/company and location: Irfu / DPhN , CEA Paris-Saclay
Name of course manager: DUPONT Emmeric

- **Appreciations** (please choose a qualifier for each item by simply putting a cross)

	*Exceptional**	*Very good*	*Good*	AVERAGE	*Insufficient,*
	*from 18**	*above 15*	*between 13 and 14, "standard" behavior*	*between 10 and 12*	*below average*
Ease of integration			X		
Motivation	X				
Autonomy/Initiative	X				
Ability to understand/skill acquisition		X			
Work Done/Efficiency		X			

*Exceptional must remain exceptional! (5% of students , the best ever supervised)

- **Free comments:**

This internship was designed as a pre-thesis internship to prepare a measurement planned for 2025. The internship went very well and we addressed aspects of the simulation requiring data (background noise for example) that we did not We haven't measured it yet. The report presents all the work carried out but it must be kept in mind that part of it was planned as part of the internship (essentially the understanding of the experimental setup and the simulation of the production of capture and fission gammas, then their transport in the experimental device), while another part normally had to be carried out later during the thesis as part of the data analysis (in particular the determination of the cuts in multiplicity and energy, and the calculation of the corresponding efficiencies).

   During the internship, Ms. Sengar demonstrated exceptional motivation and autonomy and the results presented to the entire team each month showed that she mastered her subject very well. The work carried out is very satisfactory and will be useful for the rest of the project.

Date   06/09/2023   Signature

Please return this form no later than September 11, to gulminelli@lpccaen.in2p3.fr . A very big thank you for mentoring a student .

SIMULATION OF THE TOTAL ABSORPTION CALORIMETER RESPONSE FOR STUDYING THE ^{241}Pu CAPTURE AND FISSION REACTIONS AT THE CERN n_TOF FACILITY
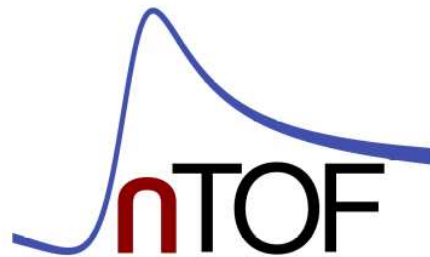
HEMANTIKA SENGAR

Erasmus Mundus Joint Master Degree on Nuclear Physics (EMJMD-NucPhys)
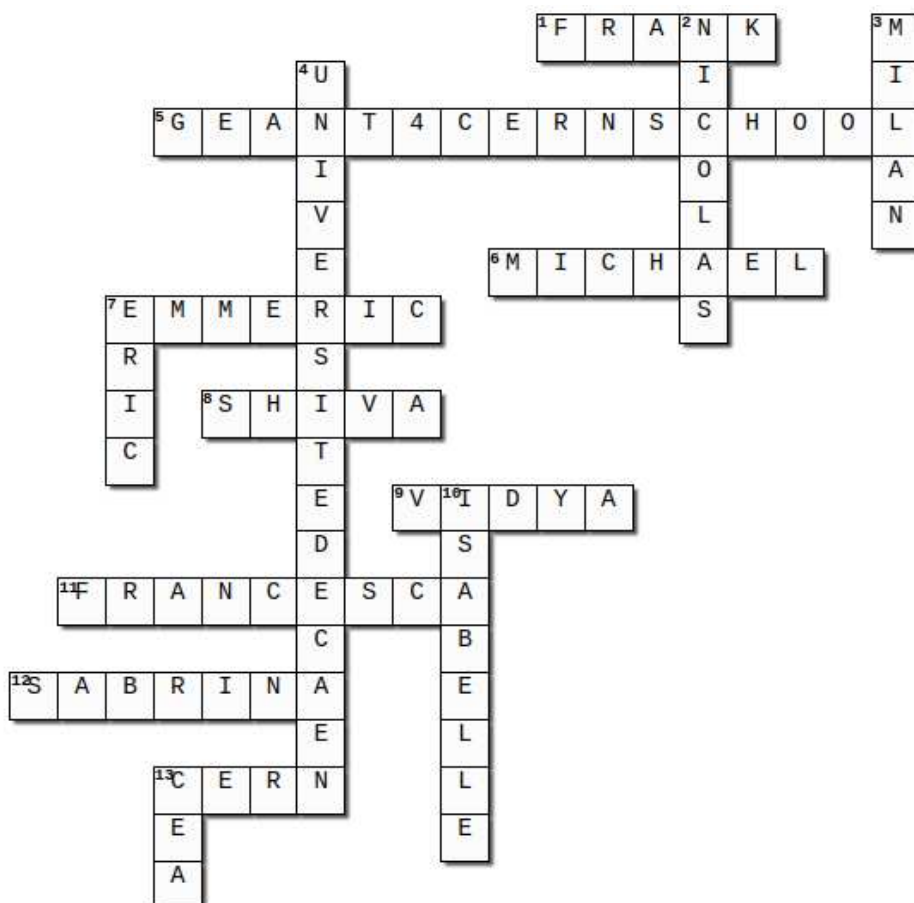Graduate School Normandie Nuclear Physics
Université de Caen Normandie

August 2023

"Cascading through the nuclear symphony, ^{241}Pu DANCEs[1] with destiny as it embraces the neutron's fleeting kiss $^{241}Pu(n,\gamma)$, birthing wondrous transformations that unveil the secrets for the next generation of nuclear reactors."

— Hemantika Sengar

ACKNOWLEDGMENTS

Down

2. Special thanks to our invaluable IT person for their exceptional technical support and assistance.

3. Grateful for the enlightening conversations at the beginning of my work and for clearing my doubts.

4. Deep gratitude to my university for providing an enriching and transformative learning experience.

7. Grateful for the help and support throughout the internship, especially for Geant4.

10. Many thanks for their assistance in day to day life at CEA and in helping find the right people always for paper-work.

13. Expressing my sincere gratitude to my hiring institute for this incredible opportunity and support throughout my journey.

Across

1. Thank you for your support and inspiring and engaging in profound and meaningful discussions.

CONTENTS

INTRODUCTION

To attain a sustainable low-carbon energy future crucial for mitigating climate change, it is required to replace fossil fuel technologies with alternative sources that emit minimal levels of CO_2, and nuclear energy can play a significant role in meeting this objective. In this context, long-term nuclear energy sustainability is dependent on the adoption of innovative nuclear systems, such as Accelerator Driven Systems and Generation-IV reactors, as well as new fuel compositions. The U-Pu cycle [2] is one of the options presented for the next generation of sustainable nuclear reactors in the Gen-IV International Forum [3]. The fissile isotope ^{241}Pu is one of the most essential isotopes in the U-Pu cycle, accounting for the neutron economy and all subsequent quantities required to run a nuclear power plant. The relevant reduced Transuranic (TRU) inventory with dominant transmutation and degradation schemes is depicted in Fig. 1.1. The isotopes are color-coded according to their role in the fuel cycle. Among the transuranic (TRU) elements in spent fuel, the approximate composition comprises 90% Pu, 5% Np, 4% Am, and 1% Cm. Consequently, the key isotopes deserving special attention are ^{239}Pu, ^{241}Pu, ^{241}Am, and ^{242}Am [4]. It is ^{238}U that is nearly exclusively responsible for TRU production, which begins with the neutron capture of ^{238}U to produce ^{239}U, which is very unstable and immediately beta-decays to ^{239}Np, which similarly soon β-decays to the more stable ^{239}Pu isotope. As shown below, neutron captures and isotope decay populate the remaining TRU vector.

$$^{238}U + n \rightarrow {}^{239}U \xrightarrow{\beta^-} {}^{239}\text{Np} \xrightarrow{\beta^-} {}^{239}\text{Pu} + n \rightarrow {}^{240}\text{Pu} + n \rightarrow {}^{241}\text{Pu} + n \rightarrow {}^{242}\text{Pu}$$
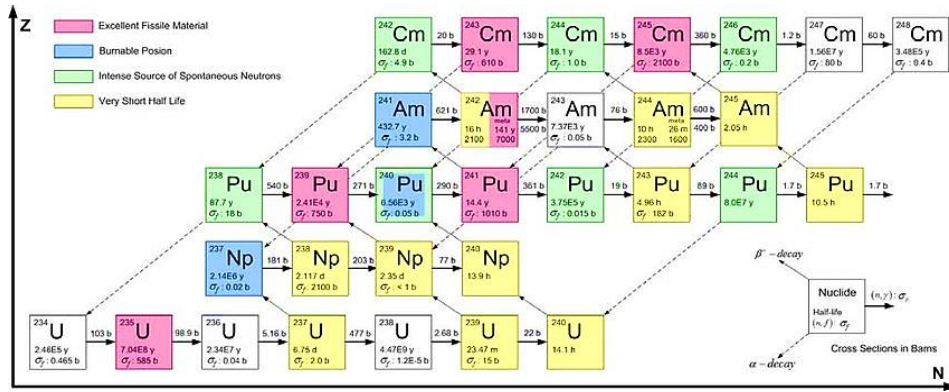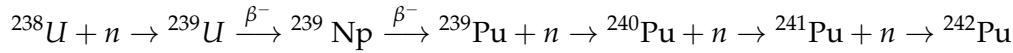

Figure 1.1: Transmutation and Decay Schemes for Important Nuclides.

The capture cross-section of ^{241}Pu is at least a factor of three lower than the fission cross-section across all energy levels, see Fig. 1.2 [5]. Measuring the capture cross section is thus challenging for this nucleus, also due to the nuclide's relative short half-life (14.4 yrs). The longer spent nuclear fuel sits in the cooling pool before being reprocessed as the spent fuel is very radioactive and hot, the more ^{241}Pu decays to ^{241}Am. Another challenge is the complicated reprocessing process itself and obtaining a high purity ^{241}Pu sample. Due to the sensitivity of plutonium and its usage in nuclear weapons, access to ^{241}Pu samples is extremely limited. This constraint can make it difficult for researchers to carry out experiments and collect enough

data for cross-section measurements. Since the 1960s, only one high-resolution data sets have been available [6].
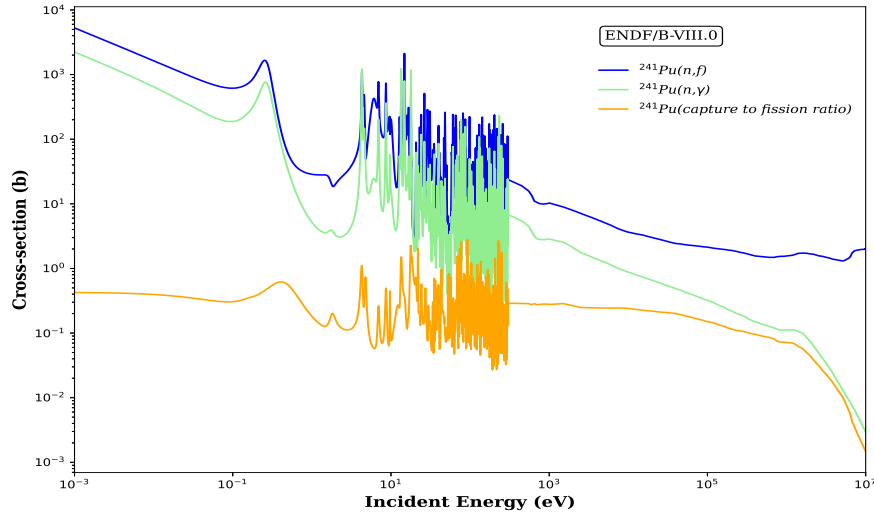

Figure 1.2: Cross-sections and capture-to-fission ratio for ^{241}Pu.

The manuscript discusses the n_TOF collaboration, which conducts measurements of neutron-induced reaction cross-sections relevant to nuclear technology. In particular, the report focuses on combining the simulations of nuclear de-excitation and gamma-ray transport of a new measurement that is set to take place at the n_TOF facility in 2025, in which a specially designed and optimized fission chamber will be used to improve the accuracy of the neutron capture cross-section of ^{241}Pu while providing additional information on the fission reaction. The first series of measurements with the n_TOF Total Absorption Calorimeter (TAC) were performed in the absence of a fission detector capable of detecting fission events within the calorimeter. As a result, discriminating between capture and fission was particularly difficult for fissile isotopes. The fission chamber that will be used in the future experiment will be custom-tailored and optimized for measurement objectives. To identify the prompt fission γ-rays, the fission veto or fission tagging approach is used, allowing for an efficient capture-fission discrimination procedure. This technique also makes it easier to investigate the properties of prompt fission γ-rays in ^{241}Pu. The manuscript also discusses the experimental setup, including the geometry of the TAC and the fission chamber. This new measurement planned in 2025 is expected to result in a major improvement in the accuracy of the capture cross-section of ^{241}Pu, as well as fresh insights into the fission reaction.

Finally, the results given in this manuscript improves the current understanding of the neutron capture and fission reaction on ^{241}Pu and the response of the Total Absorbtion Calorimeter at n_TOF to the γ-cascade generated by the neutron capture and prompt fission gamma. This work contributes significantly to the ongoing global effort to bridge the gap between the existing state of nuclear data and the accuracy required for the design and operation of novel nuclear systems. In this thesis, we tried to enhanced our understanding of the ^{241}Pu capture reaction as it has the potential to impact a wide range of nuclear technology applications.

1.1   NUCLEAR ENERGY AND NUCLEAR DATA

Fission and capture are the two most important neutron processes that occur in reactor fuel. As a result, an essential metric in reactor physics is the ratio of a given isotope's capture to fission cross-section, often known as the α-ratio, which is defined as:

$$\alpha = \frac{\sigma_\gamma(E_n)}{\sigma_f(E_n)} \tag{1.1}$$

The convolution of this parameter for all isotopes in reactor fuel is an important metric for analyzing the neutron economy of a nuclear reactor core.

In the U-Pu fuel cycle, ^{239}Pu is the fissile fuel that is created from the fertile ^{238}U. Pu isotopes are important for reactor core performance and long-term waste management due to their presence in TRU nuclides. As shown in Fig. 1.2, ^{241}Pu exhibits greater fission cross-section than capture cross-sections across the whole spectrum, which is characteristic of a fissile isotope. On the other hand, capture-to-fission ratios of fertile isotopes are greater than one are critical due to the accumulation of higher actinides that accompany them. ^{241}Pu is also a starting point for the accumulation of toxic Am and Cm isotopes.

1.2   PRESENT STATUS ON THE $^{241}Pu(n,\gamma)$ REACTION

In the instance of ^{241}Pu, this isotope functions as one of the critical fissile nucleus in the U-Pu fuel cycle. It should be noted, however, that the current knowledge of the capture cross sections on ^{241}Pu are insufficient to support the optimization of Generation IV nuclear reactors. The present data-set for ^{241}Pu is marred by inaccuracies. These sets, in addition to failing to cover the required energy range, give insufficient resolution. Apart from a handful of thermal cross section values, there exists only limited point-wise cross section data for the $^{241}Pu(n,\gamma)$ reaction and uncertainties in the measured data sets can reach as high as 10% in the thermal and epithermal regions as can be seen from Fig. 1.3, and even higher for higher energies as more reaction channels open up. It is imperative to reduce these uncertainties further to achieve the targeted goals of less than 5%, as expressed in entry 33H of the High Priority Request List (HPRL) [7] of the Nuclear Energy Agency.

Furthermore, the major evaluated libraries do not agree with each other as the outcome of the evaluation is heavily reliant on the decisions made by the evaluators. However, in order to effectively constrain the parameters of the physics models used in the evaluation, more precise measurements are required.
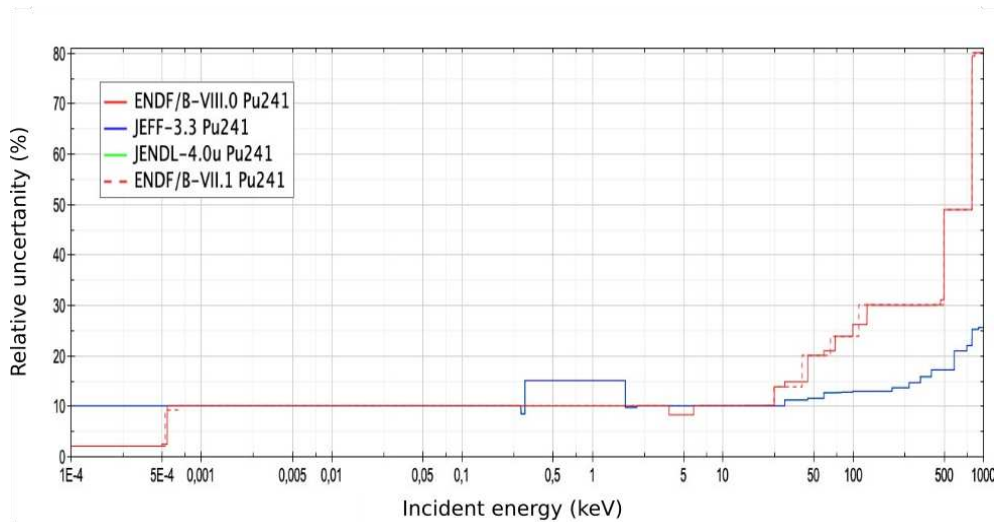

Figure 1.3: Relative uncertainty for ^{241}Pu neutron capture cross-section.

2

NEUTRON INDUCED NUCLEAR REACTIONS

This chapter provides the fundamental concepts for neutron-induced nuclear reactions, including the compound nucleus theory and radiative capture.

2.1 NEUTRON CROSS SECTION

The interaction cross-section σ is used to quantify the probability of neutron-induced nuclear reactions. When a neutron beam hits a thin layer of a given isotope, the reaction rate $R(1/s)$ is proportional to the intensity of the neutron beam $I(cm^{-2}s^{-1})$ and the number of target nuclei N

$$R = IN\sigma \tag{2.1}$$

The constant of proportionality, denoted as σ, is commonly referred to as the cross-section and is characterized by the dimension of an area. Typically expressed in units of barns (where 1 barn is equivalent to $10^{-24}\ cm^2$), this parameter quantifies the probability of a particular scattering or interaction process taking place between particles in a given target material. Neutron-induced reactions result in the generation of various partial cross sections, each contributing to the overall total cross section, denoted as σ_{tot} and represented by Eq. 2.2. This parameter denotes the likelihood of neutron interactions and scattering within a target material, and is a vital metric in various fields, including nuclear engineering, radiation protection, and astrophysics.

$$\sigma_{tot} = \sum_i \sigma_i = \sigma_{el} + \sigma_\gamma + \sigma_f + \sigma_{inel} + ... \tag{2.2}$$

Here the subscript of each partial cross section, denoted as σ_i, corresponds to a specific reaction channel. Specifically, the listed order of reactions includes elastic scattering, radiative neutron capture, neutron-induced fission, and inelastic scattering. The values of partial cross sections are dependent on the incident neutron energy and the specific reaction channel in question. Additionally, cross sections for neutron interactions vary considerably between different isotopes due to their respective nuclear structure.

Fig. 1.2 displays the (n, γ) neutron capture and (n, f) fission cross sections of ^{241}Pu across a wide range of neutron energies. As depicted in the figure, the cross section values vary significantly. The disparity between the fission and neutron capture cross-sections for ^{241}Pu displays a noticeable dependence on the energy of the incident neutrons. At thermal neutron energies (i.e., around 0.025 eV), the fission cross-section is 1023.6±10.8 barns, while the neutron capture cross-section is around 362.3±6.1 barns. Above 1 MeV, the fission cross-section is even more dominant as the capture cross-section decreases more strongly with energy [8]. The resonant structures in Fig. 1.2 demonstrate peak-to-valley ratios as large as three orders of magnitude, which is not an unusual observation in this energy range.

Four regions can be identified in Fig. 1.2:

1. For low E_n, thermal and epithermal energies, σ is proportional to the time the neutrons spend in the vicinity of the nucleus ($\sigma \propto \frac{1}{v_n} \propto \frac{1}{\sqrt{E_n}}$).
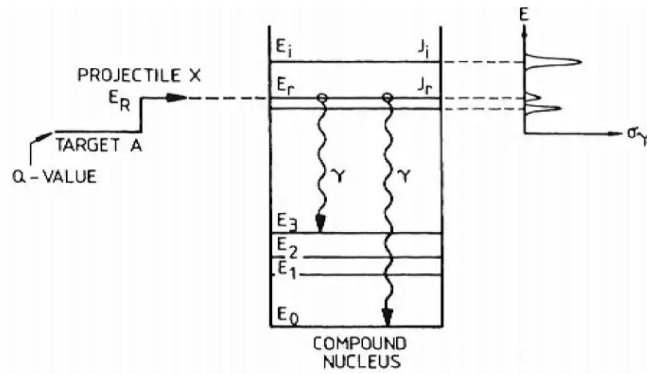
Figure 2.1: Energy levels of the compound state.

2. The cross-section displays well-defined resonances with significant peak-to-valley ratios in the resolved resonance region (RRR). This region typically spans from a few electron volts (eV) to a few kiloelectron volts (keV), depending on the isotope. The behavior of the cross-section between two resonances is strongly influenced by nearby resonances. Quasi-stationary levels of the Compound Nucleus $(n + {}^A X \rightarrow {}^{A+1} X^*)$ are related to these resonant structures. Resonances occur when the incident neutron energy matches the excitation energy of a specific compound nucleus state (taking into account the neutron binding energy). Peaks in the cross-section, as shown in Fig. 2.1, indicate resonances, while valleys show suppressed capture probability. The peak-to-valley ratios provide valuable information about underlying nuclear structure and dynamics, including level spacing, neutron-nucleus interactions strength, and the presence of collective or single-particle excitations within the compound nucleus [9, 10].

3. The various resonances begin to overlap in the unresolved resonance region (URR), at which point their inherent widths are comparable to the separation between nearby resonances.

4. Resonant structures are no longer visible at higher neutron energy because the gap between two compound states is relatively narrow at high excitation energy, and the widths of resonances are larger than the distances between resonances. As a result, there are no resonances at high energies, and the cross-section in this energy band is continuous and smooth. Additionally, as threshold reactions occur, more and more reaction channels open up [9].

The ENDF/B-VIII.0 evaluated data library corresponds to the point wise cross sections shown in Fig. 1.2. At low energies, the cross sections are often parameterized in the proper theoretical formalisms rather than presented in a point-wise basis. This has the benefit of storing fewer parameters per resonance rather than thousands of points, among other benefits. When resonances are well resolved, the resonant structures are typically represented using the R matrix formalism, in which each resonance's shape is determined by its energy, spin, parity, and a number of partial widths that are connected to each opened reaction channel. This method condenses many data points into a small number of parameters per resonance. The $1/v$ region can be represented using "negative energy" resonances, which correspond to compound nucleus levels below the neutron separation energy, and the R-matrix formalism can be extended to the URR. The elastic channel is covered in detail by the Optical Potential model, whereas the non-elastic channels are treated globally. The nuclear statistical model concept is relevant at higher energy. The optical potential for these models solely produces the transmission coefficients.

2.2 THE COMPOUND NUCLEUS: NEUTRON RESONANCES

Understanding the resonant structures seen in neutron-induced reaction cross sections is made possible by the Compound Nucleus theory [11]. The fundamental notion is that neutron-induced reactions occur in two stages:

1. The compound nucleus is initially produced with a high excitation energy $E^* = S_n + \frac{A}{A+1}E_n$ with the neutron separation energy S_n. At some specific neutron energies, the excitation energy gives rise to a complex configuration of the nucleons corresponding to a quasi-stationary level or resonance defined by its half-life τ, spin and parity.

2. In a subsequent phase, the excitation energy is released through a reaction channel, such as nuclear fission (n, f), emission of γ-radiation (n, γ), or a neutron with an energy equal to or lower than that of the incident neutron (n, n').

Fig. 2.1 provides a schematic representation of the resonances to nuclear levels of the compound nucleus. A Breit-Wigner form [12], which is determined by the resonance energy E_0 and a series of partial widths Γ_i, each related to the decay probability of the compound nucleus into the various exit channels $(\Gamma_n, \Gamma_\gamma, ..)$, provides a decent approximate description of the shape of the resonances. The Heisenberg uncertainty principle $\tau = \frac{\hbar}{\Gamma_{\text{tot}}}$ [13] relates the total sum of widths to the duration of the quasi-stationary level of the compound nucleus state. Since the observed values of Γ_{tot} in the actinide region are of the order of meVs, the expected half-life of 10^{-15} s is far longer than the normal amount of time required for a neutron to cross a nucleus without interaction. Thus, the probability of decay is independent of the formation of the compound nucleus. This is known as the Bohr's hypothesis. The R-matrix theory provides the physical underpinnings for this idea [14–16].

2.3 RADIATIVE CAPTURE

In the case of the radiative neutron capture reaction (n, γ) the compound nucleus produces γ-rays to de-excite and return to the ground or a meta stable (isomeric) state. To assess the effectiveness of the detection system when analyzing experimental data, a realistic simulation of those electromagnetic (EM) cascades is required. The precise nuclear level scheme of the compound nucleus up to the excitation energy is required for this, as well as all branching ratios and details regarding the conversion electrons for each potential decay path. Practically speaking, this is not viable because of experimental restrictions. Therefore, a statistical model from experimentally known levels up to the excitation energy of the resonance is required to complete the nuclear level scheme.

Most statistical models for the creation of EM cascades such as the one used in DICEBOX [17] convert the radiation width $\Gamma_{a\gamma b}$ into the likelihood of a γ-ray decay from level a with energy E_a to another level b with excitation energy E_b. According to Fermi's golden rule, the expectation value of $\Gamma_{a\gamma b}$ for a given radiation type X (E or M) and multipolarity L is as follows:

$$\Gamma_{a\gamma_b} = f^{(XL)} \frac{E_\gamma E_\gamma^{2L+1}}{\rho(E_a, J_a^{\pi_a})} \tag{2.3}$$

Where $f^{(XL)}(E_\gamma)$ is the so-called Photon Strength Function (PSF), which is considered to be dependent on the γ-ray energy alone (Brink's Hypothesis) and not the characteristic of the initial or final state [18, 19] and $\rho(E_a, J_a^{\pi_a})$ is the nuclear level density for states with J^π.

3

EXPERIMENTAL SETUP

This section focuses on the assessment of the response of the Total Absorption Calorimeter at the n_TOF facility and the fission chamber towards the calibration sources, namely ^{137}Cs and ^{88}Y. For the experimental set-up existing at the n_TOF facility situated at CERN, these simulations were carried out using Geant4 software. The objective of this chapter is to present a comprehensive overview of the detection systems, which served as the foundation for the simulation. Furthermore, it is anticipated that this setup will be employed in future to conduct the actual experiment utilizing ^{241}Pu samples.

3.1 THE n_TOF FACILITY AT CERN

The n_TOF facility was developed at CERN in the early 2000's. It was first proposed by Rubbia et al. in 1998 [20]. The capacity to quantify energy-dependent neutron cross-sections spanning from thermal to GeV energies makes this facility an invaluable resource for the nuclear science community. The primary objective of these measurements is to fulfill the data requirements for a range of fields, including nuclear astrophysics, nuclear technology, medical physics, and fundamental nuclear research. In recent years, the activities at n_TOF have expanded, encompassing not only the measurement of neutron cross-sections, but also the development of detectors and electronics, as well as the use of n_TOF as a neutron imaging facility [21].
The n_TOF facility utilizes spallation reactions induced by protons in Pb target to generate neutrons. Fig. 3.1a provides a schematic representation of the facility, as well as the accelerator complex at CERN. Fig. 3.1b presents a complete computer-aided design (CAD) model of the n_TOF facility. The facility consists of several components, including the spallation target area, the neutron beam lines, which are equipped with collimators and magnets, and the two time-of-flight (TOF) experimental areas where measurements are conducted.
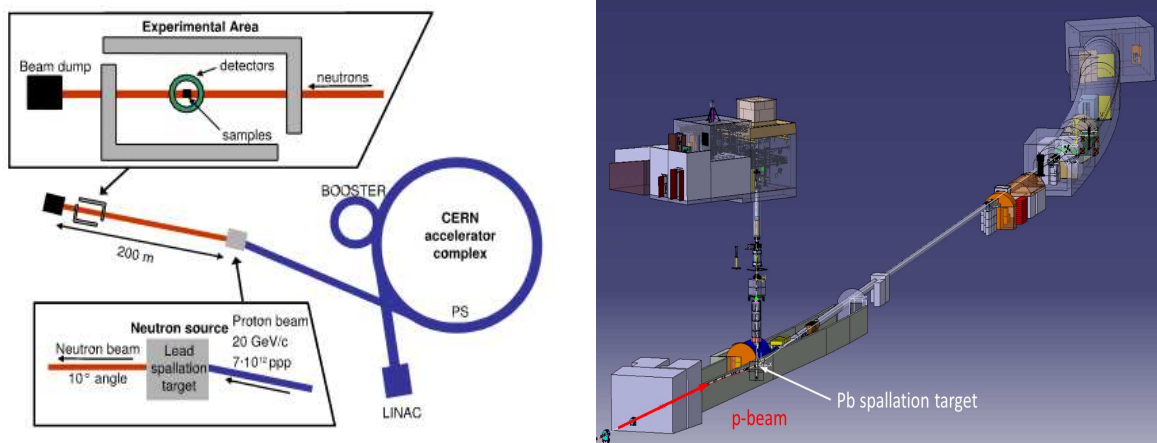
(a) Schematic overview of n_TOF facility at CERN, displaying experimental area 1 (EAR1).

(b) CAD model of complete n_TOF facility, showing experimental areas, spallation target, sweeping magnets, and collimators.

Figure 3.1: Layout of the n TOF facility within the CERN accelerator complex (source: [22]).

Through the spallation of lead caused by proton beams from the Proton Synchrotron at CERN, the n_TOF facility generates 300 neutrons on average for every 20 GeV/c proton. Depending

on the beam type, the proton beam intensity ranges from 4×10^{12} to 7×10^{12} protons per pulse of 7ns (RMS) time width. Although the average repetition rate is lower, the accelerator complex can deliver proton beams to n_TOF at a maximum rate of 0.8 Hz. In comparison to other facilities with comparable flight path lengths, the high instantaneous neutron flux produced by the high-intensity pulsed proton beam makes it possible to measure highly radioactive or low-mass materials with a better signal-to-background ratio.

Two complementary experimental areas, EAR1 and EAR2, are part of n_TOF. With a flight path length of about 180 m, EAR1 gives outstanding energy resolution, while EAR2, with a flight path length of 20 m, offers an approximately 40 times greater instantaneous neutron flux, enabling studies of highly radioactive and low-mass samples. For EAR1, the neutron beam is intercepted by a layer of borated water($H_2O + 1.28\%H_3BO_3$ in mass fraction), which suppresses and shifts the 2.2 MeV γ-rays from neutron capture in hydrogen to 0.48 MeV γ-rays from $^{10}B(n, \alpha)$, while also lowering the thermal and epithermal neutron flux at the same time. Strong magnets and enormous shielding and collimators constructed of iron, concrete, and borated polyethylene shape the neutron beam as it travels along beam lines towards the experimental locations.

3.2   THE n_TOF TOTAL ABSORPTION CALORIMETER

At the CERN n_TOF facility, the Total Absorption Calorimeter (TAC) is a segmented 4π detector array made of 40 individual BaF$_2$ crystals, 12 pentagonal and 28 hexagonal in shape, for measuring neutron capture cross sections [23]. It is based on the design from the former Karlsruhe TAC [24] to meet the requirements of an ideal Total Absorption detector: large solid angle coverage, high efficiency, high spatial segmentation, low neutron sensitivity and fast time response. The configuration of the spherical detector shell employed in the investigation, with each crystal being surrounded by protective layers, as shown in Fig. 3.2. Each crystal is encapsulated by 0.2mm thick layers of Teflon and polished aluminium foil and a 1mm thick borated carbon fibre sleeve to reduce neutron sensitivity. The crystals are coupled to 5" Photonis XP4508B photomultipliers and mounted in an aluminium honeycomb structure housing the full spherical detector shell. The TAC has hemispheres that can be moved in order to reach the samples positioned inside the center by opening the detector.The entire detector system is supported and stabilized by the aluminum cylinder and the hemispheres being firmly fastened to an aluminum enclosure that is further integrated into a honeycomb structure.
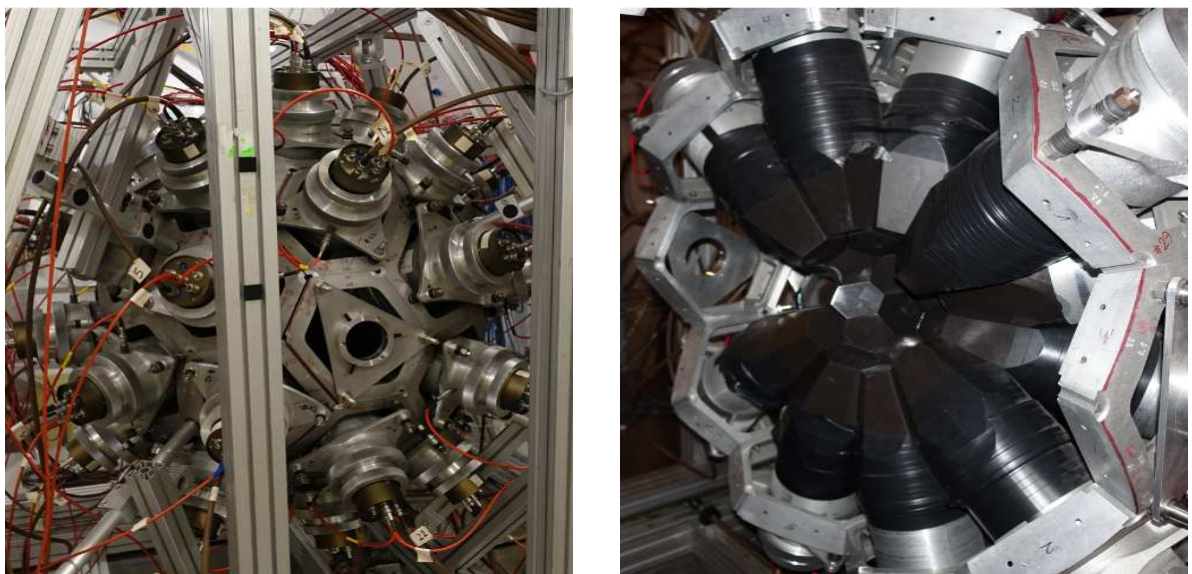
Figure 3.2: Images of the TAC in its closed (left) and open (right) configurations.

The TAC is designede to simultaneously detect γ-rays from an EM cascade that occurs after a neutron capture event. The efficiency of detecting at least one γ-ray from a cascade is close to 100 %. This high detection efficiency will be brought down later with the final cuts applied in the experimental data analysis in order to improve the signal-to-background ratio and will be calculated with simulations.

3.2.1 *Neutron sensitivity and absorber*

The term "neutron scattering" refers to the phenomenon in which neutrons from the beam are scattered upon interacting with any material they encounter. Consequently, the neutron sensitivity of the detector refers to the probability of detecting these scattered neutrons. In other words, it quantifies the likelihood of detecting and registering the presence of scattered neutrons resulting from the interaction of the beam with various materials.
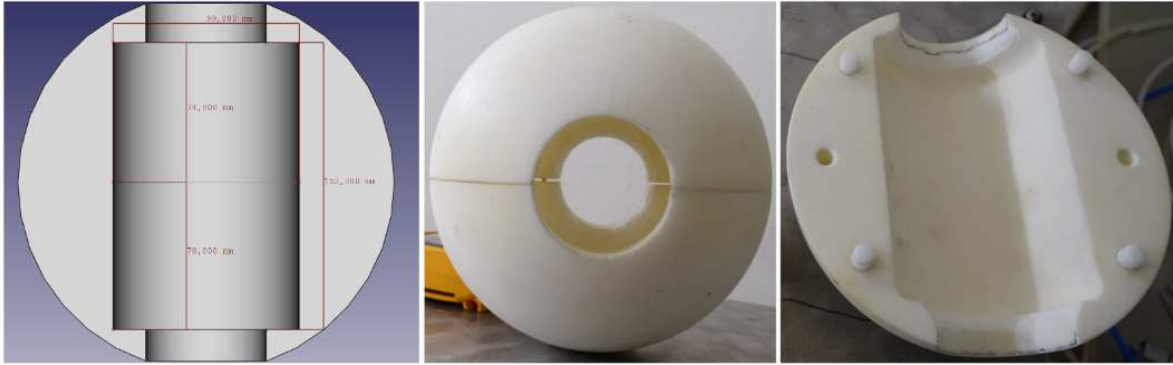
Figure 3.3: Images (center and right) and a CAD drawing (left) of the neutron absorber used in the measurement.

A combination of neutron moderator and absorber material surrounds the sample in order to reduce the neutron sensitivity and consequently its associated background contribution for the TAC setup. The experimental setup used a so-called neutron absorber consisting of moderating material loaded with neutron absorbers. With a total density of 1.06 g/cm3, the absorber is built of polyethylene that has been loaded with 7.56 w% natural lithium. It exhibits good performance for moderating and absorbing neutrons and has the benefit of having a very low γ-ray attenuation thanks to its low effective atomic number Z. To make room for the neutron beam and the fission chamber containing the samples, the interior of the absorber is vacant. The 20 cm-diameter spherical absorber used in the Geant4 simulation is depicted in CAD drawing in Fig. 3.3. With respect to the sphere's center, the inner cylinder's middle is 2 mm off in the geometry.

3.3 FISSION CHAMBER

The development of a fast fission chamber (FICH) is crucial for accurately identifying and removing the prompt γ-ray cascades originating from the fission reaction of ^{241}Pu within the total measured spectra. Although the first part of the simulation accounts for γ-rays solely from the neutron capture process, it remains essential to discuss the geometry of the fission chamber which is important for the simulation of the transport of γ-rays . This is because the fission chamber will house all the Pu samples, making it a significant component of the overall experimental setup geometry for the simulation. By describing the characteristics and configuration of the fission chamber, a comprehensive understanding of the experimental setup can be achieved, enabling precise simulation and analysis of the detected gamma-ray cascades. The main design criteria for the chamber are:

1. Compact size

2. Maximize the amount of ^{241}Pu samples.

3. Good timing performance.

4. Minimum amount of dead material in and around the neutron beam.

The first constraint is from the limited space within the n_TOF Total Absorption Calorimeter, which is a 20-cm-diameter sphere. The inclusion of the neutron absorber material further reduces the available space. As a result, the goal is to design a compact chamber that maximizes space use. This requirement for compactness, however, must be balanced with the second criterion, which emphasizes the importance of acquiring a sufficient amount of statistical data within a suitable time-frame. As a result, it is critical to strike a delicate balance between maximizing space efficiency and ensuring sufficient statistical data can be obtained within a reasonable beam time when building the chamber. The detector's timing performance is critical for establishing precise time resolution and influences the capacity to discriminate between fission fragments and alpha, and to limit particle pile-up events. The detector's intrinsic timing performance is dependent on the drift velocity of electrons created by ionizing fission fragments. Several factors influence this performance, including the gas used, the pressure maintained within the detector, and the strength of the applied electric field. The interplay of these factors determines the timing characteristics of the detector, shaping its ability to precisely measure and record the timing information associated with detected events.

The final requirement stems from the necessity to address background issues. In general, reducing the amount of dead material in the neutron beam should result in lower background levels in the TAC. Previous investigations with ^{235}U samples using MicroMegas (MGAS) detector [25], indicated that the copper mesh and anode of the MGAS amplification stage contributed significantly to the background signal above several hundred electron volts (eV). As a result, a basic ionization cell design without an amplification stage, which is not required for detecting fission fragments, is a realistic method. Implementing such a design effectively mitigates the effects of background signals emanating from the amplification stage, allowing for enhanced background suppression within the TAC for the actual experiment.

3.4   GEOMETRY MODEL: EXPERIMENTAL SETUP FOR MONTE CARLO SIMULATIONS

3.4.1   *Total Absorbtion Calorimeter (TAC) and Fission Chamber (FICH)*

For modelling the TAC, the simulation tool GEANT4 [26] with the Standard Electromagnetic Package [27] was employed. It enables the implementation of complicated geometries, has thoroughly proven physics models, and provides the powerful tracking capabilities required for event reconstruction. As illustrated in the left panel of Fig. 3.4, our model contains the BaF$_2$ crystals with their encapsulation, the photomultipliers, and the honeycomb framework that supports the detector array. In addition to this geometry the fission chamber and its electronics, Kapton windows as well as the absorber and the beam pipes are added, as can be seen in the right panel of Fig. 3.4.

In the simulation, FICH is designed as multi-plate ionization chamber containing two stacks of axial ionization cells. Fig. 3.5 depict CAD drawings of the chamber. The housing is comprised of a 1.5 mm thick aluminum tube with a 66 mm outer diameter and a 78 mm length. The maximum outside diameter of 90 mm and total length of 123 mm, including all flanges, fit perfectly in the TAC while still providing enough space for the absorber and connecting pipes. Two stacks of seven ionization cells are introduced from each end of the chamber, immediately placed on their respective motherboards. The stacks have a minimum inner diameter of 50
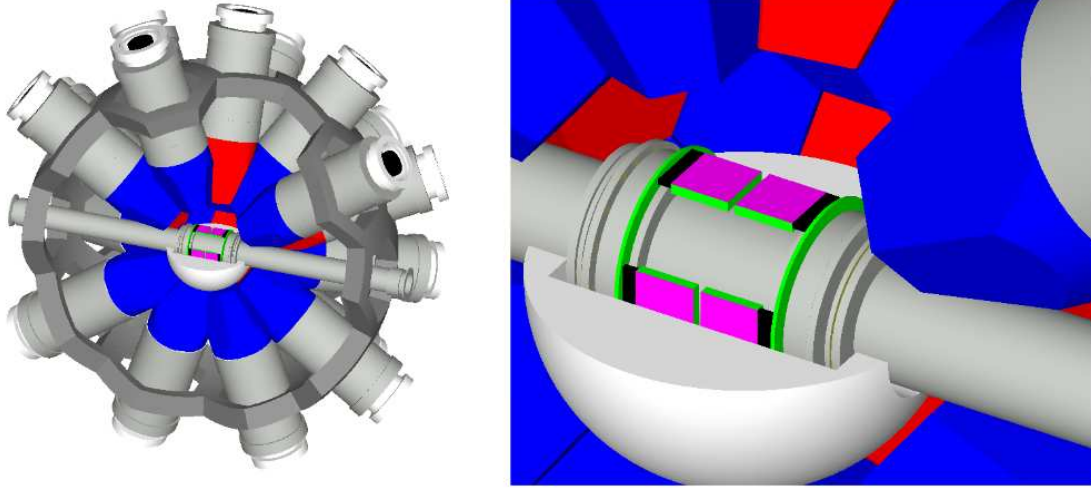
Figure 3.4: Geant4 model of the experimental setup (on the left). For visual considerations, just one hemisphere is displayed. Red and blue are used to tint the hexagonal and pentagonal crystals. The zoom (right) shows the housing, PCB pieces (green), PA-shaper electronics (pink) and connectors (black) of the fission chamber implanted in one half of the neutron absorber and connected to the beam pipes.

mm, which will allow for a beam with an FWHM of about 16 mm and a total width of less than 40 mm. In total, 8 anodes are gathering signals from the cathode-deposited targets. To provide a Faraday cage, the chamber is closed with aluminized 25 μm Kapton windows. Fig. 3.6 depicts the configuration of the cathodes, anodes, and deposits. The ionization cells are separated by 20 μm aluminium, with either one 20 μm anode or two 10 μm cathodes, for a total of 300 μm aluminium in the beam. For the highly precise requirements of this future measurement, the choice of gas is critical. It must have a high drift velocity and strong alpha-fission fragment separation. In general, high purity tetrafluoromethane CF_4 is a very rapid gas, although it is electro-negative. This results in electron attachment, which exacerbates the energy resolution. Nonetheless, the advantages it provides over other gases due to its higher drift velocity outweigh the disadvantages and make it a desirable choice for this measurement and hence to be included in the geometry. At the applied electric field of 1400 V/cm the drift velocity is roughly 11 cm/μs at a gas pressure of 1100 mbar.
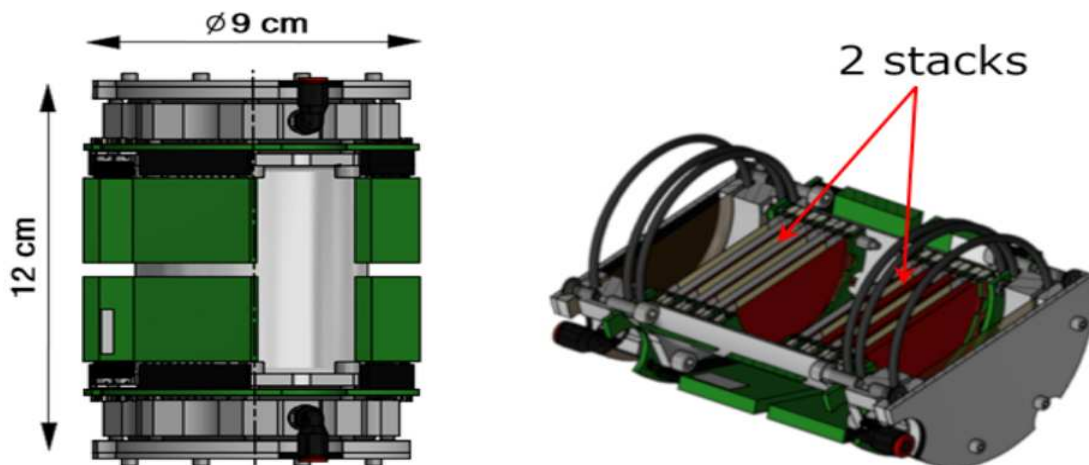
Figure 3.5: A sectional image of the fission chamber in 3D CAD. The preamplifiers are represented by the green blocks that surround the chamber.
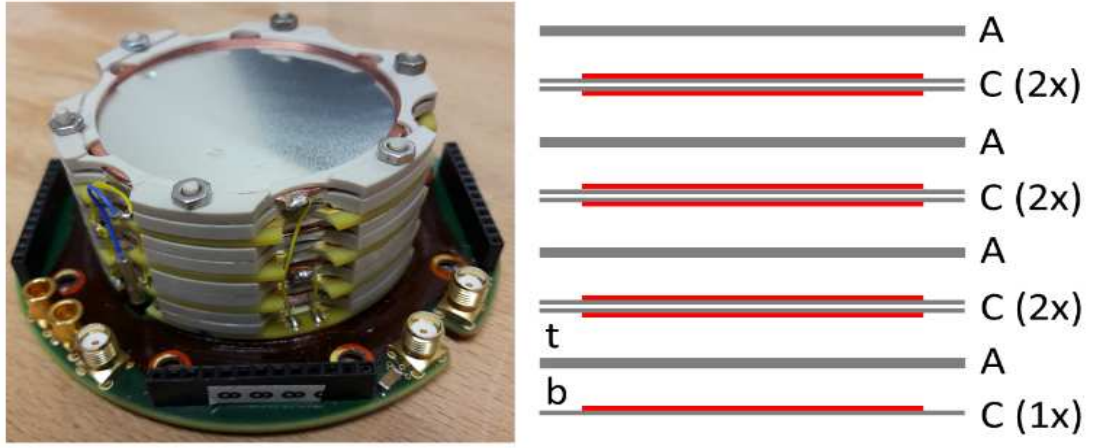
Figure 3.6: (Left) Photo of one stack of ionization cells mounted on the motherboard.(Right) Arrangement of the cathodes (C) and anodes (A) of one stack, deposits for the future experiment are indicated in red. There is one anode that reads only from 1 deposit while the others read signals from two deposits. In the case of two deposits the two ionization cells per anode are labeled top (t) and bottom (b).

3.4.2   *Event reconstruction*

The results of the Geant4 simulation are processed on an event by event basis, similar to the experimental data:

1. All hits in the BaF_2 detectors are read from the simulation output.

2. The deposited energy in each crystal is sampled based on its energy resolution. We might further need to apply additional broadening after comparison with the actual experimental data.

3. The duration between two consecutive events is sampled using a preset reaction rate, and the time between individual detector hits is determined via a Monte Carlo simulation.

4. Application of dead time and pile-up in the simulation.

5. The simulation produces a list of events characterized by their total deposited energy in the TAC and detected crystal multiplicity.

3.4.3   *Energy Resolution of TAC*

For reliable Monte Carlo simulations of the TAC response to γ-rays, the energy resolution of the BaF_2 crystals as a function of the deposited energy E_γ must be characterized.
The resolution $R(E_\gamma)$ has been calculated by fitting Eq. 3.1 [28]

$$R\left(E_\gamma\right) = \frac{\Delta\left(E_\gamma\right)}{E_\gamma} = \frac{FWHM}{E_\gamma} = \alpha + \beta / \sqrt{E_\gamma} \tag{3.1}$$

to the experimental energy resolution, namely the full width at half maximum (FWHM) of the fits to the experimental response of the calibration sources mentioned in Table. 3.1 taken from [29].
For the post-processing of Geant4 simulation results, the parameters α and β, obtained through fitting based on Equation 3.1, were employed to determine the energy resolution for any

deposited energy within a crystal. The calculated values for these parameters were as follows: $\alpha = 0.008 \pm 0.004$ and $\beta = 0.131 \pm 0.005\sqrt{MeV}$.

The average energy resolution of the TAC at various $E\gamma$ is summarized in Table. 3.1 and the energy resolution for all E_γ and the fit according to equation Eq. 3.1 in red is shown in Fig. 3.7.

Table 3.1: Average energy resolution of the TAC at various E_γ [29].

source	$E_\gamma (MeV)$	TAC $R(E_\gamma)$ %
^{137}Cs	0.662	16.9
^{88}Y	0.898	14.3
^{88}Y	1.836	10.5
$AmBe$	4.438	7.4
CmC	6.130	5.6
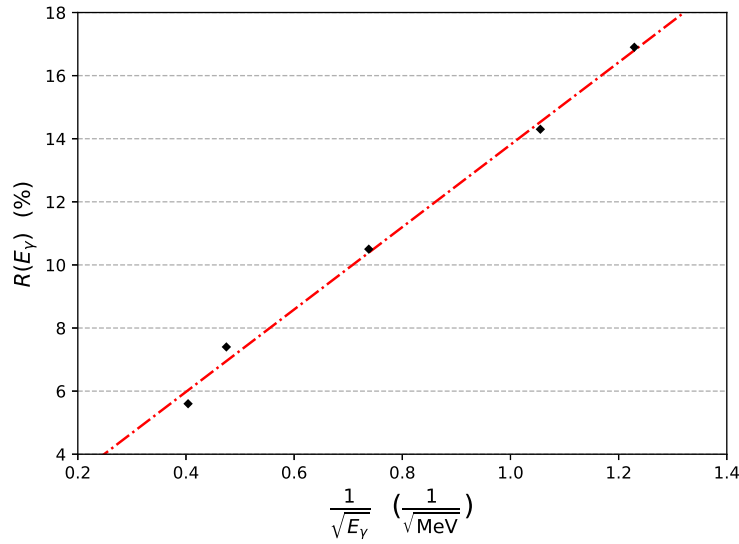
Figure 3.7: Energy resolution for BaF_2, smaller E_γ are on the right end of the x-axis.

3.4.4 *Validation of the simulation process*

The geometry model is validated by visualizing the sum energy spectra of standard calibration sources such as ^{137}Cs and ^{88}Y for various multiplicity criteria. The results from the Monte Carlo simulation are shown in Fig 3.8 and 3.9. It can be confirmed from Fig 3.8 that for the ^{137}Cs source the sum peak is at 0.662 MeV for crystal multiplicity (m_{cr}) 1 and 2 as expected. It can also be noted that there are no events for m_{cr} = 3 in this case because of the extremely low probability of occurrence. When $m_{cr} = 2$, events occur when the incident energy (E_{inc}) of the γ photon is partially absorbed by the first crystal, resulting in an energy of E_{h1}. The remaining energy $(E_{h2} = E_{inc} - E_{h1})$ is compton scattered and subsequently detected by an adjacent crystal. Therefore, the total energy observed in this scenario is given by $E_{sum} = E_{h1} + E_{h2} = E_{h1} + E_{inc} - E_{h1} = E_{inc}$.

The two essential parameters for the simulation and further analysis are the energy detection threshold (E_{thresh}) and the inner radius of the TAC (R_{TAC}) summarized in Table 3.2.

The experimental BaF_2 detection threshold E_{thresh} defines the low energy γ-threshold and is chosen keeping in mind that the applied threshold is not too low causing noise in the data or
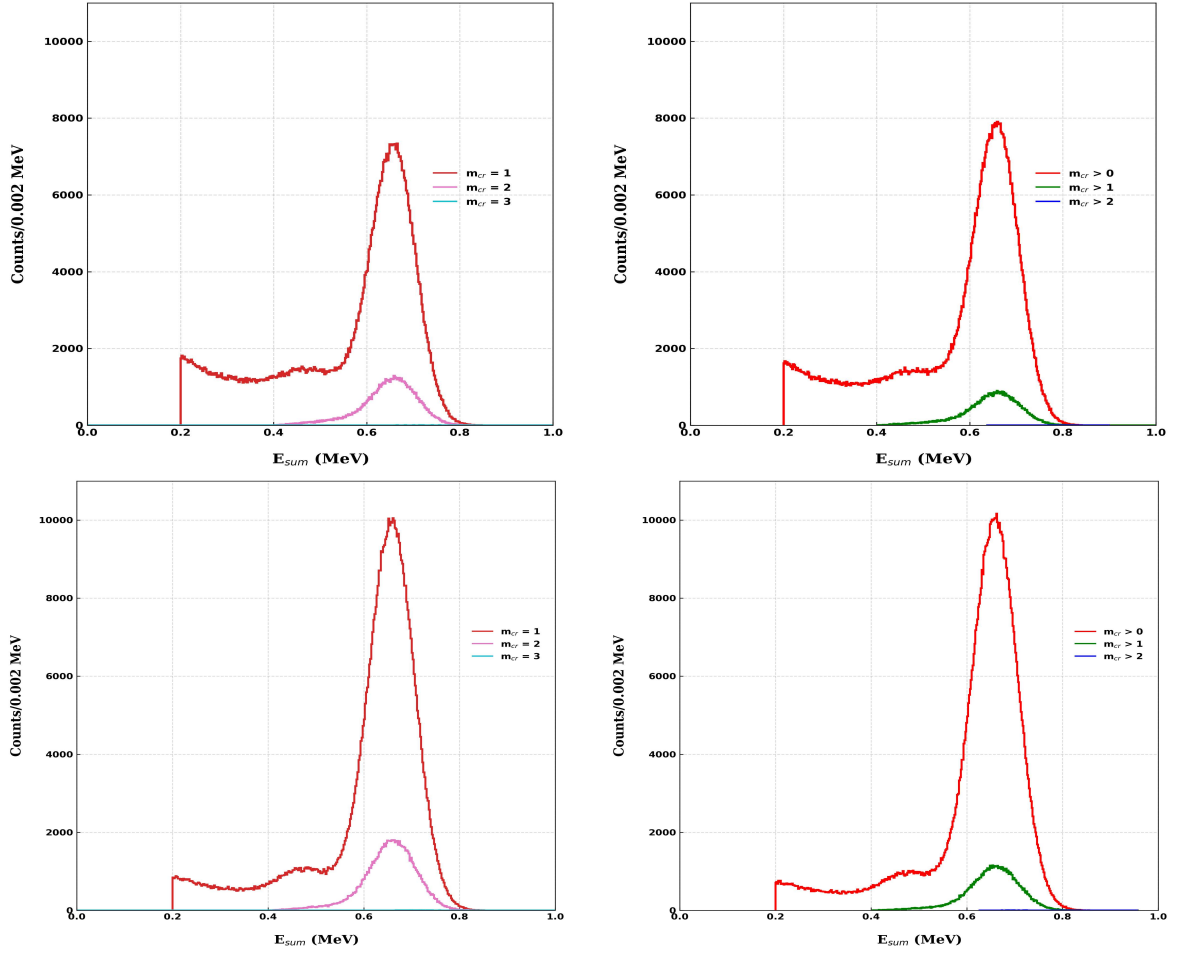
Figure 3.8: Simulated results for ^{137}Cs calibration source with(top) and without(bottom) absorber.

Table 3.2: Summary of the low energy detection threshold for the individual BaF_2 crystals and the inner geometrical radius of the TAC.

$E_{thresh}(keV)$	$R_{TAC}(cm)$
200	10.66

too high causing real count loss in the post processing of the simulated data. Other than E_{thresh}, R_{TAC} also strongly influences the sum energy spectra. The initial value of this parameter was primarily driven by considerations related to the setup's geometry. The adjustment was done by trial and error and judged by eye (not fitting). There might be a need to vary this parameter within a few mm until the experimental data for the future experiment is reproduced by the Monte Carlo results.

In the present investigation, our attention was directed towards the evaluation of simulated results pertaining to the ^{88}Y source. Firstly, as expected we see a sum peak at 2734.124 keV resulting from 898.04 keV and 1836.084 keV gamma from the ^{88}Y source. The simulated results for ^{88}Y shown in Fig. 3.9 also reveal the presence of additional peaks, especially for m_{cr} = 2 approximately around 1198 and 2136 keV. These peaks are more pronounced in simulations that incorporate the neutron absorber, but interestingly, they also appear in simulations where the absorber has been excluded.

To understand their origin we concentrated on the energy range spanning from 1 to 1.4 MeV for m_{cr} = 2. Notable counts for energy between ∼300-350 keV was observed as shown in Fig. 3.10.
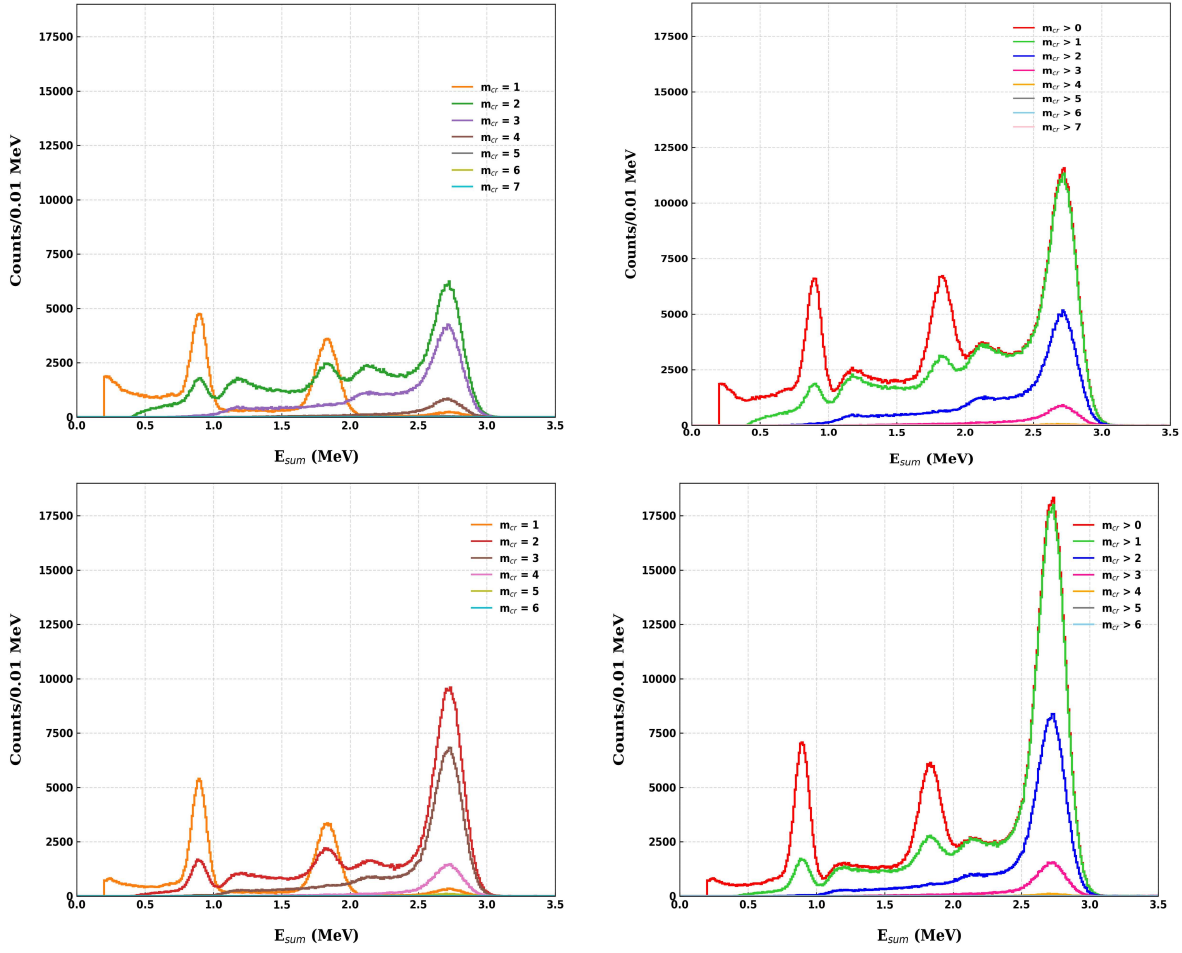
Figure 3.9: Simulated results for ^{88}Y calibration source with(top) and without(bottom) absorber.

The presence of this peak around ∼300 keV is evident even in the unprocessed raw output, prior to applying any threshold or detector resolution corrections, as depicted in Fig. 3.10 (left).
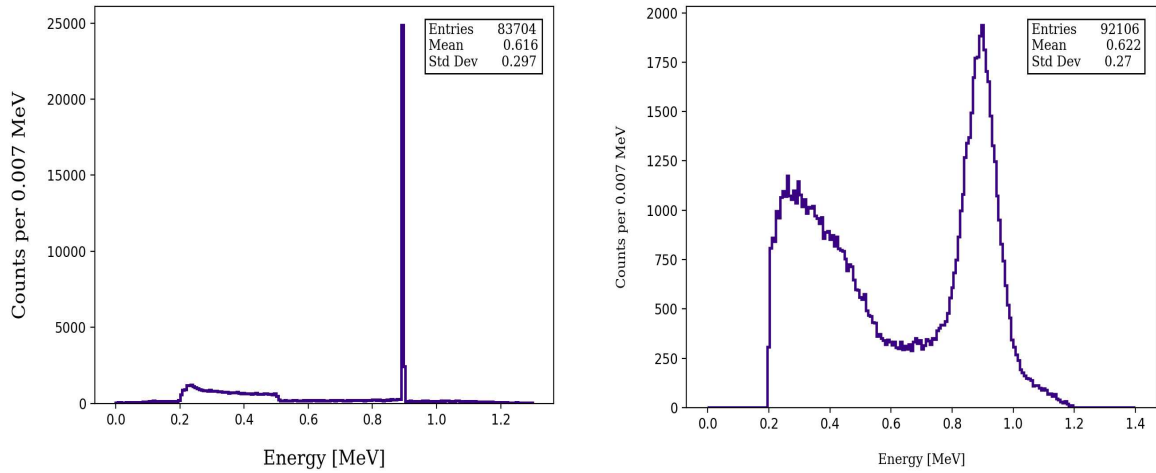
Figure 3.10: Simulated results for ^{88}Y calibration source without applying resolution(left) and after the application of TAC resolution(right) and E_{thresh}.

Evidently, this specific peak, when considered in the context of the summation spectrum, causes an apparent influence upon the cumulative peaks occurring at approximately 1198 and 2136 keV, as seen in the simulated outcomes for ^{88}Y in Fig. 3.9. Appendix-II B contains information on additional efforts undertaken to determine the cause.

4

DICEBOX SIMULATION AND RESULTS

The Monte Carlo code DICEBOX was used for the generation of EM cascades emitted in the ^{241}Pu(n, γ) reaction. The code is designed to simulate γ decay of an excited nucleus from a high-level density region where individual levels are unknown but still resolved [17]. Its main characteristic is its capacity to properly treat expected fluctuations in transition intensities and the actual number of levels.

4.1 THE $^{241}Pu(n, \gamma)$ CASCADE GENERATOR

The Monte Carlo DICEBOX code was used to generate decay of well-separated levels with specified spin and parity at neutron separation energy of ^{242}Pu. Neglecting the energy added to the compound nucleus by the incident neutron in the capture process, the excitation energy of the compound nucleus equals the neutron separation energy $S_n(^{242}Pu) = 6.31$ MeV.
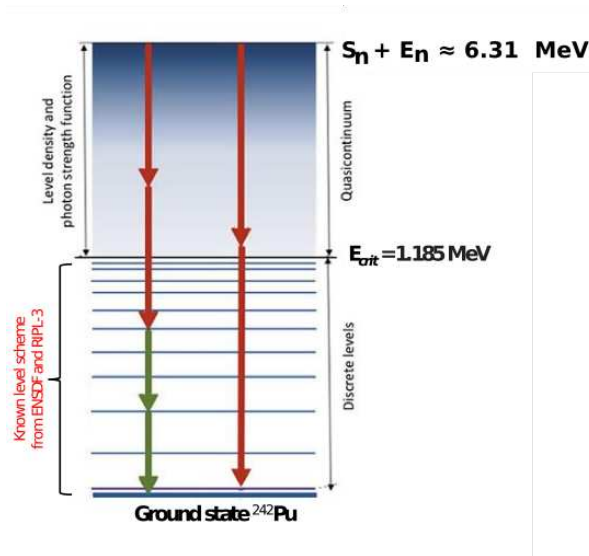
Figure 4.1: Schematics of $^{241}Pu(n, \gamma)$ cascade generator.

The (n, γ) cascades as illustrated in Fig. 4.1, can generally decay to the ground state via many intermediate levels from this excitation energy. In the case of the decay of neutron capturing levels in ^{242}Pu, the overall number of intermediate levels are of the order 10^6 to 10^7, depending on the level density model. DICEBOX calculates the individual decays from all of those levels and transitions using the following approach:

1. Below a certain critical energy E_{crit} a full set of experimentally determined nuclear levels a is known, including level energies E, spins J, parities π and all branching intensities of depopulating transitions between levels. These data are compiled in the Evaluated Nuclear Structure Data File (ENSDF) [30].

2. A complete, presumably unknown set of level energies E_a of a nucleus above E_{crit} represents a random discretization of an a priori known level density formula $\rho(E, J^\pi)$.

3. When mixing of various multipolarities is permitted by selection rules, the partial radiation width $\Gamma_{a\gamma b}$ for a transition $a \longrightarrow b$, starting at a level a with $E_a > E_{crit}$, is assumed to be a random quantity whose value is given by:

$$\Gamma_{a\gamma b} = (1 + \alpha_{IC}) \sum_{X,L} y_{XL}^2 (E_a - E_b)^{2L+1} \frac{S_\gamma^{(XL)}(E_a - E_b)}{\rho(E_a, J_a^{\pi_a})} \qquad (4.1)$$

Here, $S_\gamma^{(XL)}$ denotes the photon strength function (PSF) for transition type X (electric or magnetic transitions) and multipolarity L, and $\rho(E_a, J_a^{\pi_a})$ is the nuclear level density (NLD) for levels with spin J and parity π_a at initial excitation energy E_a. Porter-Thomas fluctuations [31] are included by the random values y_{XL} sampled from a standard normal distribution. The coefficient α_{IC} gives the contribution of the internal electron conversion.

4. Each cascade starts from a single, well-defined initial level with a known excitation energy, spin and parity E_1, J_1 and π_1, respectively.

There is no on-the-fly correction of internal electron conversion process in this version of DICEBOX. A post-processing script was developed later on in order to remove the contribution of IC. Following this approach, levels in a simulated nucleus can be obtained from a random discretization of the adopted NLD formula. Here, we define nuclear realization (NR) as the simulated system of all levels, including level positions and their decay probabilities. Only for primary transitions will different initial states with (almost) the same excitation energy (neutron resonances) have different decay probabilities. As a result, we define nuclear supra-realization (NSR) as a set of all nuclear realizations that have identical levels below the initial state and differ only in initial state decay properties. Different neutron resonances within an NSR would then correspond to different NRs. This approach assumes no transitions between different initial states.

Following this, the set of levels obtained by discretizing the level-density formula, along with the full set of random partial radiation widths obtained by Eq.4.1 for all required pairs of levels (a, b), will be referred to as a nuclear realization and denoted as ω. In the spirit of the above-outlined approach, there exist an infinite number of nuclear realizations, forming a sample space Ω, one of which is identical with the actual set of levels and partial widths of a given nucleus. It is believed that such an NR can only be obtained with realistic NLD and PSFs models.

The procedure for generating the de-excitation from the initial level to the final state in DICEBOX is explained in section A of Appendix-I. Understanding the process is facilitated by an illustration in Fig.A.1.

The cascades are characterized by the γ-ray energies E_γ and the γ-multiplicity m_γ. The nuclear level density (NLD) and the photon strength function (PSF) are obtained from physical models. The parameters of those models are adjusted on a bulk of experimental data to best create the gamma spectra for $^{241}Pu(n,\gamma)$ [32−39]. The present work took into consideration the findings and conclusions of recent research [40] regarding the limitations imposed on the Photon Strength Functions (PSFs) in actinides. In this regard, the E1 PSF was adopted in the form of a modified general Lorentzian (MGLO) prescription [41], wherein the tail of the giant electric dipole resonance (GEDR) was considered with a modified factor (k = 1.5). Additionally, the M1 PSF was composed of double-humped scissors modes (SM) and single spin-flip (SF) modes, both described by Lorentzian resonances. As for the E2 PSF, its impact on the results was found to be negligible, thus approximated by a single Lorentzian description of the giant electric quadrupole resonance (GEQR).

The parameters pertaining to the M1 PSF, specifically the σ_r values of all three components are highlighted in Table 4.1 alongside the E1 parameters.

Importantly, the Dicebox framework employed in this study explicitly accounted for internal electron conversion by utilizing the α-coefficients obtained from the BRICC database [42].

Table 4.1: PSF parameters used for the simulation.

E1 (MGLO)	E_{G1}	σ_{G1}	Γ_{G1}	E_{G2}	σ_{G2}	Γ_{G2}			
	MeV	mb	MeV	MeV	mb	MeV			
	11.28	325	2.48	13.73	384	4.25			
M1 (SM + SF)	E_{SM1}	σ_{SM1}	Γ_{SM1}	E_{SM2}	σ_{SM2}	Γ_{SM2}	E_{SF}	σ_{SF}	Γ_{SF}
	MeV	mb	MeV	MeV	mb	MeV	MeV	mb	MeV
	2.2	0.30	0.50	2.80	0.60	1.0	6.60	1.50	4.00

The level density ρ in DICEBOX is factorized as:

$$\rho(E, J, \pi) = f(\pi)f(J)\rho(E) \tag{4.2}$$

where the three components on the right side of the equation represent dependency on parity π, spin J, and excitation energy E, respectively. It should be emphasized that any level density model is only employed at excitation energy $E > E_{crit}$; all level information for $E \leq E_{crit}$ is derived from the input file. The simulation used Constant-Temperature (CT) level-density model in the form given by von Egidy et al. [41, 43] as in eq. 4.3,

$$\rho(E, J, \pi) = f(\pi)f(J)e^{-(E-E_0)/T} \tag{4.3}$$

where the parameters T and E_0 are, respectively, the nuclear temperature and the back-shift. The factor $f(J)$ represents a probability that a level has a spin J and the form of it is given in [44]. In the parametrization of CT formula [41, 43], a semi-empirical prescription for the spin-cut-off parameter (σ) [44] is used where $\sigma = 0.98A^{0.29}$ where A is the mass number of the isotope.

The temperature $T = 0.40 MeV$ and the energy offset $E_0 = -0.22 MeV$, as well as the standard form of spin dependence with a constant spin cut-off parameter and no parity dependence [41] were used. Typically the levels and transitions for low excitation energies can be taken from data bases like ENSDF [30] but choosing a critical energy lies with the experimenter. For this measurement the critical energy was chosen to be 1.185 MeV as it was ascertained that a complete gamma transition scheme was available to feed to DICEBOX below this critical energy [45], see Fig. 4.2.

4.1.1 *Possible spin and parity configurations*

The present investigation extended its focus towards the inclusion of partial wave resonances up to l=2, originating from the process of neutron capture in the nuclide ^{241}Pu possessing an intrinsic spin and parity of I = $5/2^+$. Specifically, the simulation aimed to capture the intricate dynamics and subsequent decay of distinct levels that were adequately separated, each possessing specific spin and parity characteristics, at an excitation energy of 6.31 MeV. The simulated framework was designed to encompass the levels based on spin and parity selection rules indicated in Table 4.2.

The spin and parity characteristics of the resonances/levels that are populated in the low-energy neutron capture reaction $^{241}Pu(n, \gamma)^{242}Pu$ can be accessed through evaluated files, which are based on experimental data [46]. These files provide valuable information regarding the resonance/level energy (E_r), the target nucleus spin (I = $5/2^+$ for ^{241}Pu), the angular momentum (l=0 at low neutron energy), and the spin of the resonance/level (restricted to J = 2^+ or 3^+ for ^{241}Pu when l=0) along with their corresponding partial widths. It is important
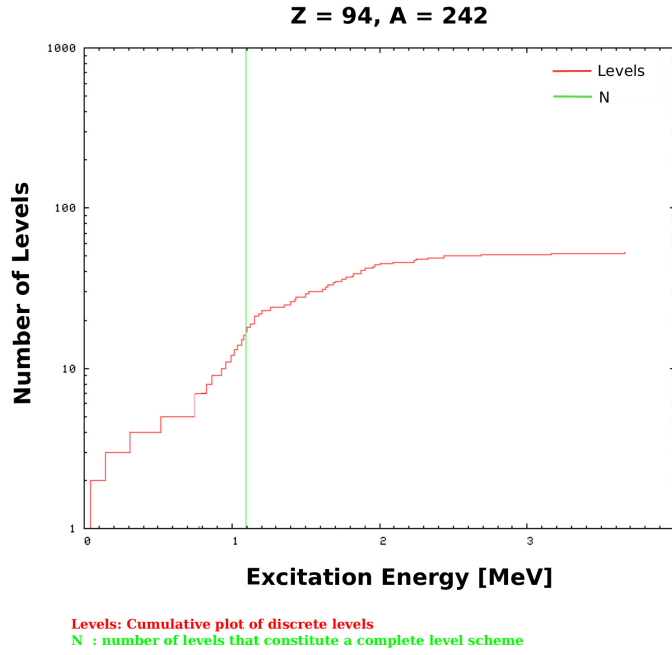
Figure 4.2: Number of levels available in RIPL/ENSDF for ^{242}Pu. The level scheme is complete up to the vertical green line.

Table 4.2: Possible level spins populated by neutron capture on ^{241}Pu used for DICEBOX simulation.

l	J^{π}
0	2^+ , 3^+
1	1^- , 2^- , 3^- , 4^-
2	1^+ , 2^+ , 3^+ , 4^+ , 5^+

to note that at higher incident neutron energies, where l>0, a wider range of level spins and parities becomes possible. Consequently, simulations were conducted for higher-lying states to gain a comprehensive understanding of the results.

However, for the actual measurements, it is feasible to impose an energy gate to select the low-energy region predominantly governed by resonances/levels with spins J = 2^+ or 3^+, as can be seen in Fig. 4.3 [47]. Hence, these two specific spin-parity combinations hold particular significance for the simulations. At low energies, the level density conforms to the 2J+1 law [48], where the level density serves as the reciprocal of the number of levels. Thus, the ratio of the number of J=2 levels to the number of J=3 levels can be determined as $(6+1)/(4+1) = 7/5$. Consequently, approximately 58% of the levels exhibit J=2^+ spin-parity, while 42% of the levels correspond to J=3^+ spin-parity configurations for low-energy neutron capture reaction.
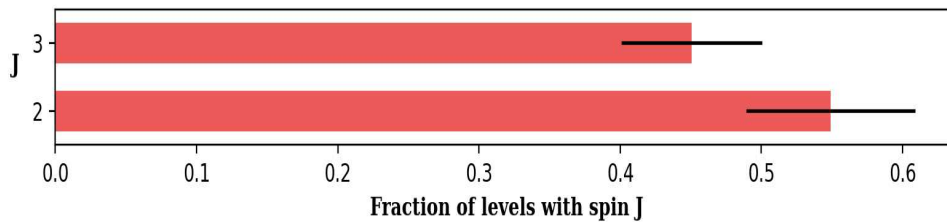
Figure 4.3: Proportion along with the statistical uncertainty of levels J=2^+ and J=3^+ for $l = 0$ at low neutron energy for resolved parameters between $10\mu eV < E < 300eV$ [47].

4.1.2 *Dicebox simulation results*

The spin and parity of a given state play a significant role in determining the probability and characteristics of γ-ray emissions, which in turn affect the energy and intensity distribution of gamma rays. In the current implementation of the DICEBOX simulation, only E1, M1, and E2 transitions are considered, except for transitions below the critical energy (E_{crit}). The emission of gamma cascades follows specific selection rules, as described in [49].

In this section, we present a selection of the key outcomes obtained from the DICEBOX simulation, with a specific focus on the 2^+ and 3^+ configurations as explained in Sec. 4.1.1. Additional results are provided in Appendix-I A.

Following the completion of the DICEBOX simulation, a post-processing method was developed to removed the contribution from transitions actually decaying by internal conversion of electrons (IC) in the spectrum. DICEBOX lacks simulation capabilities for X-rays, it utilizes a flag to determine the type of transition. In cases where gamma radiation is not emitted, it assumes an internal conversion process resulting in the ejection of an electron from the atom. However, DICEBOX does not incorporate the subsequent emission of X-rays during the rearrangement of electron shells. This correction made it possible to focus exclusively on the gamma cascade arising from the neutron capture reaction, which holds significant importance in cross-section measurements. As illustrated in Figure 4.4, it is evident that the impact of IC is particularly pronounced in the lower energy range of the spectra. It was calculated that 25% of the total spectra corresponds to IC, and this portion is removed from the overall spectra. Additionally, approximately 96% of the signal within the 0 to 200 keV energy range can be attributed to IC processes.
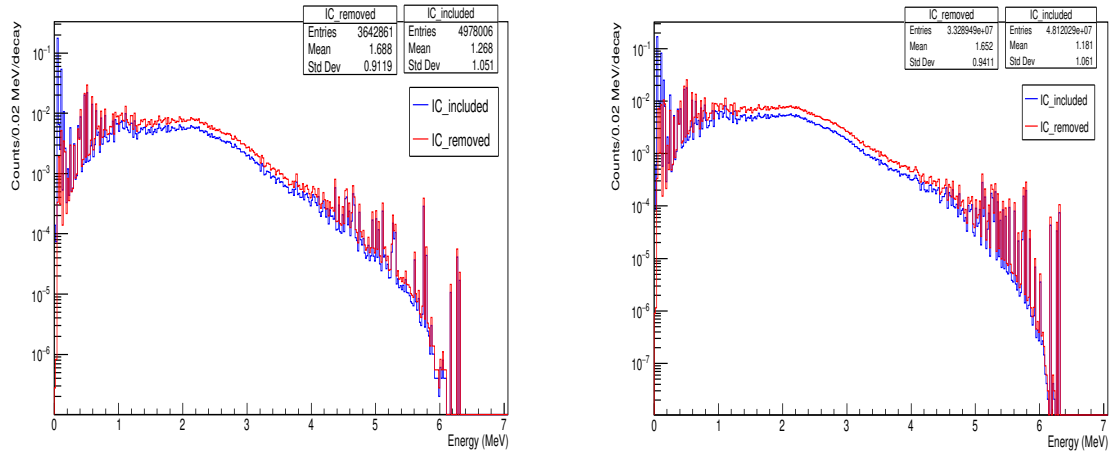
Figure 4.4: Simulated results with and without IC for I = 2^+ configuration(left) and all configurations combined(right).

In Fig. 4.5, we present the spectra corresponding to the I = 2^+ configuration, categorized based on the number of steps involved in the γ-cascade, also referred to as the multiplicity of the cascade. As shown in Fig. A.4 in the Appendix-I A, the maximum number of steps in the cascade observed for this case was 11.

With increasing multiplicity, it is expected that the mean of the spectrum decreases and shifts towards the left. This behavior is indeed observed as shown in Fig. 4.5, indicating that higher multiplicity cascades involve more numerous and lower-energy transitions. On the other hand, the spectrum corresponding to the multiplicity of 1 indicates the presence of some primary transitions, as anticipated.
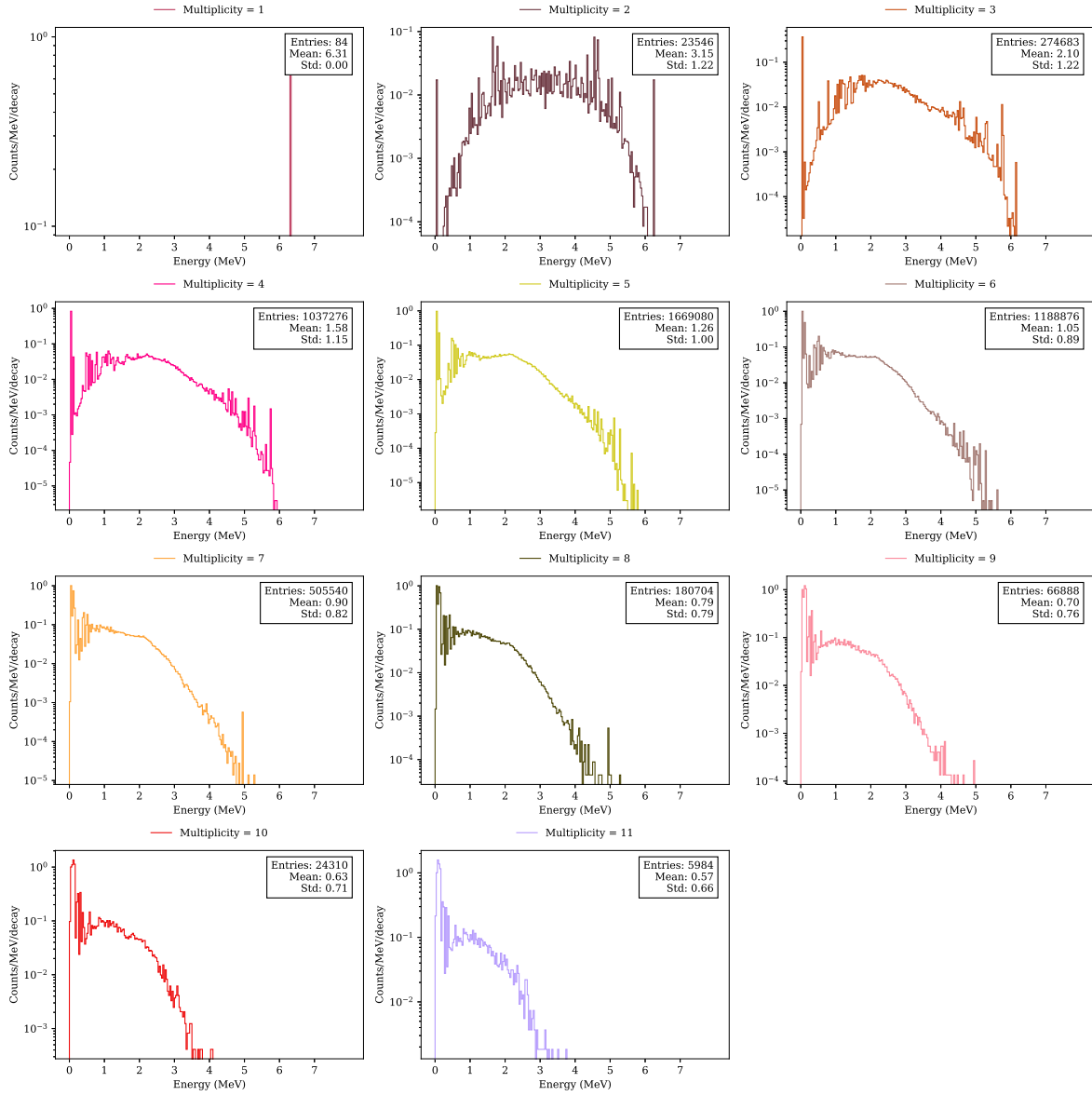
Figure 4.5: Decay of 2^+ level at S_n = 6.31 MeV of $^{241}Pu(n,\gamma)$ for different multiplicities.

It is worth noting that gamma emission from higher spin states can exhibit greater complexity and display more intricate fine structure due to the involvement of high-order multipole transitions.

Furthermore, the level scheme below the critical energy (E_{crit}) primarily consists of E1 and E2 type transitions. E1 transitions, in particular, exhibit a significant degree of collectivity, especially for low-lying E1 states, which can be described as giant resonances. The selection rules governing these transitions play a crucial role in determining the overall shape and intensity of the spectra, and the sophisticated modeling capabilities implemented in DICEBOX are essential for accurately capturing and simulating these intricate dynamics.

GEANT4 SIMULATION RESULTS

To examine the behavior of the Total Absorption Calorimeter (TAC), Geant4 simulations were initially performed using standard calibration sources as described in section 3.4.4. Subsequently, the γ-cascade output generated by DICEBOX was utilized as input for the next set of Geant4 simulations incorporating the TAC and the FICH. The simulation involved two sets of data: one set without IC correction (i.e. assuming transitions from one level to another is done by emitting gamma-rays), and another set with IC correction (i.e., excluding from the gamma spectra the transition done by internal conversion). By excluding the IC transitions in this data set, the specific influence of IC on the simulated TAC response can be evaluated.

In order to analyze the overall response of the 40 BaF_2 crystals, sum spectra were created for different multiplicities. These sum spectra were generated by adding up the energy deposited in all 40 crystals for each event. By summing the energy deposition across all crystals, the sum spectra provides a comprehensive view of the total energy response of the detector system. This allows for a better reconstruction of the sum peak near the S_n for $^{241}Pu(n,\gamma)$.
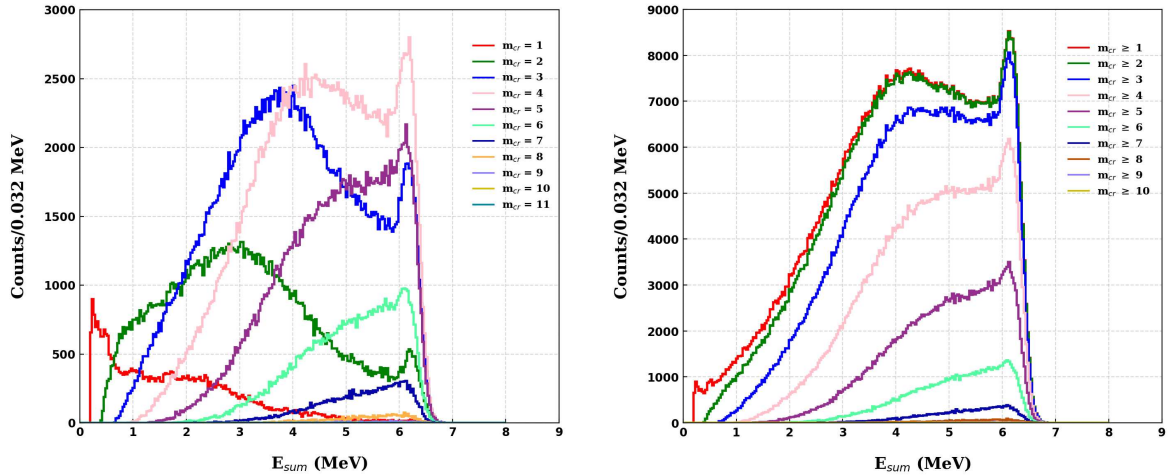
Figure 5.1: TAC response for γ-cascade emission from neutron capture in $^{241}Pu(2^+ state)$ configuration (without IC correction).

In Fig. 5.1 and Fig. 5.2, we present the E_{sum} spectra corresponding to different crystal multiplicities (m_{cr}) for the simulation of the ^{241}Pu capture measurement. Gating on the sum energy peak at 6.31 MeV allows for the investigation of the nuclear transitions within the ^{242}Pu nucleus by analyzing the multi-step cascade (MSC) spectra associated with individual multiplicities. Upon examining the multiplicity distribution in Fig. 5.4 in both cases, with and without IC correction, it can be observed that a majority of the γ-cascades consist of either 3 or 4 steps. With the application of $2.5MeV < E_{sum} < 6.5MeV$ cut Fig. 5.4 (Right), it becomes clear that for $m_{cr} = 3$ and 4, the contribution of gammas from neutron capture is much more important than the prompt fission gammas (PFG) discussed in the section 5.1. Although after taking into account the cross-sections for (n,γ) and (n,f) processes, it will be observed that the PFG will dominate as the ratio between the two is approximately a factor of three. But especially for small crystal multiplicities the background (scattered neutrons, fission-neutrons (FN), ambient and α-activity) will dominate the spectrum while the fission related prompt background is responsible for essentially all counts with $m_{cr} > 7$. Also from Fig. 5.3 which has the crystal multiplicity on y-axis after the Geant4 simulation and multiplicity of γ-cascade from DICEBOX
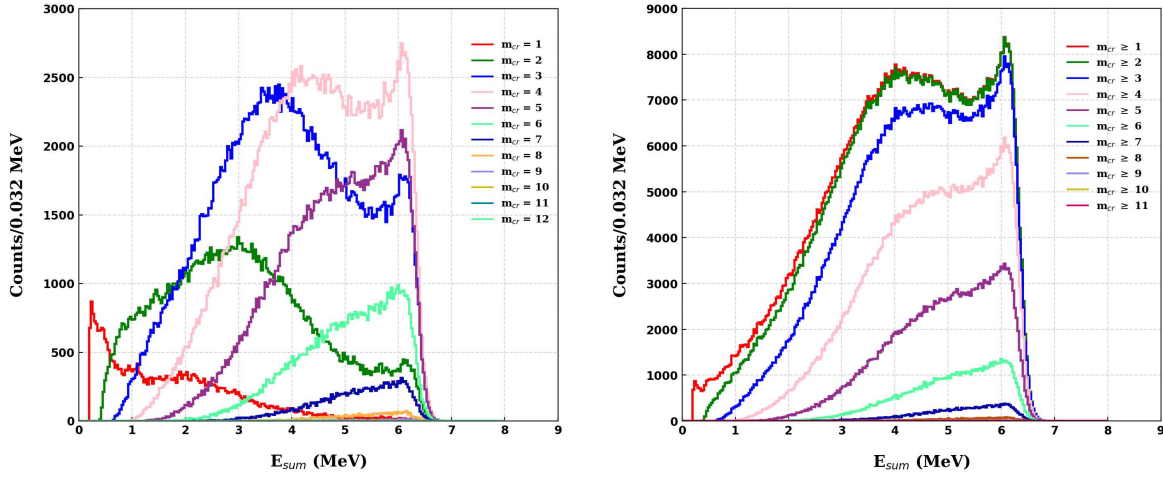
Figure 5.2: TAC response for γ-cascade emission from neutron capture in $^{241}Pu(3^+state)$ configuration (without IC correction).

on x-axis which was given as an input to Geant4, one can observe that most of the m_{cr} = 1 and 2 events come from $m_{\gamma\text{-cascade}}$ = 3, 4 and 5. This is a clear indication of partial reconstruction and consequently leads to a lower E_{sum} value for these events. The effect can clearly be seen for m_cr = 1 and 2 in Fig.5.2. The background unrelated to the ^{241}Pu samples is strongly discriminated for $m_{cr} \geq 3$. The PFG contribution is relatively lower for $m_{cr} \leq 7$ and there are almost no $^{241}Pu(n,\gamma)$ events above $m_{cr} \leq 7$, see Fig.5.4. Thus, the best conditions for the crystal multiplicity is $3 \leq m_{cr} \leq 7$ to improve the signal to background ratio.
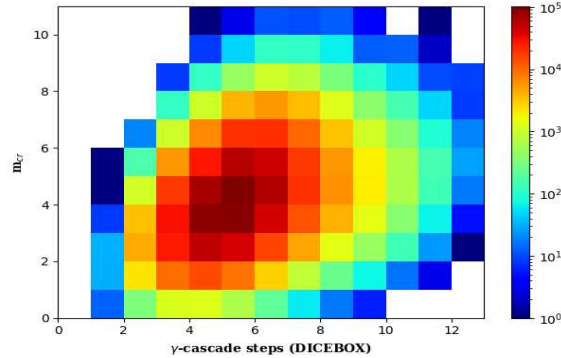
Figure 5.3: TAC crystal multiplicity (GEANT4) vs. cascade multiplicity (DICEBOX)

For smaller crystal multiplicities, such as $m_{cr} = 1$ and 2, the spectra are primarily dominated by background contributions due to neutron capture and scattering reactions in the absorber and the surrounding material, especially in the lower E_{sum} energy region below 2.5 MeV [50]. The main source of background in the lower energy range is related to the process of moderation. Particularly within the absorber, neutrons can undergo moderation and reach thermal energies. Subsequently, these neutrons may be captured in the absorber material or the borated carbon fiber shell encompassing the BaF_2 crystals. This capture process results in the emission of a single gamma-ray with an energy of either 2.22 MeV from $^1H(n,\gamma)$ or 0.48 MeV from $^{10}B(n,\alpha)$ [51]. Additionally, a portion of neutrons might escape the absorber and interact directly with the BaF_2 crystals. These direct reactions lead to signals in the TAC, specifically through the $(n,n'\gamma)$ reaction on ^{138}Ba, resulting in a gamma-ray with an energy of 1435 keV [52, 53]. Hence, to obtain reliable and meaningful results, it is recommended to utilize the spectra corresponding to $m_{cr} \geq 3$ for comparison with experimental data and for further refinement of the chosen photon strength functions.
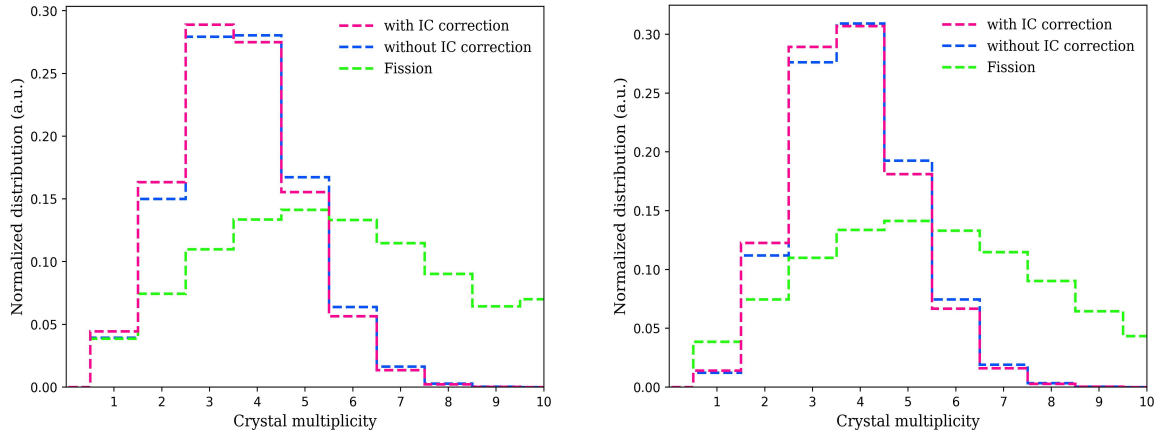
Figure 5.4: Crystal multiplicity distribution for γ-cascade in $^{241}Pu(n,f)$ and $^{241}Pu(n,\gamma)$, with and without IC correction for (2^+) level. Without cut (Left) and with cut (Right) on E_{sum} (see text).

By focusing on higher crystal multiplicities, the impact of background can be minimized, leading to more accurate and robust comparisons with experimental data. This also enables a more precise determination of the photon strength functions and contributes to the ongoing improvement of the models used to describe the nuclear transitions within the ^{242}Pu nucleus. In Fig. 5.5, where the spectra are corrected for IC, a clear distinction between the sum peak and the rest of the spectra can be observed.
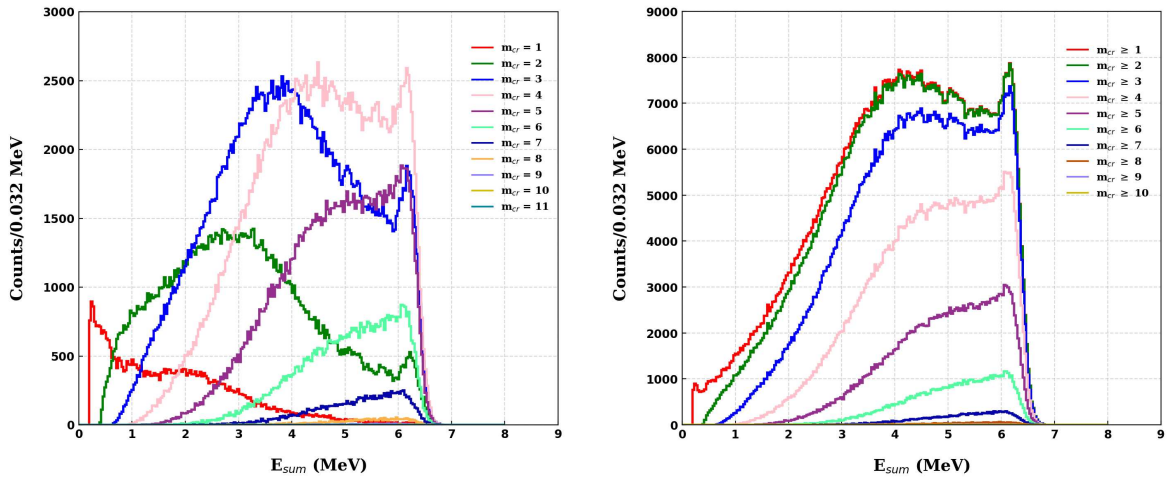
Figure 5.5: TAC response for γ-cascade emission from neutron capture in $^{241}Pu(2^+ state)$ configuration (with IC correction).

However, when considering $J = 3$ as shown in Fig. 5.6 and higher lying states, $J \geq 3$ shown in section A of Appendix-I, the distinction between the sum peak and the surrounding spectra becomes less apparent. There is not a clearly recognizable sum peak around 6.31 MeV.

To gain a better understanding of the reason behind the worsening resolution of the sum peak, it is helpful to examine the E_{sum} spectra before and after processing the DICEBOX results for IC correction.

In the case without IC correction, see Fig. 5.7(left), we observe that 99.9% of the cascades reach the ground level, resulting in a total cascade energy of 6.31 MeV. This leads to a sharp and well-defined sum peak centered at 6.31 MeV.

However, when we examine the E_{sum} spectra after post-processing the DICEBOX output and correcting the spectra for IC, see Fig. 5.7(right), we observe a different behavior. The distribution of sum energies becomes more continuous, with a peak centered around 6.31 MeV for cases
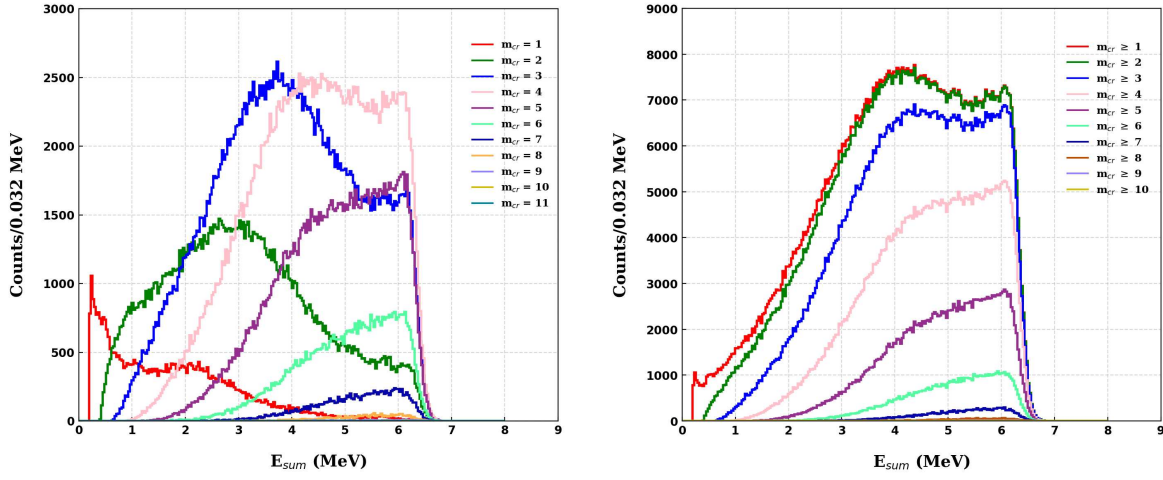
Figure 5.6: TAC response for γ-cascade emission from neutron capture in $^{241}Pu(3^+state)$ configuration (with IC correction).

where the cascade is complete. These specific cases account for a mere 5.2% of the overall events, as illustrated by the red line in Figure 5.7.

This discrepancy between the complete cascades and the overall distribution of sum energies explains the poor resolution of the sum peak in Fig. 5.6. The presence of incomplete γ-ray cascades due to IC introduce a broader energy distribution, resulting in a loss of the sharpness and clarity of the sum peak.
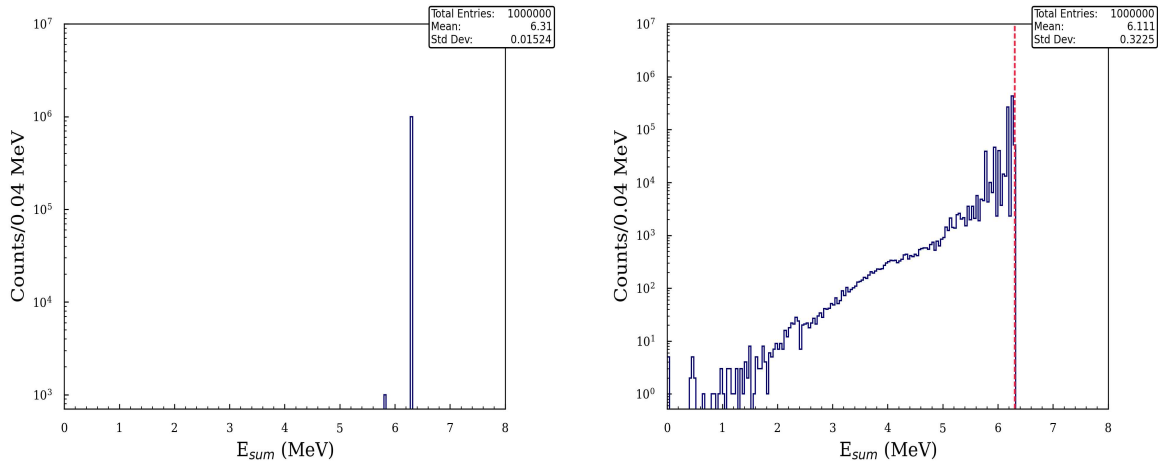
Figure 5.7: E_{sum} spectra of γ-cascade from n-capture in ^{241}Pu (3^+ state) configuration: Impact of neglecting IC (left) and correcting for IC (right)

For smaller crystal multiplicities, the spectra are still predominantly influenced by background, especially in the sum energy region below 2.5 MeV. To ensure more accurate calculations of the ^{241}Pu α-ratio, it is advisable to use events with 2.5 MeV < E_{sum} < 6.5 MeV and $m_{cr} \geq 3$. The implementation of the upper limit for the cut at 6.5 MeV prevents the inclusion of gamma rays originating from neutron capture in aluminum (Al) and barium (Ba) isotopes. In Table 5.1, you can find a list of the seven stable barium isotopes, along with their respective neutron separation energies and natural abundances.

Barium exhibits a significantly high neutron capture cross-section that varies depending on the isotope. This can be observed in the right panel of Fig. 5.8, where the neutron capture cross-sections for different barium isotopes are depicted, taking into account their respective natural abundances.

Table 5.1: Isotope Abundance (%) and S_n (MeV) for Barium Isotopes

Isotope	^{130}Ba	^{132}Ba	^{134}Ba	^{135}Ba	^{136}Ba	^{137}Ba	^{138}Ba
Abundance (%)	0.106	0.101	2.417	6.592	7.854	11.23	71.7
S_n (MeV)	7.494	7.190	6.972	9.108	6.906	8.612	4.723
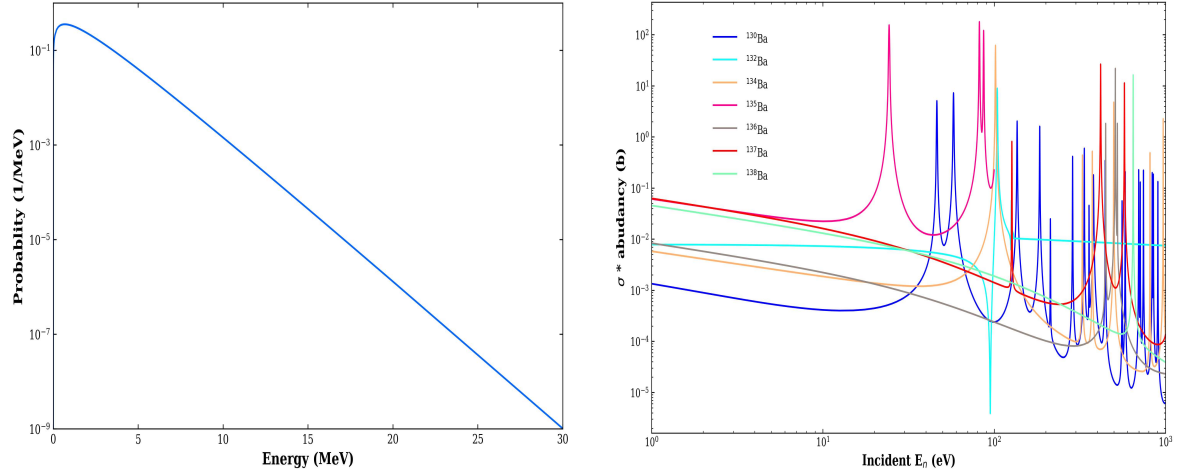
Figure 5.8: Fission neutron energy spectrum of ^{241}Pu taken from ENDF/B-VIII.0 (left). Capture cross sections of all stable barium isotopes weighted by their natural abundance (right).

The shape of the total capture cross-section of natural barium exhibits strong dependence on the neutron energy. This characteristic is due to the resonant behavior observed in the barium capture cross-section. This resonance phenomenon contributes to the energy-dependent behavior of the background observed in the TAC spectra. This background can be measured and subtracted using a dummy fission chamber (without sample). However, this is not possible for the background induced by the fission neutrons originated from the sample itself.

In order to be efficiently captured by a nucleus, fission neutrons need to be moderated, as the capture cross-sections generally become smaller for fast neutrons. 2.940±0.013 fission neutrons are released per fission reaction reaction $^{241}Pu(n,f)$. It's important to note that, on average, the moderation process for emitted fission neutrons is similar. As a result, the shape of the background due to these neutrons does not depend on the time-of-flight (TOF). Thus, it is possible to use an average shape for the background correction, which will simplify the analysis.

In addition due to the neutron separation energy of ^{242}Pu of 6.31 MeV there is no $^{241}Pu(n,\gamma)$ reaction detected above 6.5 MeV. By excluding this region, the signal-to-background ratio will be improved. Therefore the best conditions applied to E_{sum} to improve the signal to background ratio are 2.5 MeV < E_{sum} < 6.5 MeV.

The efficiency of the detector system can be calculated straightforwardly from simulations. This involves taking the ratio of the registered cascades that fulfill the specified analysis conditions (i.e., $m_{cr} \geq 3$ and 2.5 MeV $< E_{\text{sum}} < 6.5$ MeV) to the total number of cascades simulated. The efficiency values obtained under various conditions are summarized in Table 5.2. Additionally, it was seen that by implementing the upper threshold of this cut at 6.5 MeV, there is no loss in efficiency, see Fig. B.20.

5.1   PROMPT FISSION γ-RAY SPECTRA

The simulations of the production and detection of the prompt fission γ-rays (PFG) were also carried out in Geant4. The geometry of the TAC and FICH is implemented in Geant4 as

Table 5.2: TAC efficiency ϵ_{TAC}^{γ} for $^{241}Pu(n,\gamma)$ cascades for different multiplicity conditions for 2.5 MeV $< E_{\text{sum}} < 6.5$ MeV with statistical uncertainty.

$m_{cr} \geq$	ϵ_{TAC}^{γ} %
1	89.16 ± 0.07
2	88.83 ± 0.07
3	83.07 ± 0.07
4	62.68 ± 0.05
5	33.89 ± 0.04
6	12.66 ± 0.02
7	3.25 ± 0.01

described in section 3.4 and the events are generated from the probability distribution given by a model developed by M. Jandel at Los Alamos [1]. This model correlates the emitted γ-ray energy E_γ and the number of emitted γ-rays M_γ per fission. It was developed to derive the properties of the PFG. The PFG emission is described by a two-component spectrum in this model. The distributions of the multiplicity $p_{1,2}(M_\gamma)$ and γ-ray energy $p_{1,2}(E_\gamma)$ are assumed in the following form:

$$p_{1,2}\left(M_\gamma\right) = \left(2M_{1,2} + 1\right) e^{-M_{1,2}(M_{1,2}+1)/c_{1,2}^2}, \quad p_{1,2}\left(E_\gamma\right) = \frac{dN_\gamma}{dE_\gamma} \propto E_\gamma^{l_{1,2}} e^{-t_{1,2}E_\gamma} \tag{5.1}$$

where $l_1 = 2$, $l_2 = 3$, and E_γ spectra as a function of the PFG multiplicity M_γ = M1 + M2 using:

$$t_{1,2} = a_{1,2} + b_{1,2}M_\gamma \tag{5.2}$$

In the context of fission, "1" and "2" refer to the light and heavy fragments produced during the fission process. The multiplicty distribution and E_γ spectra of which is given in Fig. 5.9. The energy of PFG released by heavy fission fragments are higher as compared to the lighter fragment. This is due to the fact that heavy fragments have more protons and neutrons, resulting in higher excitation energies and larger energy releases during the de-excitation process.
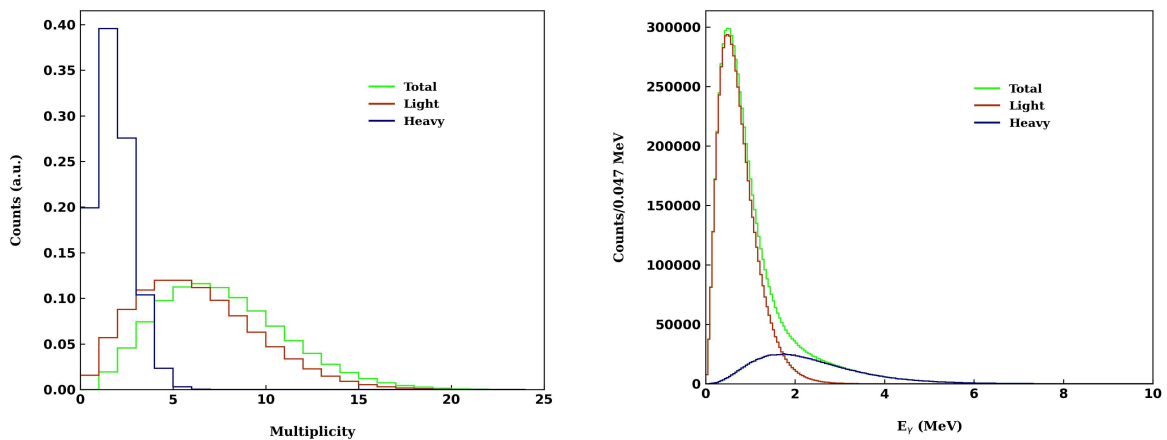
Figure 5.9: Total PFG M_γ distribution and E_γ spectra for both fission fragments using the Los Alamos model [1].

Table 5.3: Coefficients of parametrization of PFG emission in neutron induced fission for incident energies between 4 eV and 500 keV.

	c1	c2	a1	b1	a2	b2
LANL-DANCE [1]	7.11	2.14	3.618	0.0454	1.403	0.0438

PFG radiation amounts on average to only 3% of the total energy released in fission. After neutron emission, their emission occurs largely for fission fragments with low excitation energy. The typical timescale for PFG emission is in the range of a few times 10^{-14} s to a few times 10^{-11} s [54]. Typically, PFG spectral intensities are measured by γ-ray sensitive detectors, in coincidence with fission-fragment detectors such as TAC and FICH in our set-up. The coefficients of parametrization of PFG emission in for neutron induced fission in ^{241}Pu were taken the same as for ^{239}Pu due to unavailability of parameters for ^{241}Pu. Doing so makes sense because both the isotopes are odd fissile isotopes of plutonium differing only by two neutrons. Also, similar results were obtained for PFG spectra for ^{239}Pu and ^{241}Pu in measurements using the Detector for Advanced Neutron Capture Experiments (DANCE) set-up at the Los Alamos laboratory [55].

The Los Alamos PFG generator [1] was used with optimized parameters as suggested in [1] which were adapted to fission reactions for neutron energies in the range of 4 eV to 500 keV. The parameters are summarized in Table 5.3.

It should be noted that the experimental spectra may differ from the simulated spectra as the energy range for the neutrons for the real experiment might be different and fast neutrons can add energy and angular momentum to the process, thereby affecting the sum spectra resulting from the transport of γ-rays in the TAC array. Later, an optimised set of parameters can be used to obtain good agreement between the experimental and simulated results. The high energy continuum and low energy transitions are two distinct sections of the prompt fission gamma spectrum (PFGS). The emission of prompt fission γ-rays is influenced by the parent fragment. The Prompt Fission Gamma Spectrum (PFGS) is primarily composed of statistical γ-rays with exit energies surpassing 1 MeV from the Giant Dipole Resonance (GDR) and collective de-excitation along the yrast line [56]. However, notable spectral features can be observed predominantly below 1 MeV [57, 58]. These features correspond to specific γ-ray transitions between low-lying excited states in the fission fragments which result in a reduction of the fragment spin. But we get a smooth spectra as a result of the DANCE model's assumption of a certain distribution for E_γ, see Eq. 5.1, this feature remains unnoticed within the spectra, see Fig.C.1.

The response of TAC to PFG is shown in Fig. 5.10. With the constraints on the crystal multiplicity $m_{cr} \leq 20$ and the threshold for prompt fission γ detection E_{thresh} = 200 keV the total γ-ray energy vs multiplicity is shown in Fig. 5.11 (right). As expected, with increasing M_γ the $E_{\gamma tot}$ is increasing. The outgoing γ-ray energy, E_γ spectra can be seen on the left panel of the figure. The average properties of PFG emission are summarized in Table 5.4. The values obtained are close to the obtained values after simulation in Jandel's previous work [1]. In addition to average values of the PFG multiplicity $< M_\gamma >$, energy $< E_\gamma >$ and total energy $< E_{\gamma tot} >$, we also report the values of the standard deviations of these distributions and a comparison with the ENDF data and other results is also given. Note that some experiments have reported either $< E_{\gamma tot} >$ or the $< E_\gamma >$.
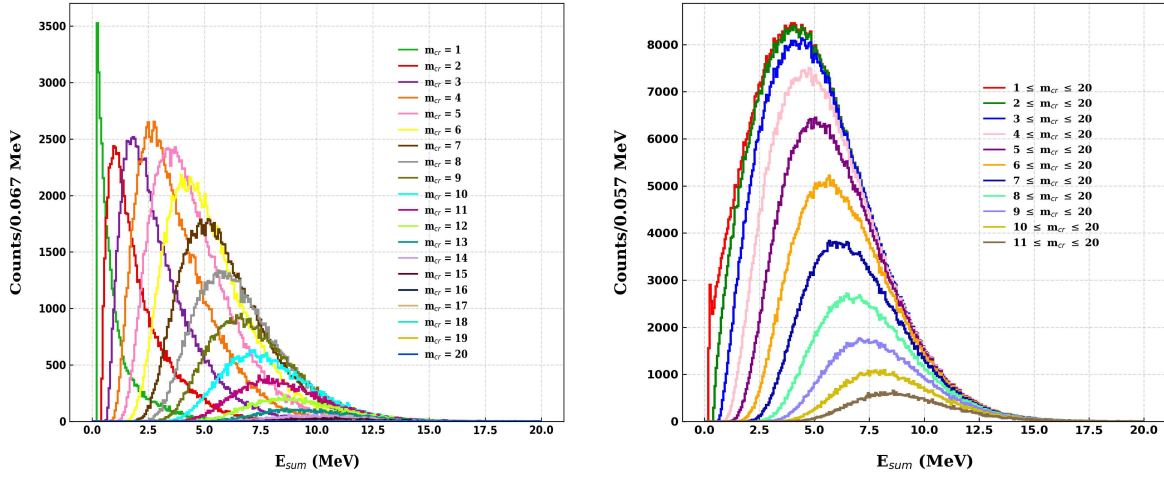
Figure 5.10: (Left)Total PFG energy spectra as simulated in the TAC array for E_{thresh} = 200 keV for different PFG multiplicities from $M_\gamma = 1 - 20$. (Right) PFG energy spectra with different conditions on M_γ.
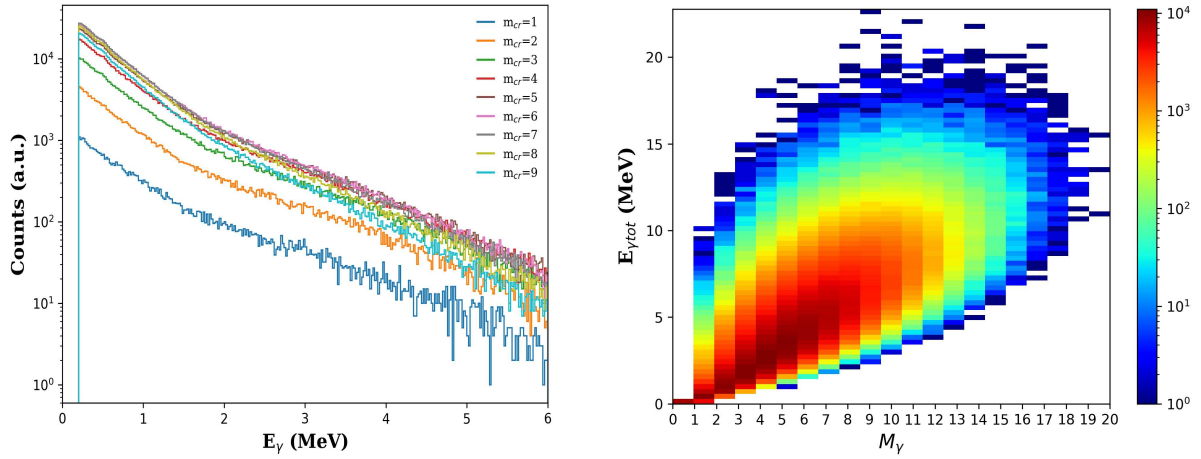
Figure 5.11: (Left) Individual prompt fission γ-ray spectra. (Right) Total prompt fission γ-ray energy vs cluster multiplicity for the neutron-induced fission of ^{241}Pu.

Table 5.4: Average multiplicity M_γ, average energy E_γ, and total energy $E_{\gamma\,tot}$ for the PFGS

	$< M_\gamma >$	$\sigma(M_\gamma)$	$< E_{\gamma\,tot} >$	$\sigma(E_{\gamma\,tot})$	$< E_\gamma >$	$\sigma(E_\gamma)$
	[γ/fission]		[MeV/fission]		[MeV/γ]	
This work	7.17	3.41	7.44	3.41	1.04	0.89
^{239}Pu, Ref.[1]	7.1	3.31	7.4	3.58	1.05	0.87
^{241}Pu, ENDF/B-VII.1	8.18		7.64		0.87	
^{239}Pu, ENDF/B-VII.1	7.78		6.74		0.87	
^{239}Pu, $E_{thresh} = 0.14 MeV$ Ref.[59]	7.23		6.81		0.94	
^{239}Pu, $E_{thresh} = 0.15 MeV$ Ref.[60]	7.15		7.46			
^{241}Pu, $E_{thresh} = 0.15 MeV$ Ref.[61]	7.93		6.94			

6

CONCLUSION

A better understanding of neutron capture cross-section of ^{241}Pu is essential for the future of the nuclear energy production. This is the challenge that the future n_TOF experiment aims to solve. This report describes numerical simulations performed to investigate the neutron capture and fission reaction in ^{241}Pu, and provides the expected performance of the TAC. We successfully modelled the γ cascades from ^{241}Pu capture and fission using DICEBOX[17] and LANL-DANCE[1] code, respectively. γ-cascades were transported in the geometrical model of the experimental setup with the help of the Geant4 toolkit [26], leading to an efficiency of the TAC to detect at least one gamma in the ^{241}Pu(n,γ) cascade within the analysis conditions of $m_{cr} \geq 3$ and 2.5 MeV $< E_{\text{sum}} <$ 6.5 MeV):

$$\epsilon_{TAC}^{\gamma} = (83.07 \pm 0.07)\% \tag{6.1}$$

The results also suggest that we could use scintillators with better resolution like $LaBr_3$ than the BaF_2 crystals in TAC for better results and cut definitions, see Table. 3.1. Replacing the passive absorber with an active alternative, such as coupling a plastic scintillator with a silicon photomultiplier readout, offers the possibility of improving the signal differentiation of (fission) neutrons in the TAC. In addition, this modification could also allow the measurement of the average number of neutrons emitted per fission event. Furthermore, we also tried to explain the strange 300 keV gammas, especially in the simulation with a bi-gamma source such as ^{88}Y and the neutron absorber.

The simulation has proven to be essential in achieving two primary objectives. Firstly, by accurately modelling the gamma emission from the ^{241}Pu capture and fission reactions, the simulations have provided crucial pre-experimental insight, enabling us to anticipate and understand the expected results. This understanding has demonstrated the feasibility of the whole endeavour for the future experiment planned in 2025, alongside guiding the experimental design for the set-up. Secondly, these simulations play a vital role in accounting for any missed events due to experimental constraints or the cuts in the post-experimental data filtering processes. They also serve as the basis for calculating the detection efficiency of the entire setup. This complex analysis helps us refine the experimental results, ensuring the accuracy and reliability of the data obtained.

In the future, additional simulations exploring the influence of ^{241}Am production within the ^{241}Pu sample should be included. This extension will allow a deeper understanding of the interplay between ^{241}Pu and ^{241}Am contributions to the gamma spectra, providing insights into the dynamic behaviour of the experimental system. It will be useful to see the relative contributions of ^{241}Pu and ^{241}Am to the γ spectra over time (at the start of the measurement and at the end of the measurement). Simulation with ^{239}Pu could also be included as this will be a contaminant present in the sample. Other than this, extensive simulation for PFG can be carried out using GEF code[62], and the model of Valentine[63] to further compare the experimental spectra and get a model works which works the best for ^{241}Pu(n,f).

With the measurement scheduled for 2025, these simulations will play a crucial role in guiding the experimental process and ensuring the accurate interpretation of the data collected. The combination of pre-experimental simulation, post-experimental analysis and exploration of different scenarios exemplifies the critical role that simulation methods play in advancing the cross-section measurements with more accuracy.

This section focuses on the DICEBOX algorithm and presents the results obtained from the DICEBOX simulation, encompassing data for higher spin values as well.

The following describes the procedure for generating the de-excitation from the initial level to the final state:

1. The discretization of the level density $\rho\left(E, J^{\pi}\right)$ yields energies E_a, spins J_a, and parities of individual levels above the critical energy E_{crit}. Hereafter, for the sake of simplicity, the levels are labeled as integer numbers (a=1, 2,..., n), with the assumption that energy E_a decreases as a increases. Levels $a = 1$ and $a = n$ represent the initial level, where all cascades begin, and the ground state, where they stop.

2. Each level with $E_a > E_{crit}$ is assigned a generator seed α_a, Fig.A.1.

3. Generation of partial widths $\Gamma_{a\gamma a'}$ for a complete set of transitions $a \longrightarrow a'$ leading from the initial level a to all possible final levels a' with $E_{a'} > E_{crit}$.

4. The total radiation width $\Gamma_{a\gamma}$ is calculated for the initial level a:

$$\Gamma_{a\gamma} = \sum_{a'>a} \Gamma_{a\gamma a'} \tag{A.1}$$

5. A full set of branching intensities $I_{aa'}$ for all the transitions initiating at the level a are then determined following a simple expression:

$$I_{aa'} = \frac{\Gamma_{a\gamma a'}}{\Gamma_{a\gamma}} \tag{A.2}$$

6. A level a_1, to which the initial level a decays, is determined by a random number s_1 fulfilling the requirement

$$\sum_{a'=a+1}^{a_1-1} I_{aa'} \leq s_1 < \sum_{a'=a+1}^{a_1} I_{aa'} \tag{A.3}$$

   resulting in a known level a_1 reached by a step of the cascade.

7. If $E_{a_1} < E_{crit}$ the branching intensities $I_{a_1 a'}$ are deduced from the evaluated ENSDF data exclusively and the decay is computed from these data until a final level of a cascade is reached. If $E_{a_1} \geq E_{crit}$ the substitution $a_1 \longrightarrow a$ is performed and the items 3-6 are repeated until a level a_k with $E_{a_k} < E_{crit}$ or a final level of a cascade is reached. The final level of a cascade is either the ground state or an isomer with a half-life on the level of the experimental time window.

Understanding the process is facilitated by an illustration in Fig.A.1.
The simulated spectra corresponding to all the possible configurations up to $l = 2$, as outlined in Table 4.2, are presented here. Additionally, we provide a detailed account of the multiplicity distribution before and after the implementation of the IC correction method. The mean and standard deviation (SD) values corresponding to various cases have been concisely presented in Table A.1. Fig. A.3 presents spectra corresponding to different multiplicities for $J^{\pi} = 1^+$ state.
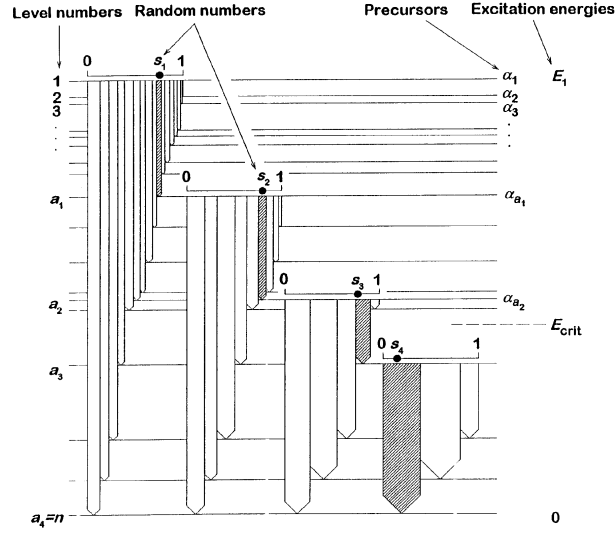
Figure A.1: Schematic description of gamma cascading
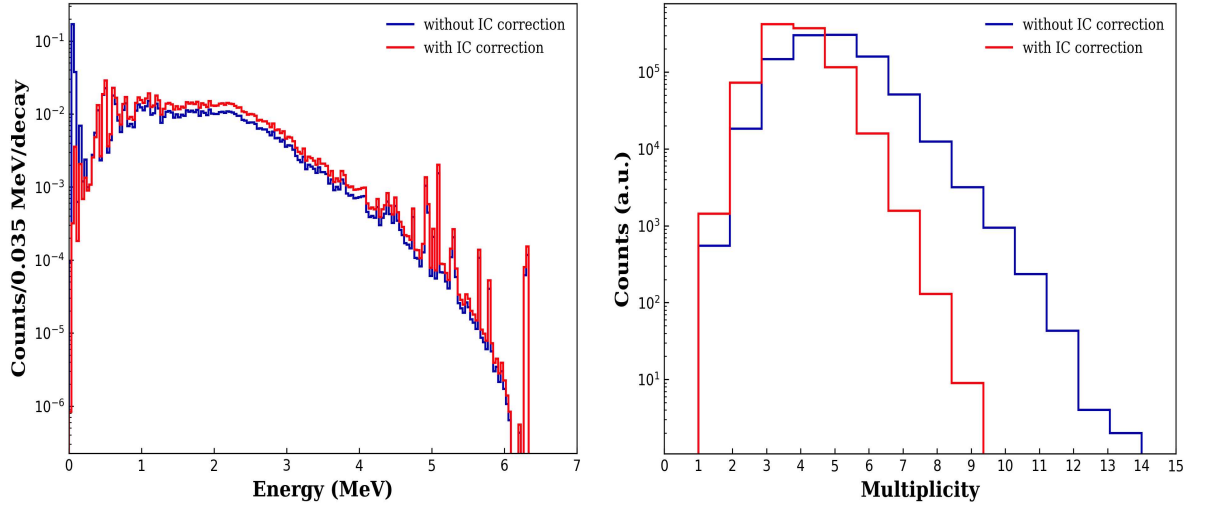
Figure A.2: DICEBOX results with and without IC correction (Left) and their multiplicity distribution (Right) for $J^\pi = 1^+$ configuration.

Table A.1: Statistical analysis of different DICEBOX results (SD stands for standard deviation).

Level	Without IC correction			With IC correction		
	Tot. Entries	Mean	SD	Tot. Entries	Mean	SD
1^+	4663523	1.35	1.05	3581035	1.73	0.91
1^-	4638099	1.36	1.07	3565735	1.73	0.93
2^+	4978006	1.27	1.05	3642861	1.69	0.91
2^-	4962482	1.27	1.08	3629626	1.69	0.93
3^+	5393808	1.17	1.05	3710852	1.65	0.93
3^-	5405379	1.17	1.05	3717552	1.64	0.93
4^+	5859173	1.08	1.05	3780312	1.60	0.96
4^-	5875228	1.07	1.05	3786095	1.60	0.96
5^+	6344592	0.99	1.04	3875420	1.55	0.98
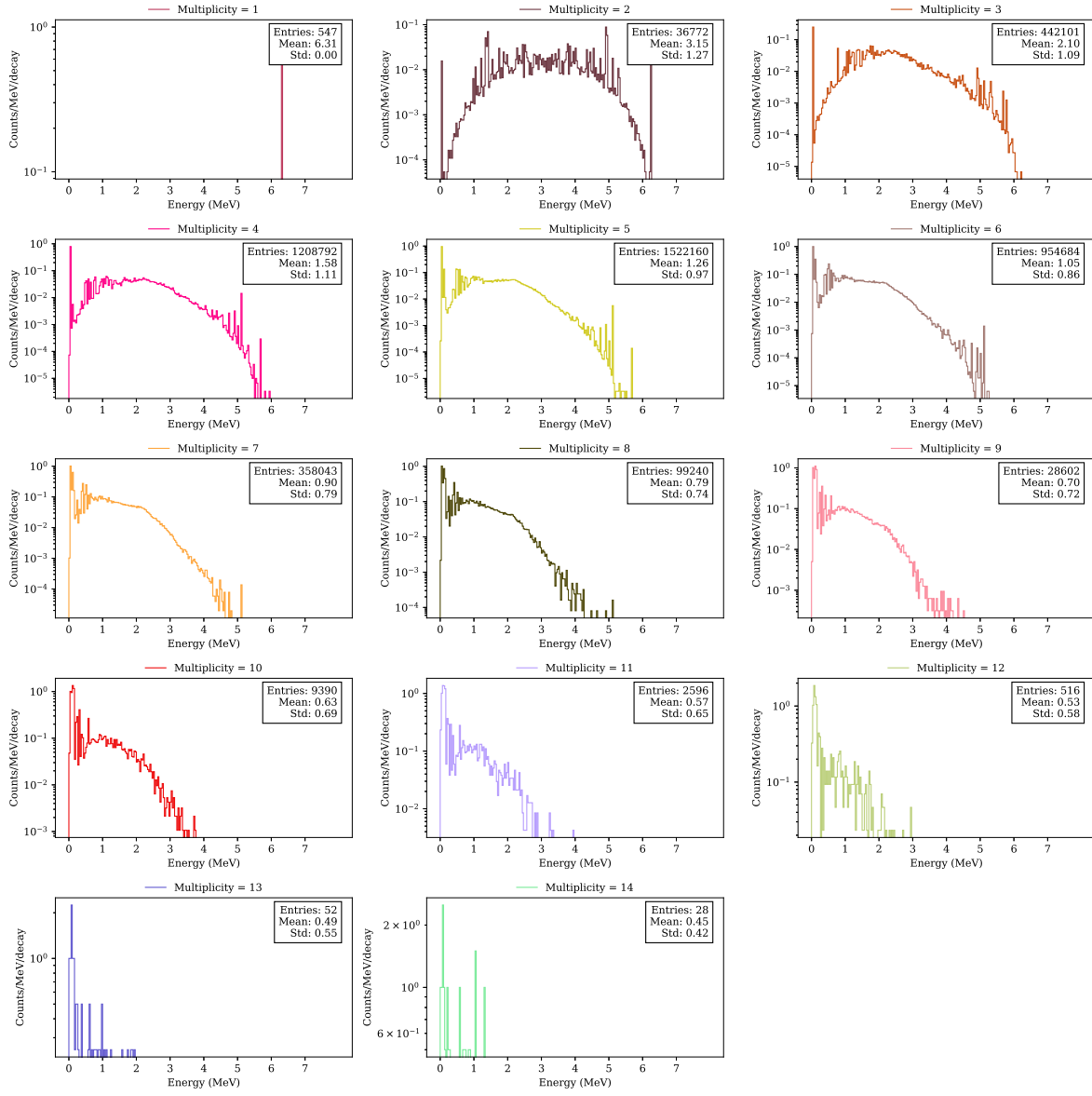
Figure A.3: Decay of 1^+ level at S_n = 6.31 MeV of $^{241}Pu(n, \gamma)$ for all crystal multiplicities (separated).
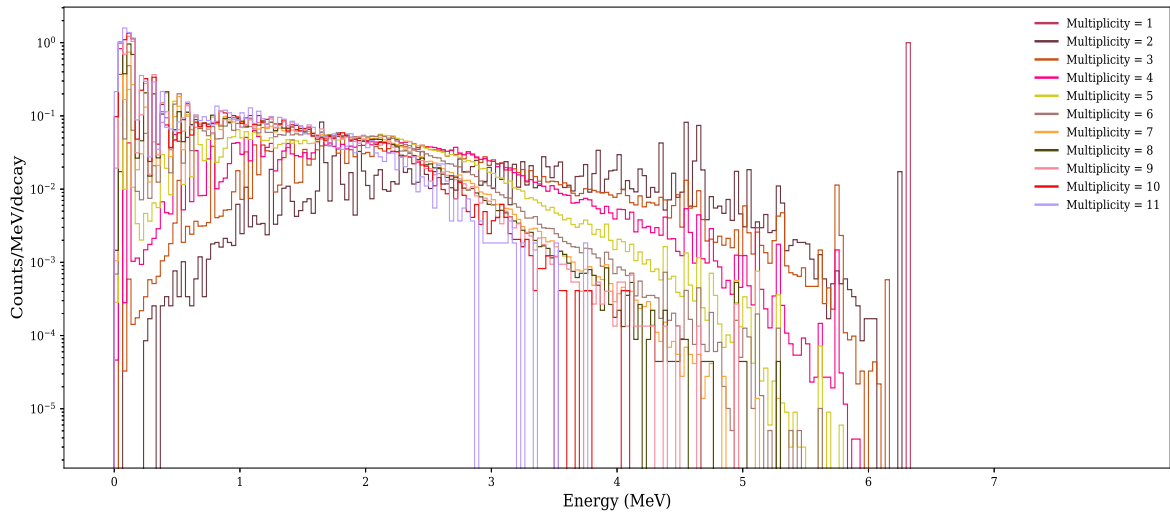
Figure A.4: Decay of 2^+ level at S_n = 6.31 MeV of $^{241}Pu(n, \gamma)$ for all different crystal multiplicities.
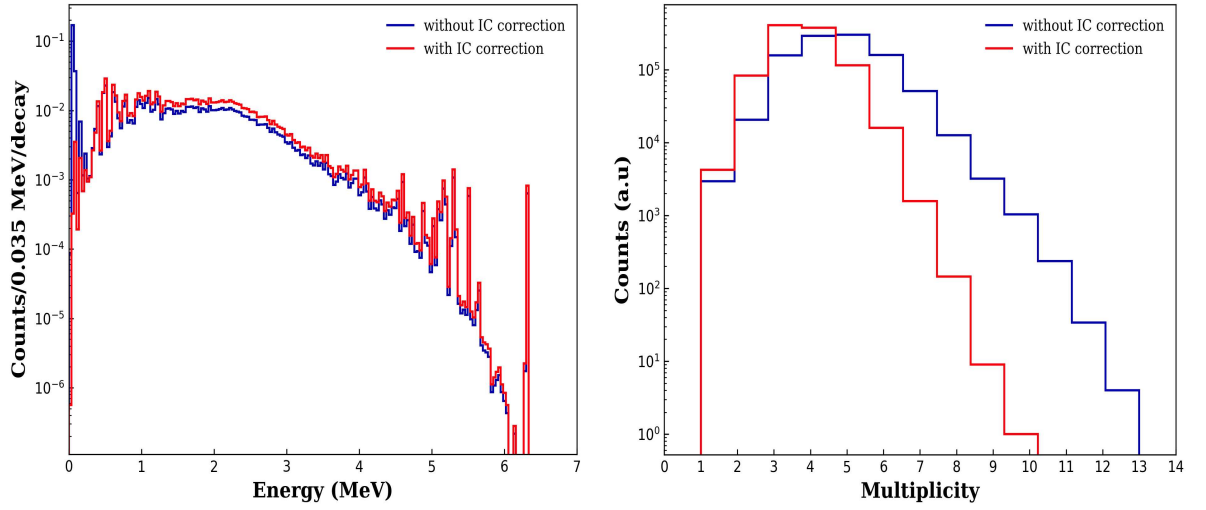
Figure A.5: DICEBOX results with and without IC correction (Left) and their multiplicity distribution (Right) for $J^{\pi} = 1^{-}$ configuration.
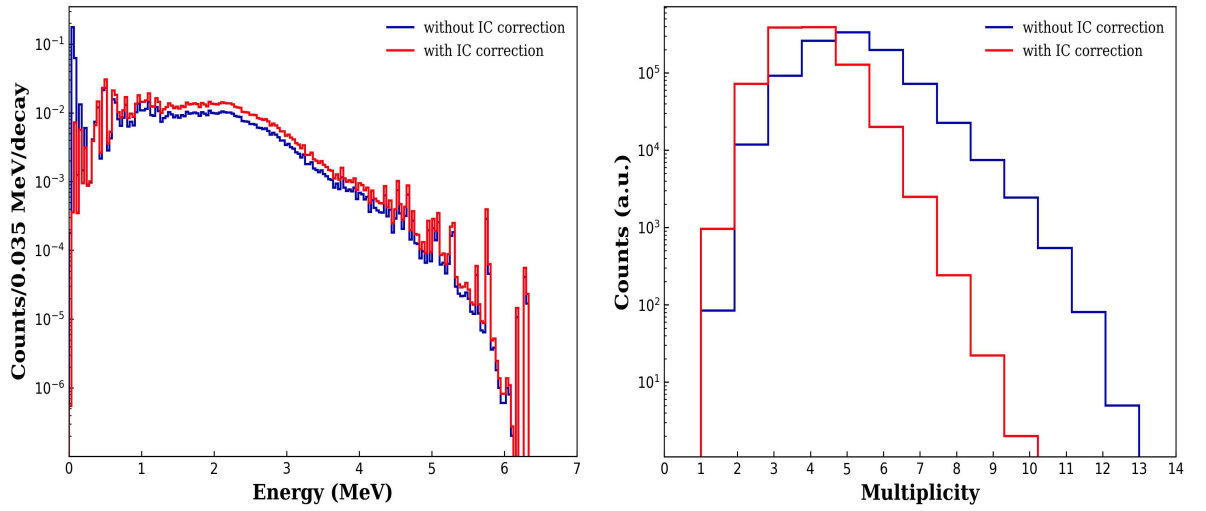
Figure A.6: DICEBOX results with and without IC correction (Left) and their multiplicity distribution (Right) for $J^{\pi} = 2^{+}$ configuration.
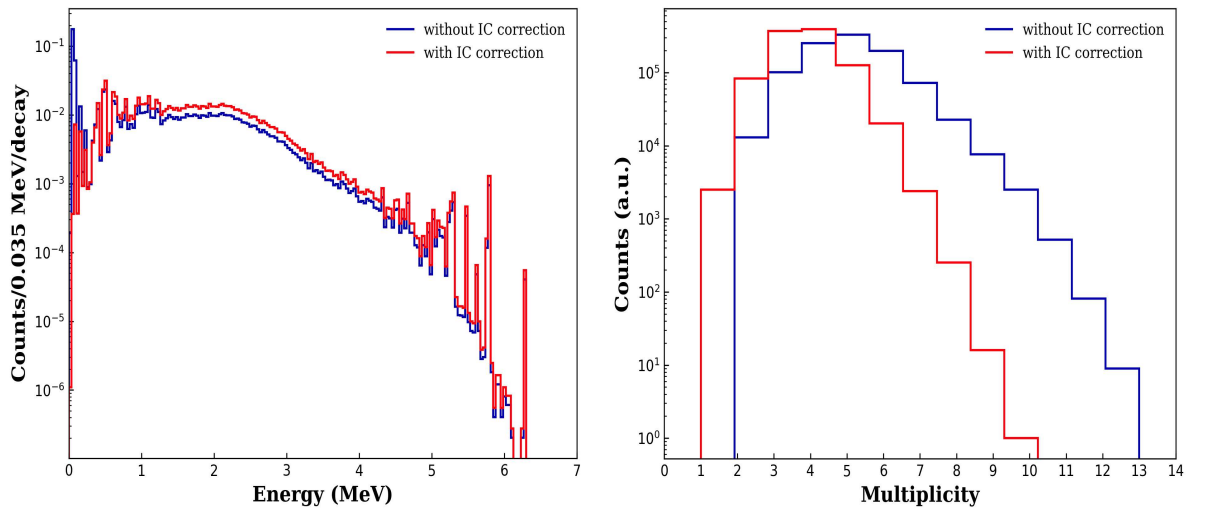
Figure A.7: DICEBOX results with and without IC correction (Left) and their multiplicity distribution (Right) for $J^{\pi} = 2^{-}$ configuration.
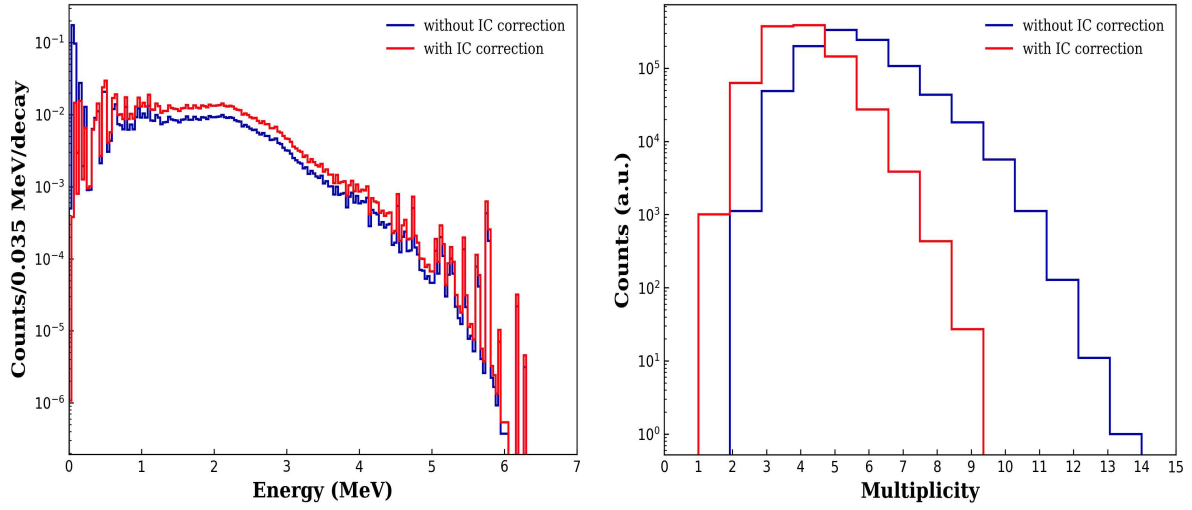
Figure A.8: DICEBOX results with and without IC correction (Left) and their multiplicity distribution (Right) for $J^\pi = 3^+$ configuration.
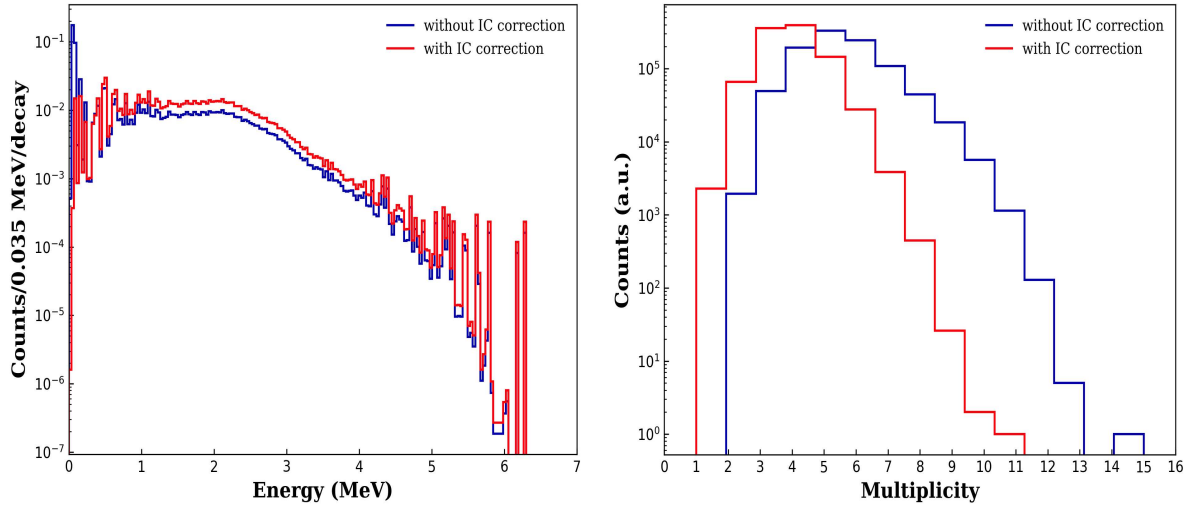
Figure A.9: DICEBOX results with and without IC correction (Left) and their multiplicity distribution (Right) for $J^\pi = 3^-$ configuration.
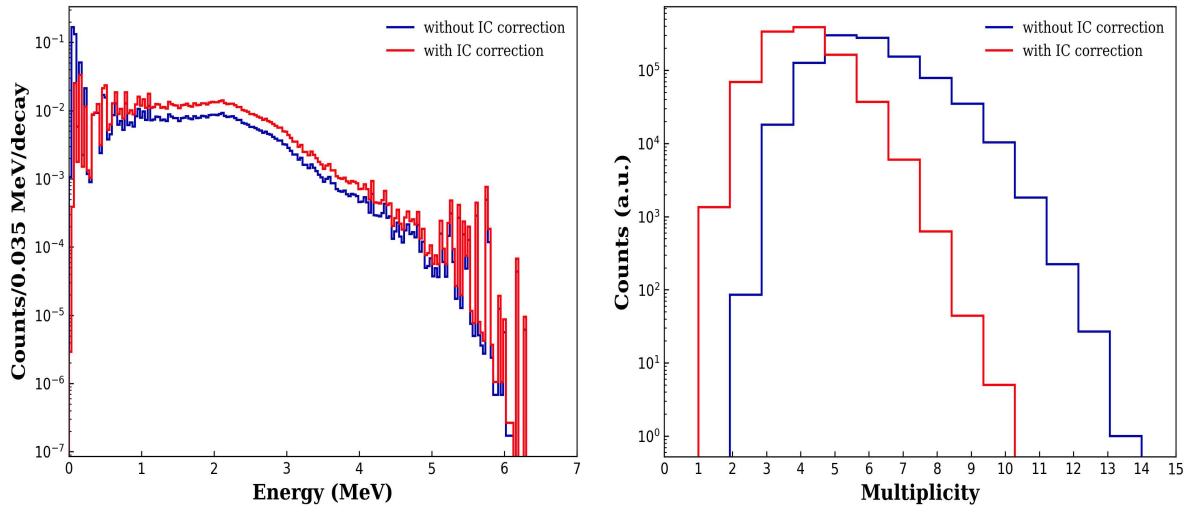
Figure A.10: DICEBOX results with and without IC correction (Left) and their multiplicity distribution (Right) for $J^\pi = 4^+$ configuration.
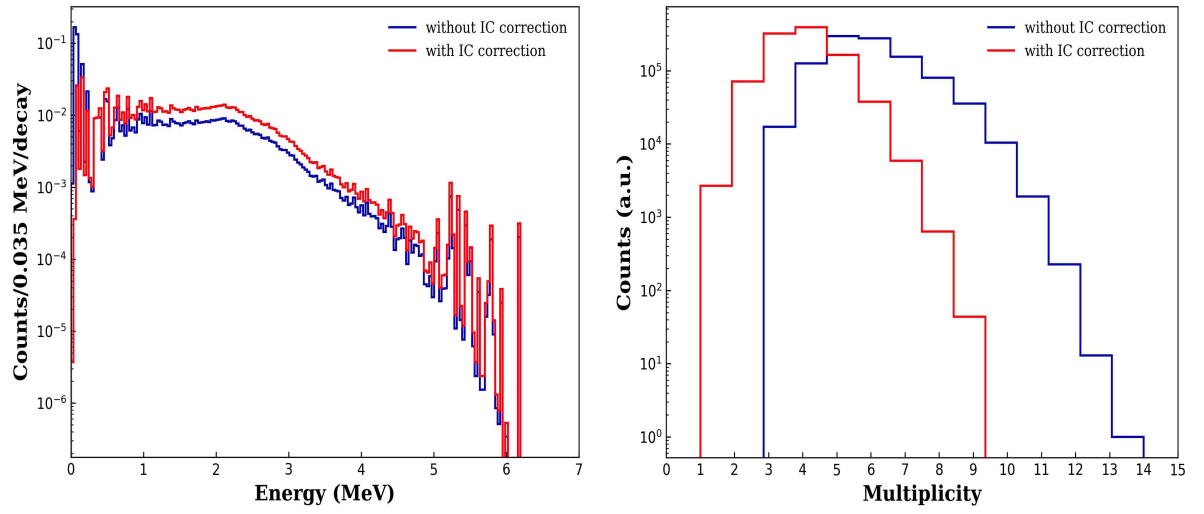
Figure A.11: DICEBOX results with and without IC correction (Left) and their multiplicity distribution (Right) for $J^\pi = 4^-$ configuration.
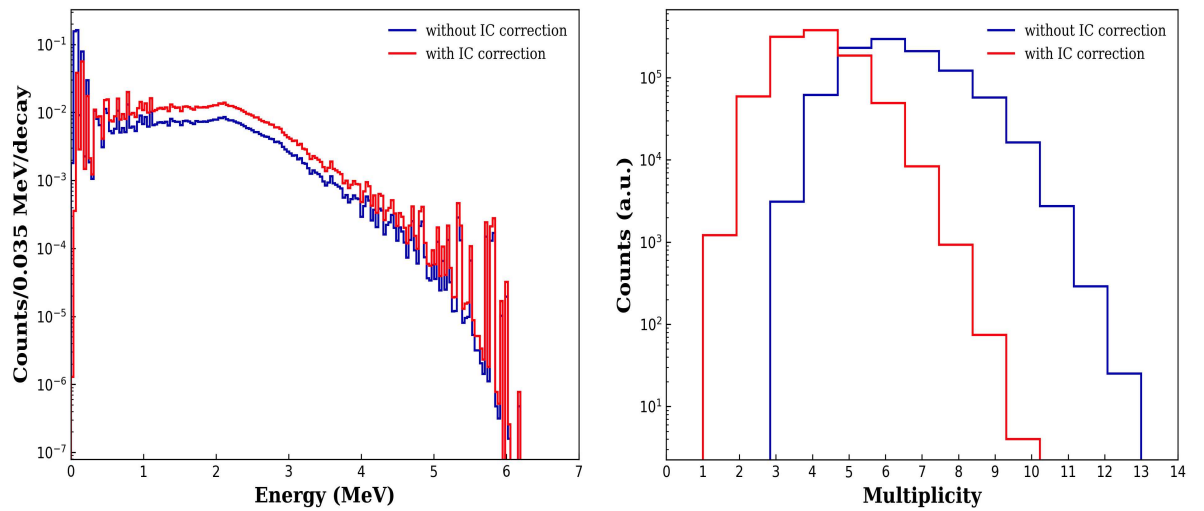
Figure A.12: DICEBOX results with and without IC correction (Left) and their multiplicity distribution (Right) for $J^\pi = 5^+$ configuration.

B

This section provides additional information on the geometry of experimental set-up, calibration and Geant4 simulation results.

The energy deposited in the crystal is directly proportional to the integrated area of the signal. In order to establish an accurate energy calibration, a correlation was established between the signal region and the known γ-ray energies (E_γ) of the calibration sources. Fig. B.1 depicts the response of the BaF$_2$ module to the calibration sources.
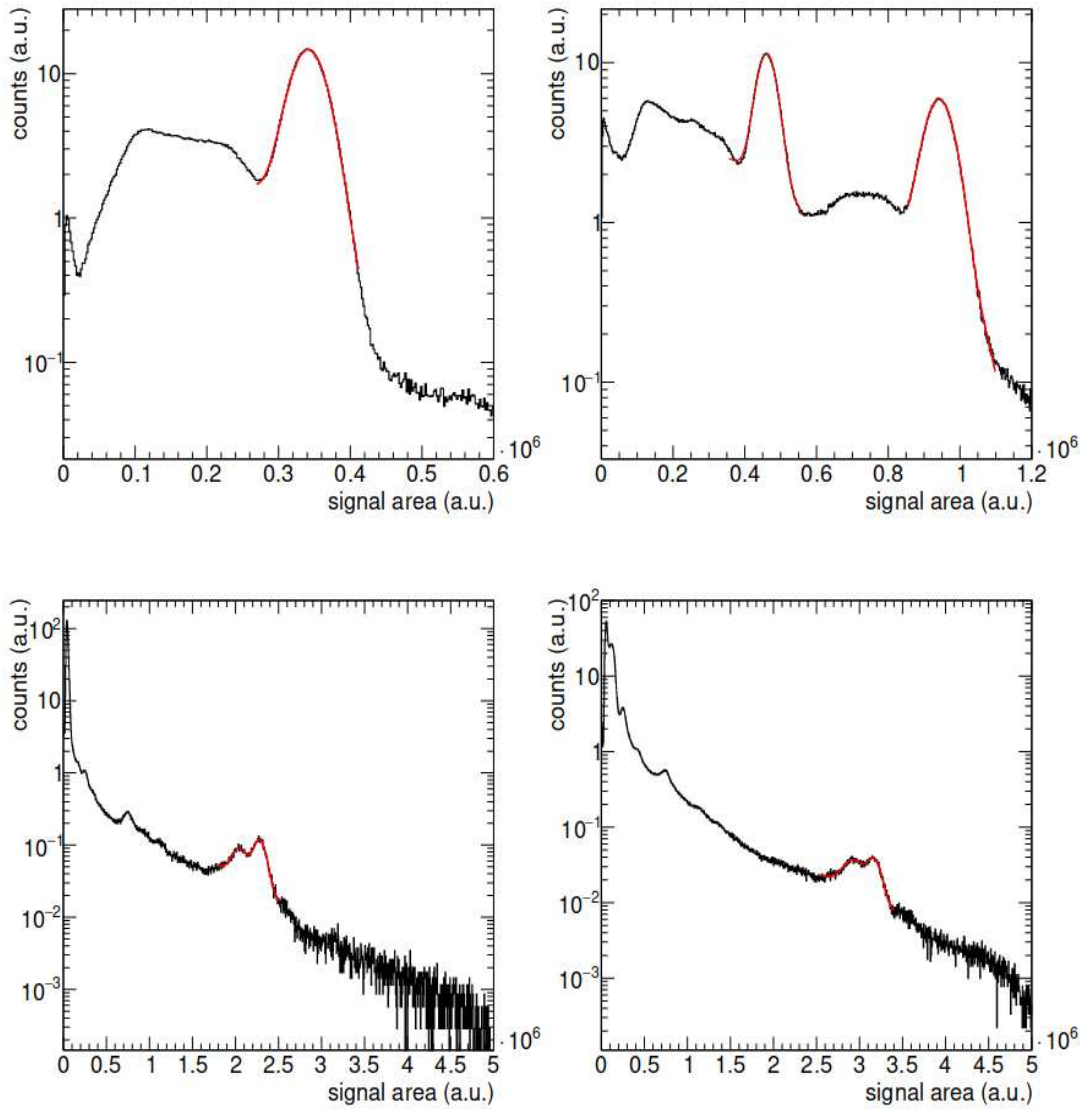
Figure B.1: BaF$_2$ module response to standard calibration sources ^{137}Cs (top left), ^{88}Y (top right), $AmBe$ (bottom left), and CmC (bottom right). Fits to the experimental data are shown in red using various fitting methods.

A Gaussian function and an assumed exponential background were employed in the gamma peak fits to produce the centroid. To fit the whole energy deposition and initial escape peak of the spectra of the AmBe and CmC sources, two Gaussian functions plus an assumed

exponential form of the background were utilized. A linear fit was used to determine the detector's deposited energy calibration as is given as Eq. B.1 and as shown in Fig. B.2.

$$centroid = k * E_\gamma [MeV] + d \tag{B.1}$$
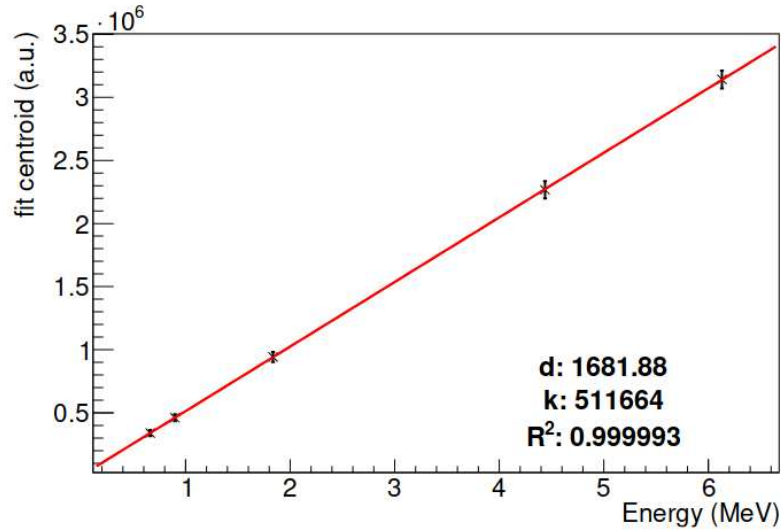
Figure B.2: Calibration curve for TAC.

During the validation of simulation process described in section 3.4.4 we stumbled upon strange ~300 keV peak during the simulation of ^{88}Y source. One of the main reasons for this peak could be gamma from the back-scattering process, but if this was the case then it should be notable in the ^{137}Cs spectra as well. Thinking that the 0.662 MeV gamma from Cs was not enough to cause backscattering, another simulation with a dummy gamma source with higher energy 2.0 MeV was carried out. The results of the simulation with and without the neutron absorber are given in Fig. B.3. We were expecting to see a sum peak at ~2.3 MeV for this case, which as can be seen was not found.

After this to further investigate another simulation for a dummy bi-gamma source was carried out with two gamma energies as follow: 2 MeV and 3 MeV. The results are shown in Fig. B.4. Here we can again see the effect of strange ~300 keV gamma. Although in this case for the simulation without neutron absorber this effects is barely seen indicating that the ~300-350 keV gamma could be coming due to the absorber. In summary, the origin of these peaks can be attributed with a high likelihood to back-scattered gamma-rays of approximately 300 keV. Notably, they manifest in the E_{sum} spectra precisely at the energy of the primary gamma emissions, augmented by 300 keV. This occurrence primarily emerges in scenarios where multiple γ-rays are emitted concurrently, a characteristic seen in cases involving the ^{88}Y source. In the next part of this investigation the position of these hits with energy between 300-350 keV for multiplicity = 2 in case of ^{88}Y with absorber was figured out as shown in Fig. B.5. These hits were uniformly distributed for all crystal multiplicities from 1 to 40. The fully TAC geometry is shown in Fig. B.6 and the crystal positions are shown in Fig. B.7.

The Geant4 simulated results corresponding to all the possible configurations up to I = 2, for IC corrected cases are presented below in Figures B.8, B.9, B.11, B.13, B.14, B.15 and B.16. It can be seen that the resolution for the reconstruction of E_{sum} peak around 6.31 MeV in case of $3^+, 3^-, 4^+, 4^-$ and 5^+ is poor. Fig. B.17 depicts the outcome of all simulations aggregated with equal weight.

The peak-to-tail ratio was determined by calculating the ratio between the counts in band 2 (B2), corresponding to the sum peak in the range of 5.9 to 6.3 MeV, and band 1 (B1), representing
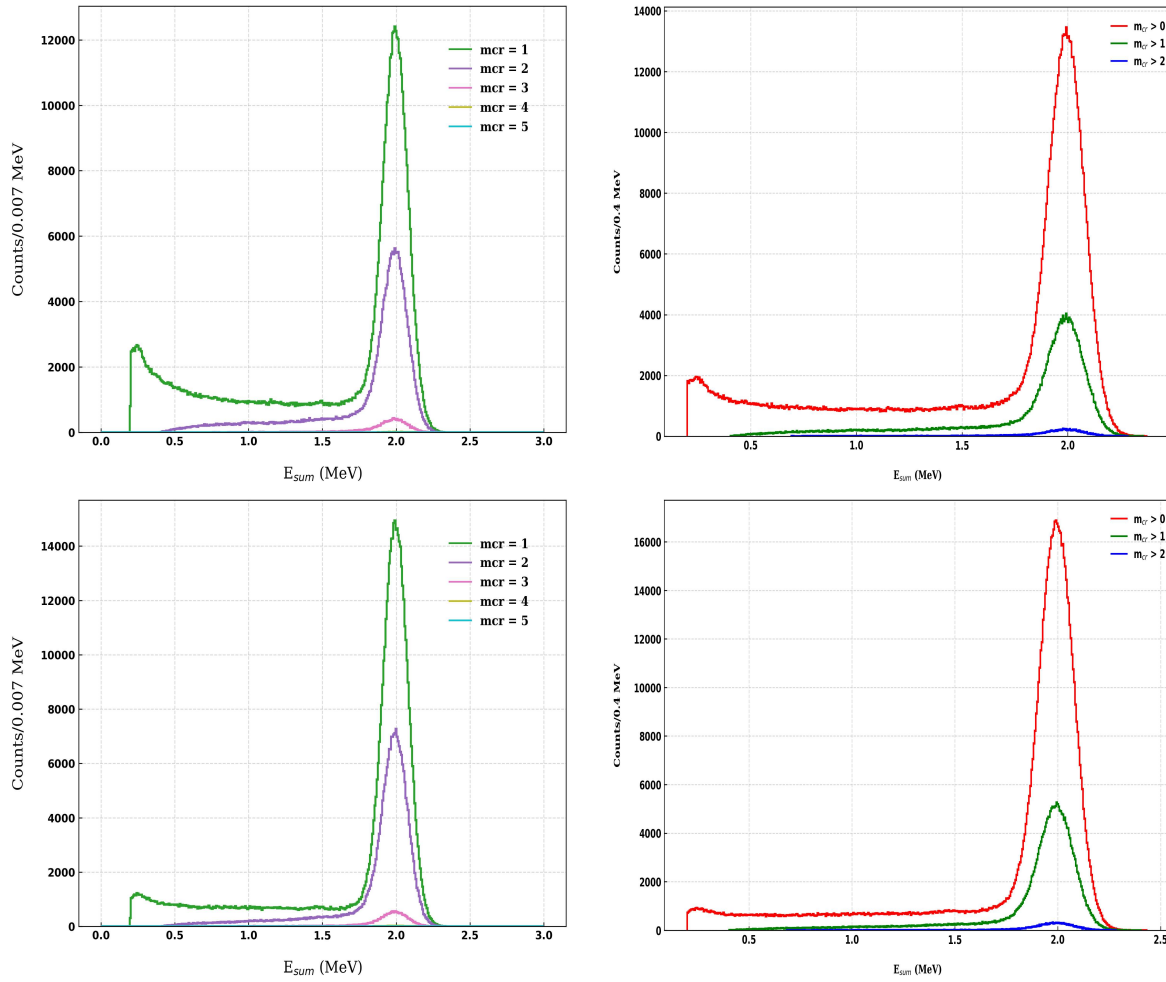
Figure B.3: Simulated results for the dummy gamma source with 2 MeV gamma with(top) and without(bottom) absorber.

the tail in the range of 5.4 to 5.8 MeV, see Fig. B.18. In the case of Fig. 5.5, it was found that the peak-to-tail ratio is maximized for $m_{\mathrm{cr}} \geq 4$, with a value of 0.066, see Fig. B.19. However, it should be noted that this method may not be the most suitable approach for assessing peak-to-tail ratios, as it may require adjusting the band ranges for different multiplicities based on the spectra.

Efficiency as a function of the max energy (upper limit) of the decided cut on E_{sum} (2.5 MeV < E_{sum} < 6.5 MeV) is given in Fig. B.20.
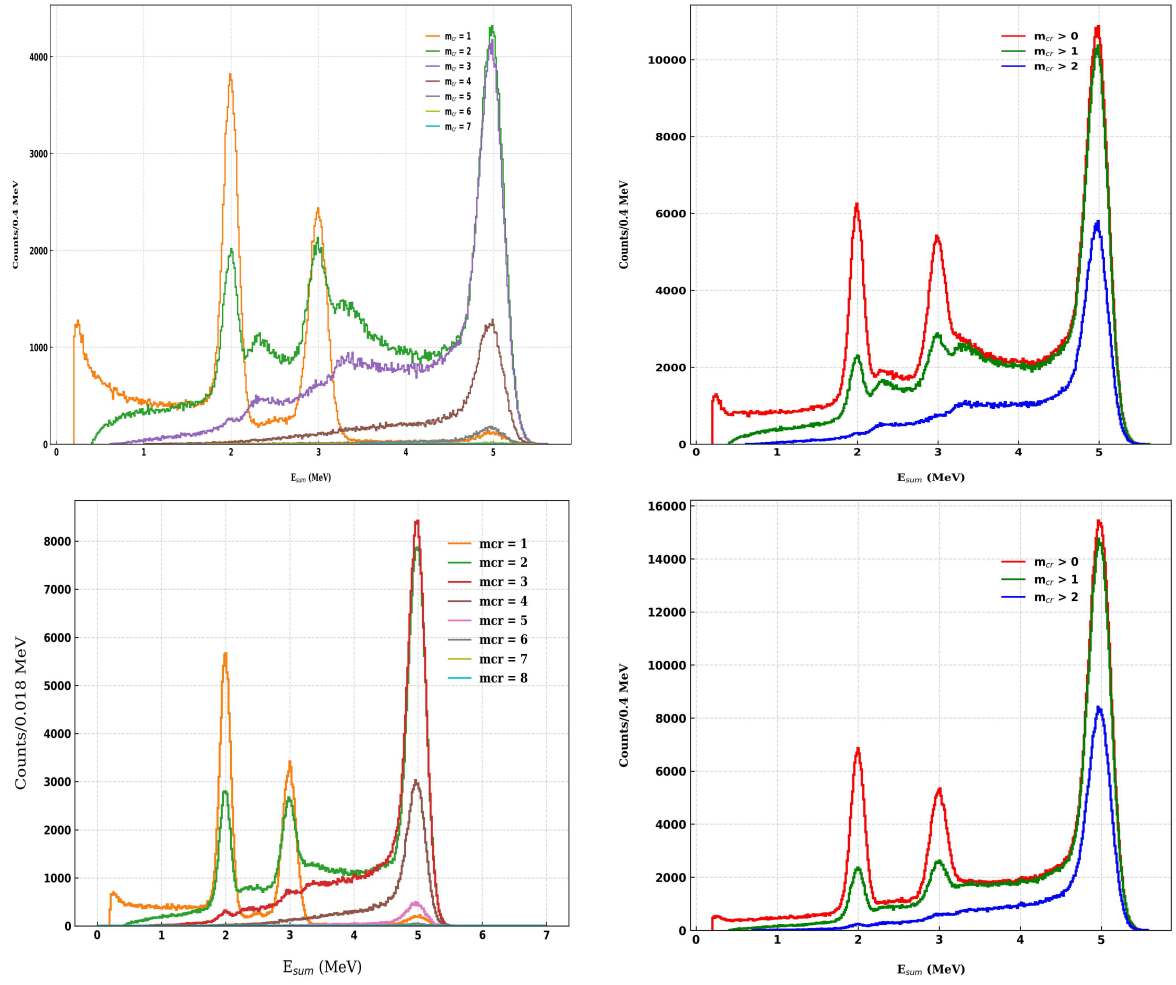
Figure B.4: Simulated results for the dummy bi-gamma source with 2 MeV and 3 MeV gamma with(top) and without(bottom) absorber.
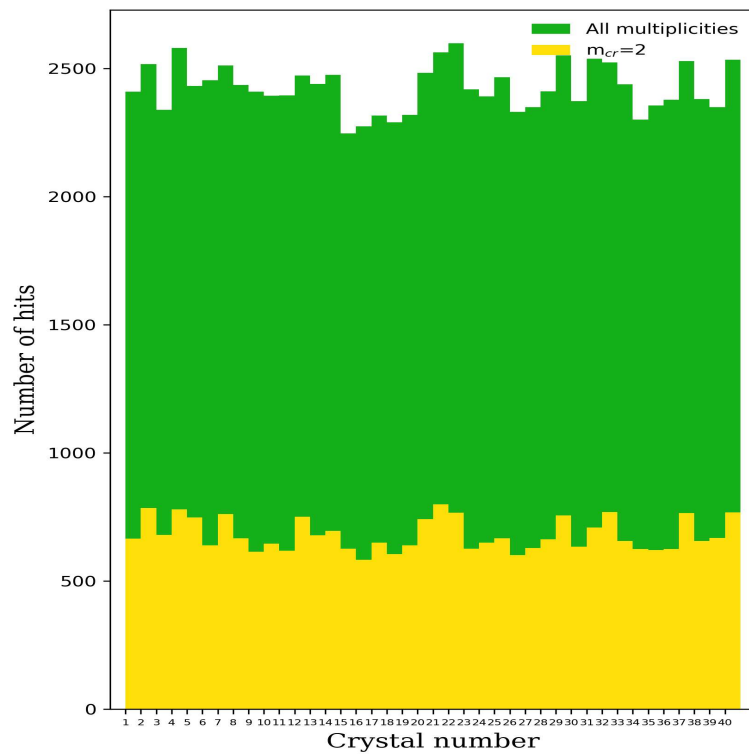
Figure B.5: Hits for gamma in the range of 300-350 keV for the TAC crystals(1-40) for m_{cr} =2 and for all multiplicities in case of ^{88}Y.
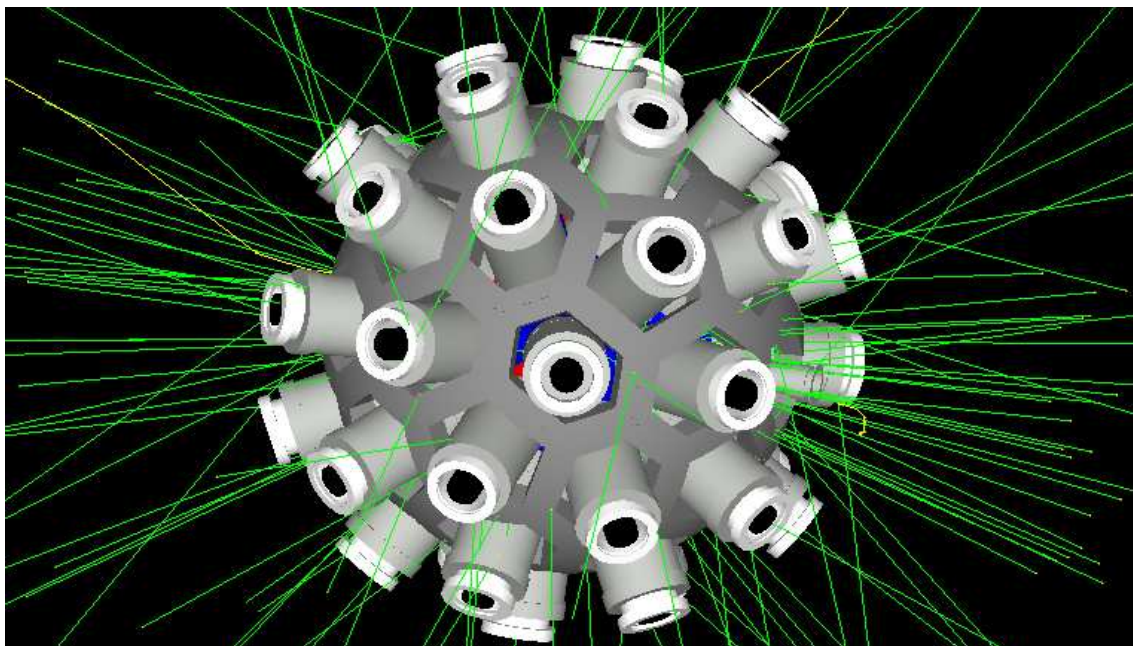
Figure B.6: Geant4 model of the experimental setup with full TAC hemisphere is displayed.
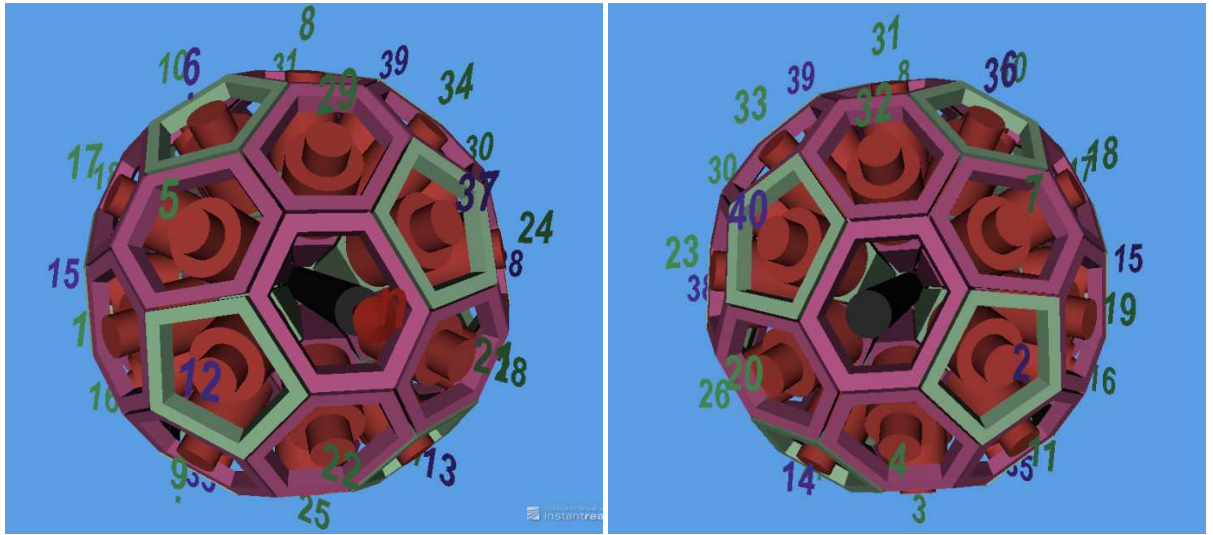
Figure B.7: Crystal position for the TAC.
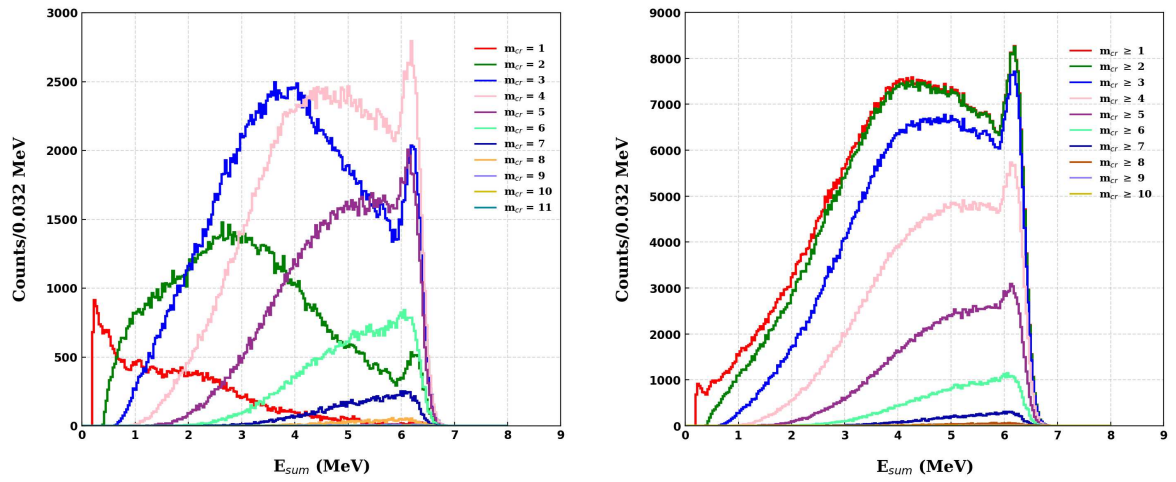
Figure B.8: TAC response for γ-cascade emission from neutron capture in $^{241}Pu(1^+state)$ configuration (with IC correction).
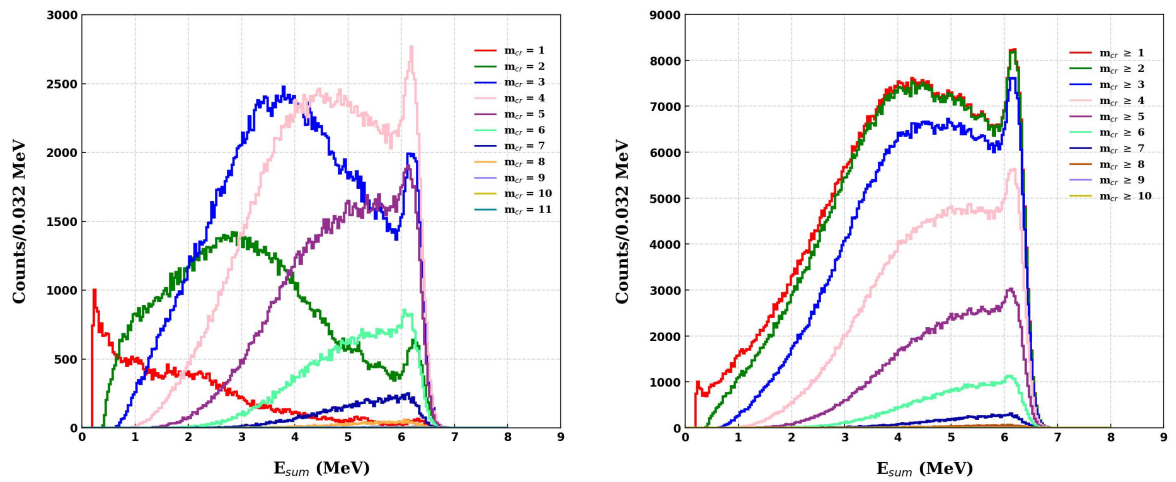
Figure B.9: TAC response for γ-cascade emission from neutron capture in $^{241}Pu(1^-state)$ configuration (with IC correction).
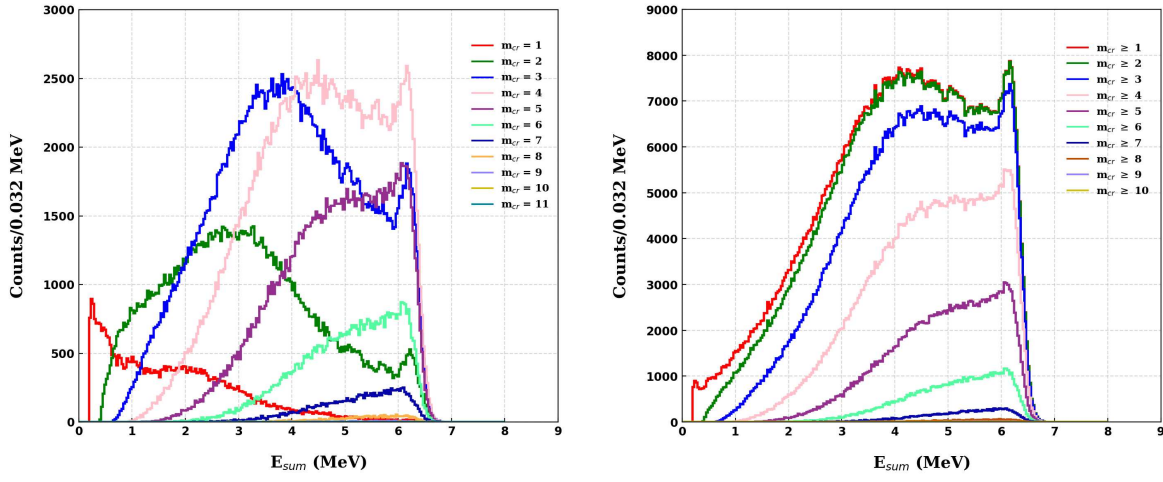
Figure B.10: TAC response for γ-cascade emission from neutron capture in $^{241}Pu(2^+state)$ configuration (with IC correction).
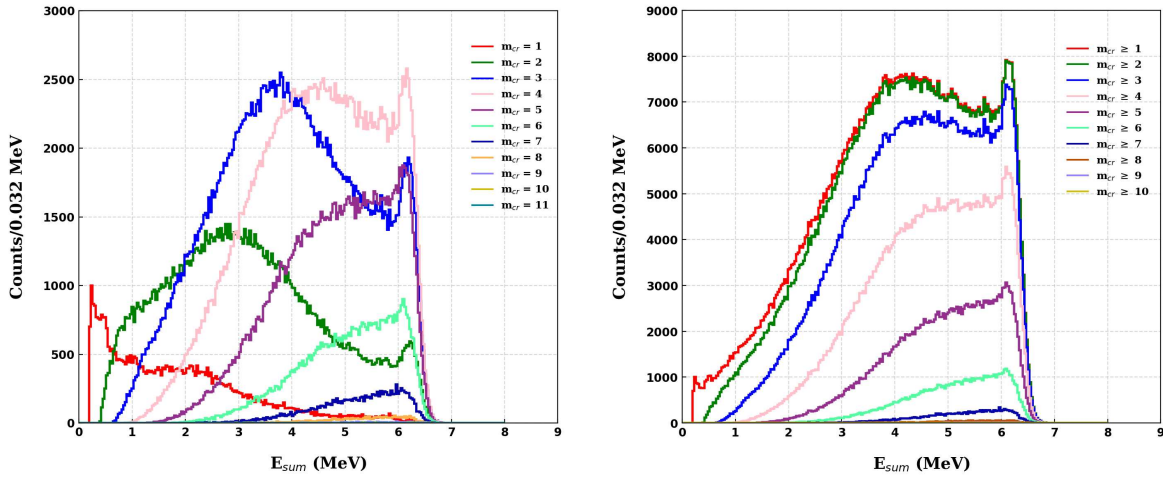
Figure B.11: TAC response for γ-cascade emission from neutron capture in $^{241}Pu(2^-state)$ configuration (with IC correction).
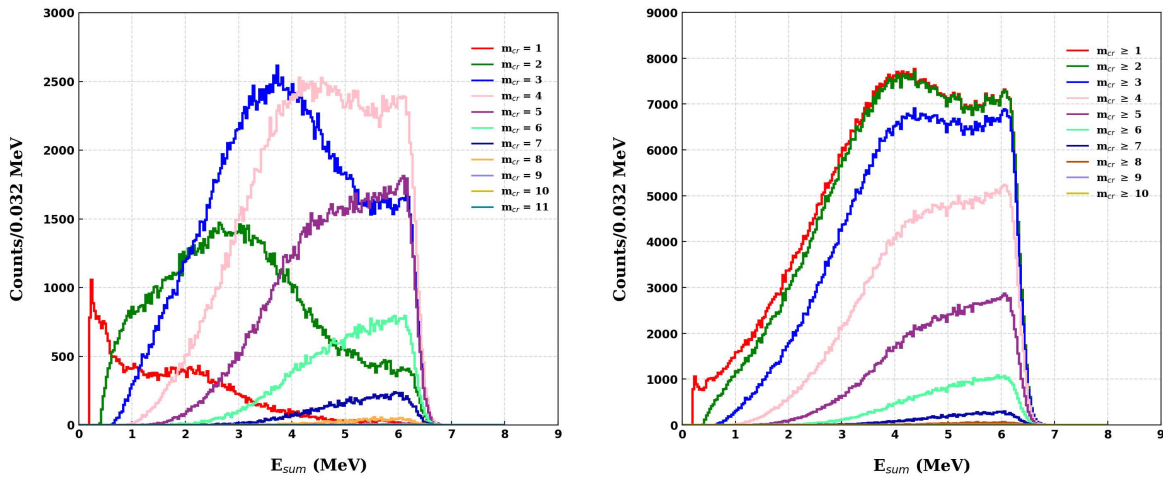
Figure B.12: TAC response for γ-cascade emission from neutron capture in $^{241}Pu(3^+state)$ configuration (with IC correction).
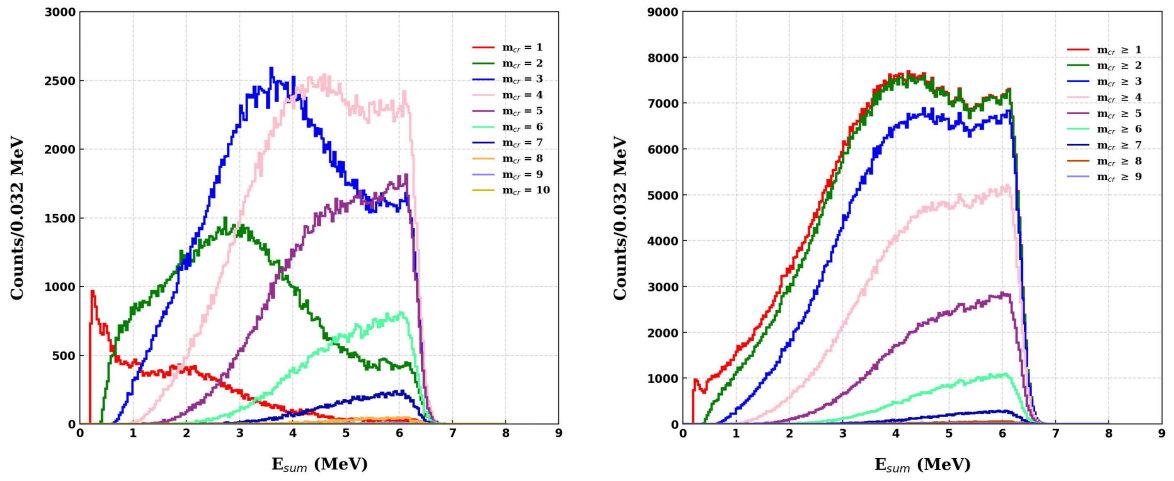
Figure B.13: TAC response for γ-cascade emission from neutron capture in $^{241}Pu(3^{-}state)$ configuration (with IC correction).
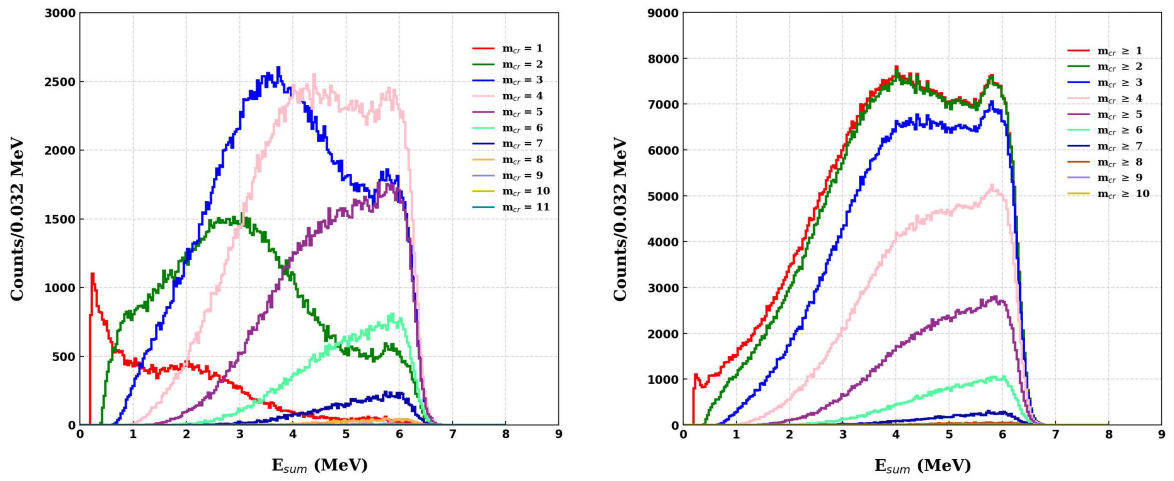
Figure B.14: TAC response for γ-cascade emission from neutron capture in $^{241}Pu(4^{+}state)$ configuration (with IC correction).
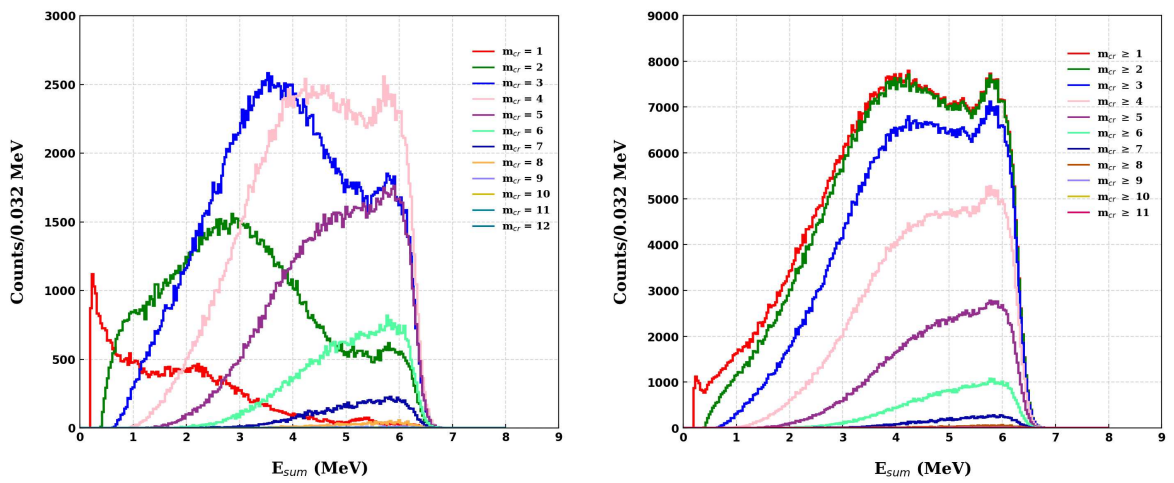
Figure B.15: TAC response for γ-cascade emission from neutron capture in $^{241}Pu(4^{-}state)$ configuration (with IC correction).
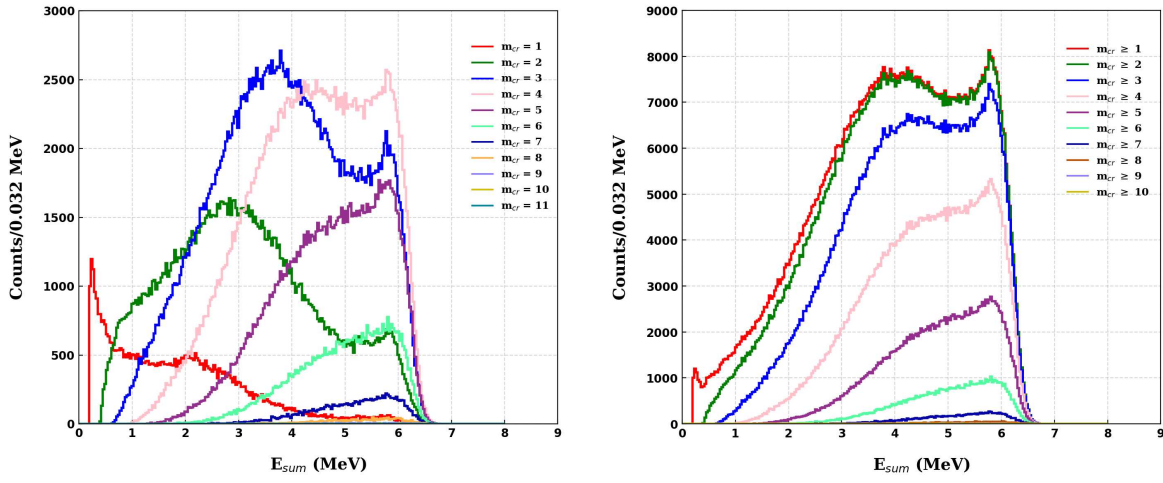
Figure B.16: TAC response for γ-cascade emission from neutron capture in $^{241}Pu(5^+ state)$ configuration (with IC correction).
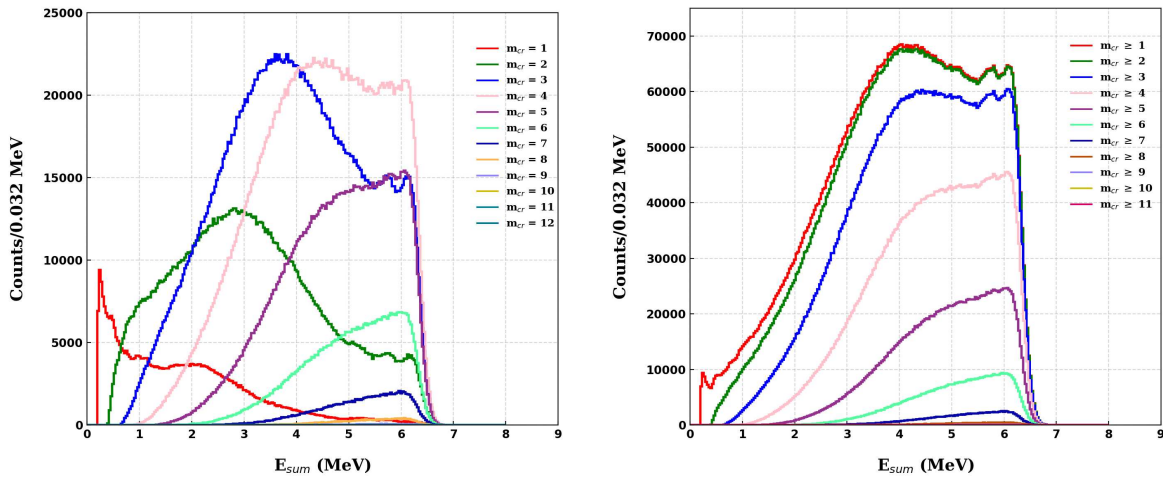
Figure B.17: TAC response for γ-cascade emission from neutron capture in ^{241}Pu for all simulated configuration (with IC correction).
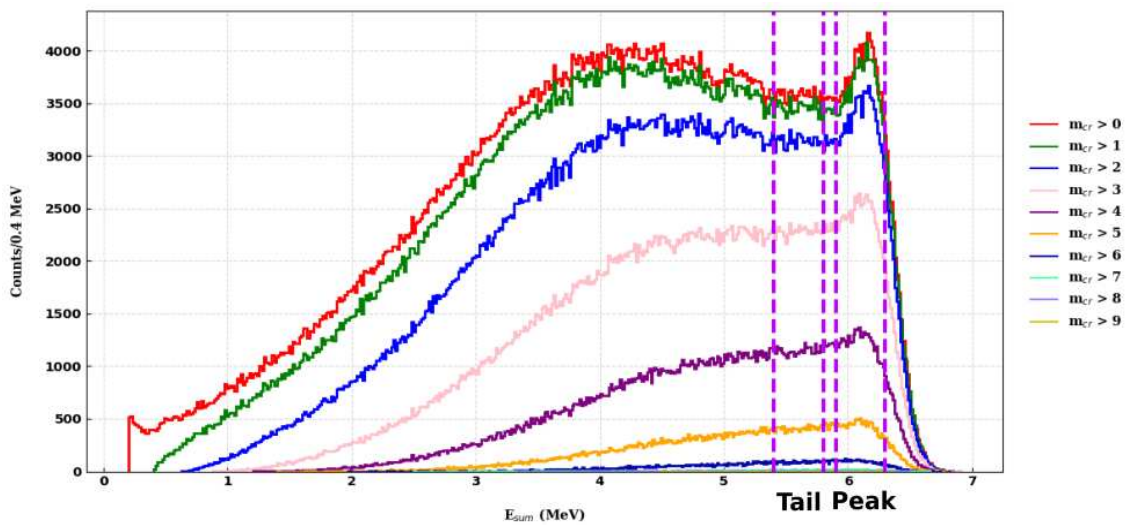
Figure B.18: Peak to background ratio.
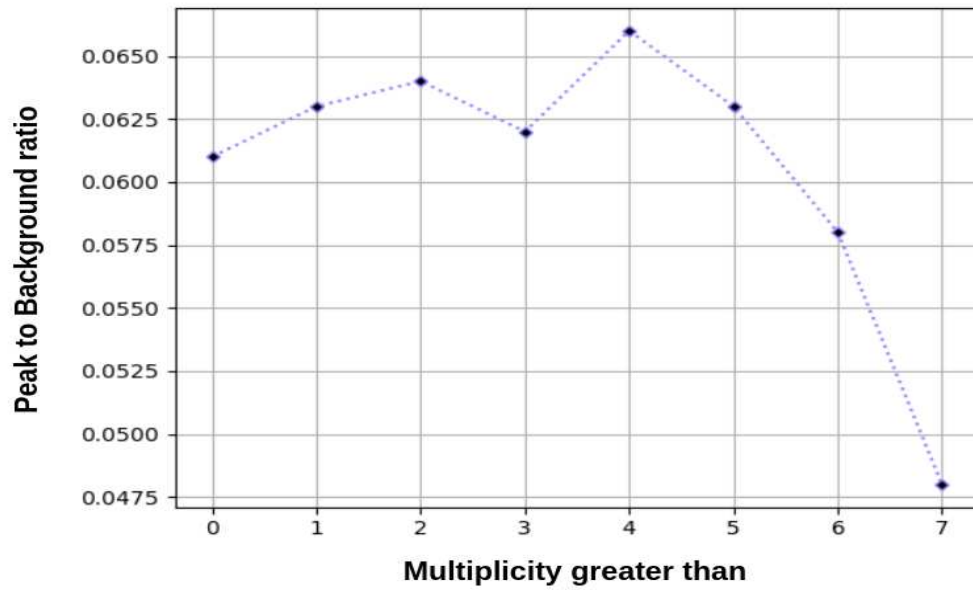
Figure B.19: Peak to tail ratio for different conditions on the multiplicity.
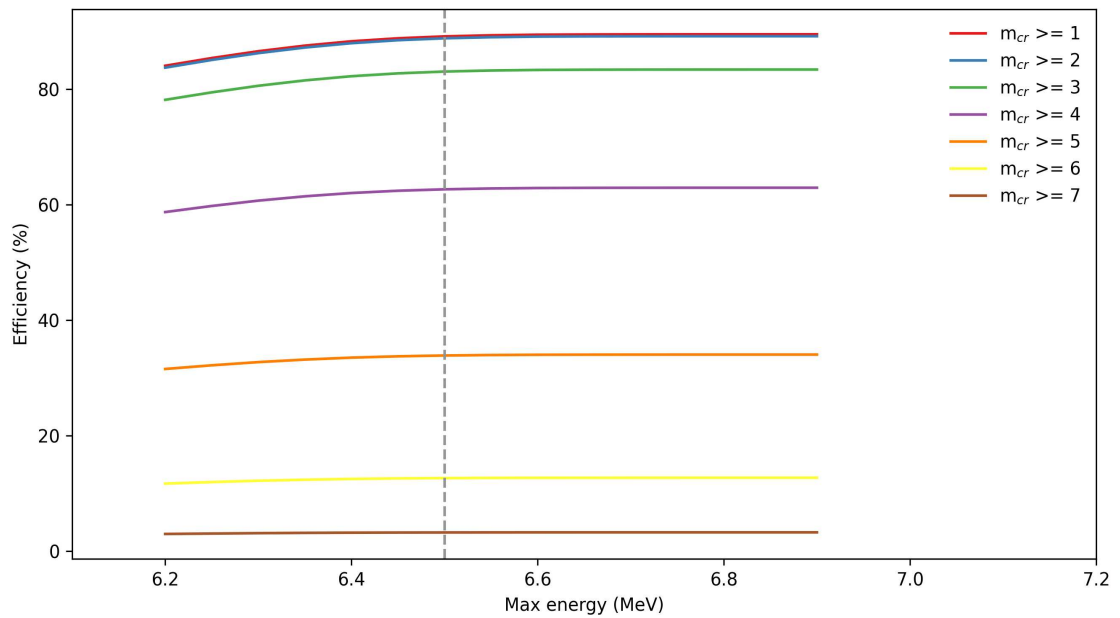
Figure B.20: Efficiency as a function of the max energy of the cut.

In this section some more results from the PFG simulation for ^{241}Pu have been presented using the Los Alamos model [1].

The Prompt Fission Gamma Spectrum (PFGS) is mostly constituted of statistical γ-rays from the Giant Dipole Resonance (GDR) with exit energies over 1 MeV and collective de-excitation along the yrast line. However, noteworthy spectrum characteristics may be found mostly below 1 MeV [57, 58] in the experimental data. This feature is not visible on the spectra as the spectra is smoothed out due to assuming certain distribution in the DANCE model for E_γ which do not take into account the specific transitions Fig. C.1.
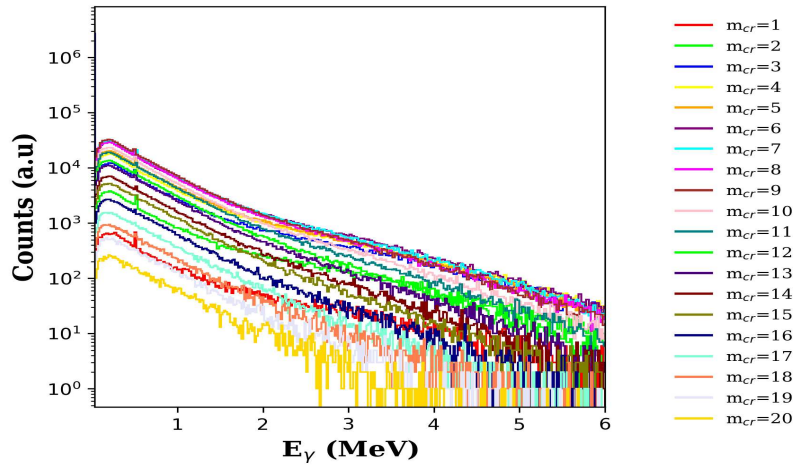
Figure C.1: Individual prompt fission γ-ray spectra.

The individual γ-ray energy E_γ vs multiplicity is shown in Fig. C.2
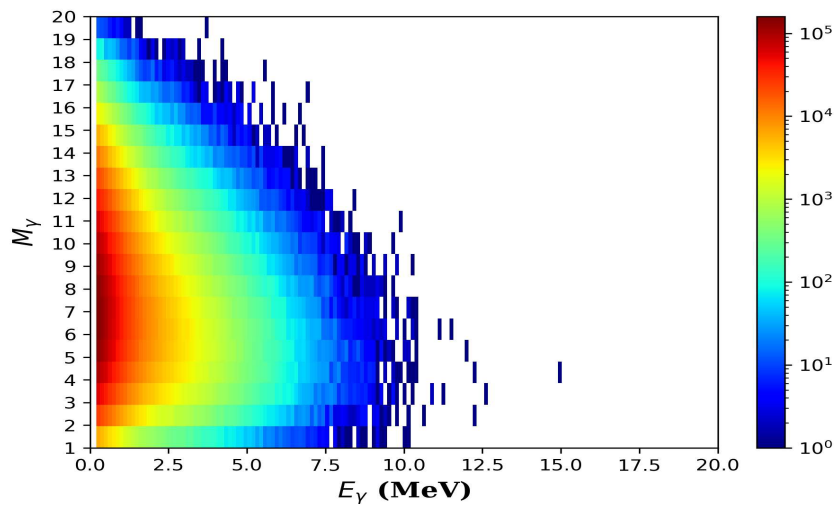
Figure C.2: Individual prompt fission γ-ray energy vs multiplicity for the neutron-induced fission of ^{241}Pu.

LIST OF FIGURES

LIST OF TABLES

[1]   M. Jandel et al. "Prompt Fission Gamma-ray Studies at DANCE." In: *Physics Procedia* 59 (2014). GAMMA-2 Scientific Workshop on the Emission of Prompt Gamma-Rays in Fission and Related Topics, pp. 101–106. ISSN: 1875-3892. DOI: https://doi.org/10.1016/j.phpro.2014.10.016. URL: https://www.sciencedirect.com/science/article/pii/S187538921400491X.

[2]   J. Krepel and E. Losa. "Closed U-Pu and Th-U cycle in sixteen selected reactors: Comparison of major equilibrium features." In: *Annals of Nuclear Energy* 128 (2019), pp. 341–357. ISSN: 0306-4549. DOI: https://doi.org/10.1016/j.anucene.2019.01.013. URL: https://www.sciencedirect.com/science/article/pii/S0306454919300180.

[3]   "The Generation IV International forum." In: (2013). URL: https://www.gen-4.org/.

[4]   Pavel Valeryevich Tsvetkov, Salvador B Rodriguez, David E Ames II, and Gary Eugene Rochau. "High fidelity nuclear energy system optimization towards an environmentally benign, sustainable, and secure energy source." In: (Oct. 2010). DOI: 10.2172/992769. URL: https://www.osti.gov/biblio/992769.

[5]   Yasuyuki Kikuchi. "Evaluation of Neutron Cross Sections of Plutonium-241." In: *Journal of Nuclear Science and Technology* 14.7 (1977), pp. 467–481.

[6]   L. W. Weston. "REVIEW OF FAST-NEUTRON CAPTURE CROSS SECTIONS OF THE HIGHER PLUTONIUM ISOTOPES AND Am-241." In: *Oak Ridge National Laboratory* ().

[7]   "The Nuclear Energy Agency: High Priority Request List." In: (2023). URL: www.oecd-nea.org/dbdata/hprl.

[8]   W.S.C. Williams. *Nuclear and particle physics*. Oxford at the Clarendon, 1991. URL: https://books.google.fr/books?id=h10yMgEACAAJ.

[9]   J.R. Lamarsh. *Introduction to Nuclear Engineering. 2nd Edition*. Addison-Wesley, 1983.

[10]   W. M. Stacey. *Nuclear Reactor Physics*. John Wiley Sons, ISBN: 0- 471-39127-1, 2001.

[11]   Niels Bohr and John Archibald Wheeler. "The Mechanism of Nuclear Fission." In: *Phys. Rev.* 56 (5 1939), pp. 426–450. DOI: 10.1103/PhysRev.56.426. URL: https://link.aps.org/doi/10.1103/PhysRev.56.426.

[12]   G. Breit and E. Wigner. "Capture of Slow Neutrons." In: *Phys. Rev.* 49 (7 1936), pp. 519–531. DOI: 10.1103/PhysRev.49.519. URL: https://link.aps.org/doi/10.1103/PhysRev.49.519.

[13]   W. Heisenberg. "Über den anschaulichen Inhalt der quantentheoretischen Kinematik und Mechanik." In: *Zeitschrift für Physik* 43 (172 1927), pp. 172–198. DOI: 10.1007/BF01397280. URL: https://doi.org/10.1007/BF01397280.

[14]   Eugene P. Wigner. "Resonance Reactions." In: *Phys. Rev.* 70 (9-10 1946), pp. 606–618. DOI: 10.1103/PhysRev.70.606. URL: https://link.aps.org/doi/10.1103/PhysRev.70.606.

[15]   E. P. Wigner and L. Eisenbud. "Higher Angular Momenta and Long Range Interaction in Resonance Reactions." In: *Phys. Rev.* 72 (1 1947), pp. 29–41. DOI: 10.1103/PhysRev.72.29. URL: https://link.aps.org/doi/10.1103/PhysRev.72.29.

[16]   "Evaluation and Analysis of Nuclear Resonance Data." In: *NEA* (2000).

[17] F. Bečvář. "Simulation of γ cascades in complex nuclei with emphasis on assessment of uncertainties of cascade-related quantities." In: *Nuclear Instruments and Methods in Physics Research A* 417.2 (Jan. 1998), pp. 434–449. DOI: 10.1016/S0168-9002(98)00787-6.

[18] D. Brink. "Some Aspects of the Interaction of Light with Matter." PhD thesis. University of Oxford, 1955.

[19] Magne Guttormsen, Ann Cecilie Larsen, A. Görgen, Therese Renstrøm, Sunniva Siem, T. Tornyi, and Gry Tveten. "Validity of the Generalized Brink-Axel Hypothesis in ^{238}Np." In: *Physical Review Letters* 116 (Nov. 2015). DOI: 10.1103/PhysRevLett.116.012502.

[20] Carlo Rubbia et al. *A High Resolution Spallation Driven Facility at the CERN-PS to Measure Neutron Cross Sections in the Interval from 1 eV to 250 MeV: a Relative Performance Assessment*. Tech. rep. Addendum to CERN-LHC-98-002-EET. Geneva: CERN, 1998. URL: https://cds.cern.ch/record/363828.

[21] Federica Mingrone, Marco Calviani, Claudio Torregrosa Martin, Oliver Aberle, Michael Bacak, Enrico Chiaveri, Elvis Fornasiere, Antonio Perillo-Marcone, Vasilis Vlachoudis, and the n_TOF Collaboration. "Development of a Neutron Imaging Station at the n_TOF Facility of CERN and Applications to Beam Intercepting Devices." In: *Instruments* 3.2 (2019). ISSN: 2410-390X. DOI: 10.3390/instruments3020032. URL: https://www.mdpi.com/2410-390X/3/2/32.

[22] C. Guerrero, A. Tsinganis, E. Berthoumieux, and et al. "Performance of the neutron time-of-flight facility n_TOF at CERN." In: *Eur. Phys. J. A 49, 27* (2013). URL: https://doi.org/10.1140/epja/i2013-13027-6.

[23] C. Guerrero et al. "The n_TOF Total Absorption Calorimeter for neutron capture measurements at CERN." In: *Nuclear Instruments and Methods in Physics Research Section A: Accelerators, Spectrometers, Detectors and Associated Equipment* 608.3 (2009), pp. 424–433. ISSN: 0168-9002. DOI: https://doi.org/10.1016/j.nima.2009.07.025. URL: https://www.sciencedirect.com/science/article/pii/S016890020901465X.

[24] K. Wisshak and et al. "Nucl. Instr. Meth. A 292:595618." In: (1990).

[25] J. Balibrea-Correa et al. "Measurement of the neutron capture cross section of the fissile isotope 235U with the CERN n_TOF total absorption calorimeter and a fission tagging based on micromegas detectors." In: *EPJ Web of Conferences* 146 (Jan. 2017), p. 11021. DOI: 10.1051/epjconf/201714611021.

[26] S. Agostinelli et al. "GEANT4–a simulation toolkit." In: *Nucl. Instrum. Meth. A* 506 (2003), pp. 250–303. DOI: 10.1016/S0168-9002(03)01368-8.

[27] H. Burkhardt, Vladimir Grichine, Peter Gumplinger, V.N. Ivanchenko, Rostislav Kokoulin, M. Maire, and Laszlo Urban. "Geant4 standard electromagnetic package for HEP applications." In: vol. 3. Nov. 2004, 1907 –1910 Vol. 3. ISBN: 0-7803-8700-7. DOI: 10.1109/NSSMIC.2004.1462617.

[28] Glenn F. Knoll. *Radiation Detection and Measurement*. Wiley Third edition, 2000.

[29] Michael Bacak. "Development of a detector for the simultaneous measurement and for the study of uranium-233 capture and fission yields at the CERN n_TOF neutron source." In: (2019).

[30] "National Nuclear Data Center (NNDC) Evaluated Nuclear Structure Data File Search and Retrieval." In: ((2023).). DOI: https://doi.org/10.1016/j.nima.2021.166202. URL: /www.nndc.bnl.gov/ensdf.

[31]   C. E. Porter and R. G. Thomas. "Fluctuations of Nuclear Reaction Widths." In: *Phys. Rev.* 104 (2 1956), pp. 483–491. DOI: 10.1103/PhysRev.104.483. URL: https://link.aps.org/doi/10.1103/PhysRev.104.483.

[32]   T. von Egidy and D. Bucurescu. "Experimental energy-dependent nuclear spin distributions." In: *Phys. Rev. C* 80 (5 2009), p. 054310. DOI: 10.1103/PhysRevC.80.054310. URL: https://link.aps.org/doi/10.1103/PhysRevC.80.054310.

[33]   Thibault Laplace et al. "Statistical properties of ^{243}Pu, and ^{242}Pu(n,γ) cross section calculation." In: (Nov. 2015).

[34]   T. von Egidy and D. Bucurescu. "Experimental energy-dependent nuclear spin distributions." In: *Phys. Rev. C* 80 (5 2009), p. 054310. DOI: 10.1103/PhysRevC.80.054310. URL: https://link.aps.org/doi/10.1103/PhysRevC.80.054310.

[35]   *Reference Input Parameter Library (RIPL-3)*. https://www-nds.iaea.org/RIPL-3/.

[36]   F. Zeiser et al. "Restricted spin-range correction in the Oslo method: The example of nuclear level density and γ -ray strength function from ^{239}Pu(d,pγ)^{240}Pu." In: *Phys. Rev. C* 100.2 (2019), p. 024305. DOI: 10.1103/PhysRevC.100.024305. arXiv: 1904.02932 [nucl-ex].

[37]   J. Kopecky, S. Goriely, S. Péru, S. Hilaire, and M. Martini. "$E1$ and $M1$ strength functions from average resonance capture data." In: *Phys. Rev. C* 95 (5 2017), p. 054317. DOI: 10.1103/PhysRevC.95.054317. URL: https://link.aps.org/doi/10.1103/PhysRevC.95.054317.

[38]   R.E. Chrien, J. Kopecky, H.I. Liou, O.A. Wasson, J.B. Garg, and M. Dritsa. "Distribution of radiative strength from neutron capture by 239Pu." In: *Nuclear Physics A* 436.2 (1985), pp. 205–220. ISSN: 0375-9474. DOI: https://doi.org/10.1016/0375-9474(85)90196-4. URL: https://www.sciencedirect.com/science/article/pii/0375947485901964.

[39]   G.M. Gurevich, L.E. Lazareva, V.M. Mazur, G.V. Solodukhov, and B.A. Tulupov. "Giant resonance in the total photoabsorption cross section of Z 90 nuclei." In: *Nuclear Physics A* 273.2 (1976), pp. 326–340. ISSN: 0375-9474. DOI: https://doi.org/10.1016/0375-9474(76)90594-7. URL: https://www.sciencedirect.com/science/article/pii/0375947476905947.

[40]   ka, familyi=v., given=M., giveni=M., „ S. Goriely, S. Hilaire, S. Péru, and S. Valenta. "Constraints on the dipole photon strength functions from experimental multistep cascade spectra." In: *Phys. Rev. C* 99 (4 2019), p. 044308. DOI: 10.1103/PhysRevC.99.044308. URL: https://link.aps.org/doi/10.1103/PhysRevC.99.044308.

[41]   Till von Egidy and Dorel Bucurescu. "Systematics of nuclear level density parameters." In: *Phys. Rev. C* 72 (4 2005), p. 044311. DOI: 10.1103/PhysRevC.72.044311. URL: https://link.aps.org/doi/10.1103/PhysRevC.72.044311.

[42]   T. Kibédi et al. "Simulation of gamma cascades in complex nuclei with emphasis on assessment of uncertainties of cascade-related quantities." In: *Nuc. Inst. and Meth. A* (589 2008), pp. 202–229. URL: bricc.anu.edu.au..

[43]   T. Von Egidy, H.H. Schmidt, and A.N. Behkami. "Nuclear level densities and level spacing distributions: Part II." In: *Nuclear Physics A* 481.2 (1988), pp. 189–206. ISSN: 0375-9474. DOI: https://doi.org/10.1016/0375-9474(88)90491-5. URL: https://www.sciencedirect.com/science/article/pii/0375947488904915.

[44]   A. Gilbert and A. G. W. Cameron. "A COMPOSITE NUCLEAR-LEVEL DENSITY FORMULA WITH SHELL CORRECTIONS." In: *Canadian Journal of Physics* 43.8 (1965), pp. 1446–1496. DOI: 10.1139/p65-139. eprint: https://doi.org/10.1139/p65-139. URL: https://doi.org/10.1139/p65-139.

[45] M.J. Martin and C.D. Nesaraja. "Nuclear Data Sheets for A=242." In: *Nuclear Data Sheets* 186 (2022), pp. 263–395. ISSN: 0090-3752. DOI: https://doi.org/10.1016/j.nds.2022.11.003. URL: https://www.sciencedirect.com/science/article/pii/S0090375222000588.

[46] "JANIS Web." In: (). URL: https://www.oecd-nea.org/janisweb/.

[47] "JANIS Web, Incident neutron data for Resonances." In: (). URL: https://www.oecd-nea.org/janisweb/tree/N/'ENDF/B-VIII.0'/SIG/Pu/Pu241/resonances/resonances.

[48] Tatum. *Boltzmann's Equation*. Year. URL: https://phys.libretexts.org/Bookshelves/Astronomy__Cosmology/Stellar_Atmospheres_%28Tatum%29/08%3A_Boltzmann's_and_Saha's_Equations/8.04%3A_Boltzmann's_Equation.

[49] R. Shankar. *Principles of Quantum Mechanics*. Plenum Press, New York, 1994. URL: http://dx.doi.org/10.1007/978-1-4757-0576-8.

[50] L. M. Bacak and et al. "Preliminary results on the ^{233}U capture cross section and alpha ratio measured at n_TOF (CERN) with the fission tagging technique." In: *EPJ Web Conf.* 211 (2019), p. 03007. DOI: 10.1051/epjconf/201921103007. eprint: Publishedonline05June2019.

[51] *ADVANCES IN BORON NEUTRON CAPTURE THERAPY*. VIENNA: INTERNATIONAL ATOMIC ENERGY AGENCY, 2023. URL: https://www-pub.iaea.org/MTCD/Publications/PDF/CRCP-BOR-002_web.pdf.

[52] L. I. Govor, A. M. Demidov, and I. V. Mikhailov. "Investigation of 138Ba in the (n, n') reaction." In: *Physics of Atomic Nuclei* 66 (2003), pp. 17–29. DOI: 10.1134/1.1540653.

[53] X. Mougeot and M. M. Bé. *Comments on evaluation of decay data for La-138*. Online document. Year of publication. URL: http://www.lnhb.fr/nuclides/La-138_com.pdf.

[54] K. Skarsvag. "Time distribution of $rays from spontaneous fission of^{252}Cf$ at short times." In: *Nuclear Physics A* 253 (1975), p. 274.

[55] A. Chyzh et al. "Systematics of prompt -ray emission in fission." In: *Physical Review C* 87.034620 (2013), p. 034620. DOI: 10.1103/PhysRevC.87.034620.

[56] Wikipedia contributors. *Yrast*. https://en.wikipedia.org/wiki/Yrast.

[57] J. Behrens. *Determination of Absolute Fission Cross Section Ratios Using the Method of Threshold Cross Sections*. Technical Report UCRL-51478. Lawrence Livermore National Laboratory, 1973, p. 97.

[58] G. W. Carlson and J. W. Behrens. "Measurement of the fission cross sections of Uranium-233 and Plutonium-239 relative to Uranium-235 from 1 keV to 30 MeV." In: *Nuclear Science and Engineering* 66 (1978), p. 205.

[59] V. V. Verbinski, H. Weber, and R. E. Sund. "Prompt gamma rays from 235U(n,f), 239Pu(n,f) and spontaneous fission of 252Cf." In: *Physical Review C* 7 (1973), p. 1173.

[60] J. L. Ullmann and et al. "Prompt -ray production in neutron-induced fission of 239Pu." In: *Physical Review C* 87 (2013), p. 044607.

[61] A. Chyzh and et al. "Total prompt -ray emission in fission of 235U, 239,241Pu, and 252Cf." In: *Physical Review C* 90 (2014), p. 014602.

[62] K. H. Schmidt and et al. "General Description of Fission Observables: GEF Model Code." In: *Nuclear Data Sheets* 131 (2016), pp. 107–221.

[63] T. E. Valentine. "Evaluation of prompt fission gamma rays for use in simulating nuclear safeguard measurements." In: *Annals of Nuclear Energy* 28.3 (2001), p. 777.